Development and data analysis of a position detector for AE$\bar{g}$IS (Antimatter Experiment: Gravity, Interferometry, Spectroscopy)

Angela Gligorova

Dissertation for the degree of Philosophiae Doctor (PhD)

Department of Physics and Technology
University of Bergen

Dissertation date: 13.03.2015

Acknowledgements

During my PhD studies and my research stay both in Bergen and at CERN, I had the privilege to work with many inspiring people who were strongly supporting my work and whom I would like to thank. I would like to begin by acknowledging my CERN supervisor, Michael Doser, for sharing his wisdom and knowledge with me, not only through the years of my thesis work, but also in the time prior to that. Thank you goes to him also for the constant help and advices concerning both theoretical and experimental physics, as well as administrative matters. Finally, if it weren't for Michael I wouldn't have met my PhD supervisor from the University of Bergen, Heidi Sandaker, and this thesis would have never happened. I thank him for all that.

My second but not less important thank you is for my main PhD supervisor, Heidi, for all the help, support and encouragement from the very first to the very last day of my PhD studies. I thank her for all the patience and unquestioned belief in me, and especially for the guidance through my scientific work. Also thanks for the useful and motivational conversations every time I thought there is no way out and for the understanding you had for all the difficulties I went through, not only professional, but private as well.

Next thank you is given to Nicola Pacifico, my co-supervisor, colleague, office mate and friend. Thank you for the enormous help and support throughout my day-to-day work, for all the advices and proof-readings, for the cheerful environment in our office. Thanks as well for keeping up the good spirit and making things work during beam test and shifts even when the situation seemed hopeless. Finally, I thank him for all the fun and laughing and I'm looking forward for the next "grab and fly" break at the airport.

I would also like to thank all my colleagues from the AEḡIS collaboration, for creating an enjoyable environment for doing research, for the shifts we did together, as well as for all the pleasant conversations during lunches and the collaboration meetings.

My warm gratitude to Massimo Caccia, for being my host at the University in Como and for sharing his time and knowledge to introduce me to MAPS detectors. Thank you also for providing the MIMOTERA for the measurements and for all the logistics during the first beam tests.

A very special thank you for Michael Holzscheiter, for giving me the opportunity to get involved with another CERN project, ACE and for the kind support he provided for my applications. Thank you also for proof reading this thesis and for the wonderful comments. Another great thank you goes to my colleague Thomas Kaltenbacher and to the professor in theoretical physics from UiB, Jan Petter Hansen, who read the thesis and helped me to improve it with very useful comments.

I would also like to express a deep gratitude to Zlatko Dimcovski, the physics professor who introduced me to the work at CERN and initiated my involvement in AEḡIS. My thanks also go to Anna Lipniacka for the useful advices and for opening her home

in Bergen to me during my exams.

To Lee and Ed, thank you for your friendship and for the wonderful time in Seoul!

To all my friends in Macedonia and Switzerland, for the trips we made together and the happy times we shared.

The greatest thank you of all is for my parents, for everything.

Abstract

AEgIS (Antimatter Experiment: Gravity, Interferometry, Spectroscopy) is an antimatter experiment based at CERN, the European Organization for Nuclear Research, whose goal is to carry out the first direct measurement of the Earth's gravitational acceleration on antimatter. The outcome of such measurement would be the first precision test of the Weak Equivalence Principle in a completely new area. According to WEP, all bodies fall with the same acceleration regardless of their mass and composition. AEgIS will attempt to achieve its aim by measuring the gravitational acceleration ($\bar{g}$) for antihydrogen with 1% relative precision. The first step towards the final goal is the formation of a pulsed, cold antihydrogen beam, which will be performed by a charge exchange reaction between laser excited (Rydberg) positronium and cold (100 mK) antiprotons. The antihydrogen atoms will be accelerated by an inhomogeneous electric field (Stark acceleration) to form a beam whose free fall due to Earth's gravity will be measured with a moiré deflectometer coupled to a hybrid position detector. This detector will consist of an active silicon part, where the annihilation of antihydrogen takes place, followed by an emulsion part.

The work in this thesis is part of the R&D efforts for the construction of the silicon position detector. The results presented here are from beam test studies of low energy antiproton annihilations in silicon sensors. The outcome of these tests defined the basis for the final design parameters for the silicon position detector.

This thesis is based on three papers. The first paper reports on the results of the very first study of low energy (0-700 keV) antiproton annihilations in a segmented silicon detector. The results include cluster and energy deposition studies, as well as a first comparison with simulation models for low energy antiproton annihilation in silicon.

The second paper presents the results of a study on the signatures of an annihilation event in different silicon sensors which were designed to detect minimum ionizing particles or slow charged hadrons. The characteristics of the clusters due to antiproton annihilations were investigated for silicon detectors with various geometries. The correlation of the clusters charateristics, such as the released energy and the size provided a better overview of the performance of the microstrip technology when compared to pixel detector technologies.

The third paper compares two different silicon sensor technologies (MAPS and 3D pixel) used for the detection of low energy antiprotons in order to study the impact of the thickness of the detector on the cluster characteristics, as well as to estimate the achievable position resolution. Comparison with simulation models are also reported, which proved to account for the intrinsic technological differences in the two sensors.

The work and the results in this thesis work have contributed to a better understanding of the annihilation process in silicon and proved that silicon detectors can be used for direct detection of low energy antiprotons. A first comparison between experimen-

tal data and Monte Carlo simulation results for low energy antiproton annihilation is also reported, suggesting areas where the improvement of simulation models is possible.

List of papers

1. S. Aghion et al. (AEgIS collaboration), *Detection of low energy antiproton annihilations in a segmented silicon detector*, Journal of instrumentation **9** P06020, 2014.

   doi:10.1088/1748-0221/9/06/P06020.

   The results from the first on-sensor annihilations of low energy antiprotons in pixel silicon imaging detector are presented in this paper. Energy deposition due to the annihilation process is examined, as well as the cluster topology. First validation of GEANT4 simulation models for low energy antiprotons in silicon is also performed. A small part of the paper is dedicated to the study of the energy loss of antiprotons in aluminium, validating the simulation with experimental data.

2. N. Pacifico et al. (AEgIS collaboration), *Investigation of silicon sensors for their use as antiproton annihilation detectors*, Nuclear Instruments and Methods in Physics Research Section A: Accelerators, Spectrometers, Detectors and Associated Equipment, in press.

   doi: 10.1016/j.nima.2014.06.036.

   This paper reports on the investigation of the performance of three different silicon sensor technologies (MAPS, micro-strip and 3D pixel) for detection of low energy antiproton annihilations. Clusters and tracks in the detectors associated with annihilation events are characterized and correlated with the features of the sensors, such as the thickness of the active volume and the dynamic range. The work provides an insight of the expected signal from a planar microstrip detector, like the one foreseen for the silicon position sensitive detector in the AE$\bar{g}$IS experiment.

3. A. Gligorova et al. (AEgIS collaboration). *Comparison of planar and 3D silicon pixel sensors used for detection of low energy antiprotons*, IEEE Transactions on Nuclear Science, accepted.

   This paper is based on the presentation given by the author of the thesis at the 2013 IEEE NSS/MIC/RTSD conference. It compares the results obtained with MAPS and 3D pixel detector (the latter originally designed for the ATLAS IBL detector at the LHC) for detection of on-sensor antiproton annihilations. It shows that the annihilation takes place in the first few μm of the silicon sensor and that the charged products of the annihilation can be detected with the same sensor. Comparison with GEANT4 simulation models is reported as well.

Contents

List of Figures

Chapter 1

Introduction

Many profound open questions are still on our way to a better understanding of the universe and its laws. Baryon asymmetry is one of the greatest unsolved problems in modern physics. It is well known that matter and antimatter particles, which have equal mass but opposite lepton and baryon numbers and an opposite charge, are always created in pairs. In other words, energy can transform into matter only when the latter is accompanied by its counterpart, antimatter. The opposite holds true as well: when a particle and its antiparticle are brought together, they annihilate completely into energy. Matter and antimatter are always produced in equal amounts. Still, observations show that the universe is entirely made of matter and there is no significant amount of detectable antimatter [26], even though equal amounts of both should have been formed in the Big Bang.

In 1967 Sakharov showed that CP violation is part of a possible reason why the universe is made of matter rather than equal amounts of matter and antimatter. He proposed a set of three necessary conditions that a baryon-generating interaction must satisfy to produce matter and antimatter at different rates [27]. The discovery of CP violation was made in 1964, when Cronin and Fitch found that kaons transform into their antiparticles (composed of the corresponding antiquarks) and vice versa, but that such transformation does not occur with exactly the same probability in both directions [28]. Nevertheless, this discrepancy proved to be too small to explain the absence of antimatter and two more requirements (from the Sakharov conditions) need to be fulfilled to explain the dominance of matter [27]. CP violation is also predicted to occur in the leptonic sector, e.g. in the oscillations of neutrinos and anti-neutrinos. Although experiments are in search, no observation has been made yet [29]. If discovered, CP violation in neutrinos could also be part of the Sakharov mechanism [30]. Another possibility to generate a baryon asymmetry rests on CPT violation [26].

Attempts to resolve the question of the matter-antimatter imbalance led to many experimental studies in search of a significant difference in the behaviour of matter and antimatter. Experiments at the European Center for Nuclear Research (CERN) made major steps in exploring different antimatter properties and have achieved many significant results. A hitherto unprobed property of antimatter is its coupling to gravity. The AEgIS experiment [31] aims at contributing to finding a possible reason for the antimatter absence in the universe by carrying out the first direct measurement of the gravitational acceleration for the simplest antimatter atom: antihydrogen.

The work in this thesis is part of the development of a silicon position detector for

the AEḡIS experiment, to measure the vertical deflection of a beam of antihydrogen atoms in the Earth's gravitational field. The study is focused on describing different aspects of the antiproton annihilations in silicon using different silicon detector technologies. Although different studies about antiproton annihilation in different materials were carried out in the past years, there is no data available for silicon to date.

The design process of the silicon detector required input parameters that were unknown, e.g. the energy deposited in the detector by an annihilation event or the optimal thickness of the detector. For this reason, the topology of low energy antiproton annihilation events in segmented silicon sensors was investigated through analysis of the beam test data and Monte Carlo simulations. The obtained results contributed significantly in defining the sensor's and readout electronics designs which are currently being submitted for production.

The structure of this thesis reflects the order of the development process of the silicon detector. Theoretical background on the basis of the annihilation of antiprotons with nucleons and nuclei, which is required for the understanding of the annihilation process is presented in Chapter 2. The basis of the silicon detectors operation in general and the features of the different technologies used in this study are given in Chapter 3. A brief overview of past experimental studies of antimatter using silicon detectors is given in the same chapter. Chapter 4 describes in detail the AEḡIS apparatus and the gravity measurement. Conclusion and remarks for further work are given in Chapter 5. After a short introduction in Chapter 6, the scientific results are presented and discussed in three peer-reviewed papers.

Chapter 2

Antiproton annihilation: theoretical basis and brief overview of the experimental data

The development of a detector for antimatter is bound to begin with understanding and describing the annihilation process. This chapter summarizes the current theoretical models for antiproton-nucleon and antiproton-nucleus interactions and gives a brief overview of the results from experimental studies on antiproton annihilation, based on [1], [4], [32] and [33]. This is the basis for the concept of the antiproton annihilation process in silicon which is the key to the work presented in this thesis. The antiproton annihilation process is still not fully understood at a quark level and the microscopic models usually include phenomenological parameters. However, the theoretical treatment of antiproton-nucleon and the antiproton-nucleus interactions is not the scope of this thesis. Experimental data for antiproton annihilation in materials other than silicon are included to provide an image of the expected features of the annihilation process in silicon.

2.1 A brief historical overview of antimatter studies

The existence of antimatter was postulated by Dirac in 1928: a prediction that emerged from the negative energy state solution of an equation that included, for the first time, both quantum mechanics and special relativity [34]. The experimental proof came with the observation of the first positron track in a cloud chamber in 1932 by Anderson, which was produced by a shower of cosmic particles [35]. It took about twenty more years and the invention of the first particle accelerators for the discovery of the two antinucleons: the antiproton in 1955 [36] and the antineutron in 1956 [37] at the Bevatron at Berkeley. Photographic emulsions and cloud chambers were the detector technologies most often used in these experiments. The understanding of the nucleon-antinucleon ($N\bar{N}$) interactions was naturally the next challenge in the antimatter experiments. In the 1960s and the 1970s, data for nucleon-antinucleon annihilations at rest were obtained at the CERN Proton Synchrotron (PS) and at Brookhaven National Laboratory (BNL) using liquid hydrogen and deuterium bubble chambers as detectors, where tracks from the different annihilation prongs were observed. In 1983, when LEAR (Low Energy Antiproton Ring) [38] at CERN came into operation, the study of proton-antiproton ($p\bar{p}$) annihilation was brought to a new level as this facility provided data for antiproton annihilations in different nuclei that are still the main, and often

the only source of experimental results for such interactions. The most significant results concerning the $p\bar{p}$ annihilation at low energies originate from the Crystal Barrel (PS197) [39] and the Obelix (PS201) [40] experiments at LEAR. The Crystal Barrel research studies were mainly devoted to proton-antiproton and deuterium-antiproton annihilations, both at rest and in flight, while Obelix explored the antiproton and antineutron ($\bar{n}$) interactions at rest and with very low momenta, down to 40 MeV/c.

The production of the first antimatter atom, antihydrogen, was reported by the LEAR collaboration at CERN in 1996 [41]. The antihydrogen atoms were produced in flight and were relativistic, excluding any possibility of a precise measurement of their proprieties. Low energy antiprotons were needed for the formation of cold antihydrogen. This led to the successor of LEAR, the Antiproton Decelerator (AD) [42] at CERN, which is operating since 2000 and produces a beam of low energy (5.3 MeV) antiprotons for the various antimatter experiments. The first successful production of cold antihydrogen was reported by the ATHENA collaboration in 2002 [43] and confirmed by the ATRAP collaboration the same year [44]. This achievement opened the possibilities of applying the same spectroscopic techniques already used for studying hydrogen and making precise comparisons between hydrogen and antihydrogen. The first trapping of antihydrogen atoms was carried out by the ALPHA experiment in 2010 [45]. A long-time confinement ($\sim$ 1000 s) was achieved by the same collaboration [46] and is considered as a big step towards precise measurements of the antihydrogen properties and testing CPT invariance with baryons. Another experiment at CERN, ASACUSA, successfully produced hybrid metastable atoms, the so-called antiprotonic helium, which is formed by replacing one of the helium electrons with an antiproton. The ASACUSA collaboration managed to determine the mass of the antiproton to about one part in a billion by two photon laser spectroscopy of the antiprotonic helium [47].

2.2 Antiproton annihilation physics

2.2.1 Antiproton annihilation with nucleons

Annihilation is a process that occurs at the level of elementary particles when a particle comes in contact with its antimatter particle. As a result, new particles are created, conserving the charge, energy and momentum of the system. The particular case of detection of antihydrogen in matter requires knowledge of the theoretical basis of the annihilation of its constituents: the positron and the antiproton. Of these, the electron-positron annihilation at rest is a well defined process and the annihilation prongs are well known. When an electron-positron pair annihilates at rest, the total mass of the particles is converted to two photons, with an energy of 511 keV each, emitted in opposite directions. Any other outcome of this scenario would violate energy and/or momentum conservation. If the annihilation occurs in collisions with sufficient rest-frame energy, then other heavier particles may be produced, such as W^+W^- pairs, muon-antimuon pairs, neutrinos, D-mesons etc [48].

The annihilation process can be translated to nucleons as well. The mechanism of the proton-antiproton, and even more, the neutron-antiproton annihilations are still being actively studied, as not even the rates of the different decay channels are completely

known. Since the nucleon is not an elementary particle, but possesses an internal structure, the annihilation takes place at the quark level. When a nucleon-antinucleon annihilation occurs, all the quark-antiquark pairs do not necessarily annihilate. The complexity of the quark level mechanism is confirmed by the observation of neutron-antiproton and proton-antineutron annihilations [49, 50], where one of the quarks composing the nucleon has no corresponding antiquark in the antinucleon. Quarks are mediated by the strong interaction with gluons as force carriers. Being quarks elementary particles, when a quark and an antiquark annihilate, the total energy of the annihilation is first released in the form of gauge bosons, which, in turn, can be transformed into other particles.

When antinucleons ($\bar{N}$) collide in flight with free nucleons (N), elastic and inelastic processes can occur. Apart from annihilation ($N\bar{N} \rightarrow$ mesons and hyperons) and charge-exchange ($p\bar{p} \rightarrow n\bar{n}$), inelastic reactions ($N\bar{N} \rightarrow N\bar{N}$ plus mesons and hyperons) can also take place [4]. Depending on the energy of the interacting nucleon and antinucleon, different reaction channels are possible. At high energies, multi-particle production dominates the total cross section. The study of the annihilation process at different energies thus gives an insight into the physics of hadronisation. At low momentum (below 1 GeV/c), the annihilation cross section is very large and dominates over the elastic cross section. Having no energy threshold, the annihilation with production of mesons is the most significant process at low energies. The study of antiproton scattering and annihilation at low energies always combines long-range physics, which is described by conventional meson-exchanges, and short-range physics, where direct interaction between quarks and antiquarks takes place.

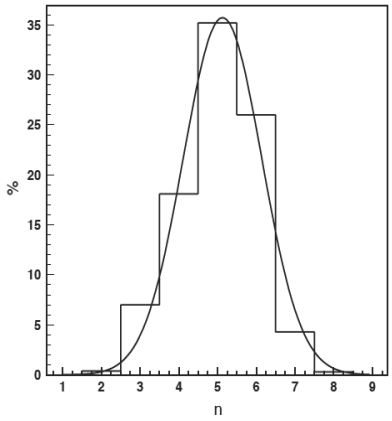

Figure 2.1: Multiplicity distribution of the total number of pions (both charged and neutral) from the Crystal Barrel data [1].

The $N\bar{N}$ annihilation at low energies can be described in simple terms as a process generating a hot, concentrated quark gas with energy equal to the total mass of the annihilating nucleon and antinucleon ($\sim$ 1880 MeV). Data show that the $N\bar{N}$ system evaporates into two to eight pions, with an average of five pions [32]. The total rest mass of the five pions is 5×140 MeV/c^2 = 700 MeV/c^2, so the rest of the en-

	BNL, CERN and Crystal Barrel
2 pions	$0.38 \pm 0.03\%$
3 pions	$7.4 \pm 0.3\%$
4 pions	$18.1 \pm 1.8\%$
5 pions	$35.2 \pm 3.7\%$
6 pions	$23.3 \pm 2.8\%$
7 pions	$3.3 \pm 0.3\%$

Table 2.1: Frequencies of pionic final states in $p\bar{p}$ annihilation at rest, as obtained from combined results from CERN, BNL and Crystal Barrel data [1].

ergy released from the annihilation is distributed as kinetic energy of the pions, with an average of 236 MeV per pion. In the case of low energy $p\bar{p}$ annihilations, more than 95% have a final state composed of pions (π^+, π^-, π^0), and only in a few percent of the annihilations the final state includes kaons. The pions can be produced either directly or through the decay of mesonic resonances (η, ρ, ω). The mean number of produced charged pions experimentally determined depends on which sets of data are included. Most of them report around 1.53 ± 0.03 for each of the charged pions (π^+ and π^-) and 1.96 ± 0.23 per annihilation for neutral pions (π^0) [4]. An extensive summary of the experimental data including three different sources (BNL, CERN and the Crystal Barrel experiment) was made and the frequencies of the pionic final states for the $p\bar{p}$ annihilation at rest were determined. The results are given in table 2.1. The obtained mean multiplicities for charged and neutral pions per annihilation are: 3.05 ± 0.04 for charged pions, 1.93 ± 0.12 for neutral pions, for a total of 4.98 ± 0.35 pions per annihilation. The multiplicity distribution of the total number of pions per annihilation from the Crystal Barrel data, fitted with a Gaussian distribution is given in fig. 2.1. The mean number of pions given by the fitting is 5.03 ± 0.05 and the width is 1.13 ± 0.07 [1].

2.2.1.1 Models for $N\bar{N}$ annihilation

Modelling the $N\bar{N}$ annihilation persists to be a complex task even after more than fifty years of experimental studies. Different approaches are used to describe the $N\bar{N}$ annihilation process. The microscopic approaches are either based on quark models (quark rearrangement model) or on the hadronic representation using baryons and mesons as degrees of freedom (baryon exchange model).

The baryon exchange model describes the $N\bar{N}$ annihilation analogue to electron positron (e^-e^+) annihilation and it was the first model proposed to explain $N\bar{N}$ annihilation mechanism. It mainly presents $N\bar{N}$ annihilaiton as a short-range process mediated by baryon exchange, with a range of the order of $1/(2m_p) \sim 0.1$ fm, where m_p is the proton mass. The model relies on hadronic degrees of freedom and it uses the same meson-baryon couplings from the corresponding nucleon-nucleon potential [51, 52]. These couplings are specified by the interaction Lagrangians which define well the basic dynamics of baryon exchange models. Nevertheless, since the assumed range is very small (0.1 fm), large form factors have to be introduced in the model to take into account the sizes of the intermediate off-shell mesons and baryons participating in the annihilation process [1]. The more recent developments of the baryon exchange

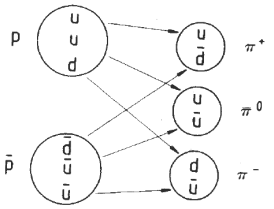

Figure 2.2: A scheme of one possible rearrangement of the quarks into three pions due to a $p\bar{p}$ annihilation [2].

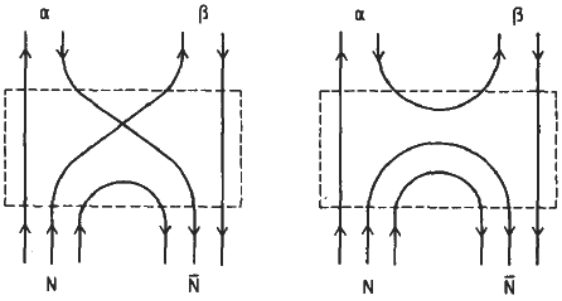

Figure 2.3: Annihilation mechanisms at quark level for nucleon-antinucleon annihilation into two mesons. Left: $q\bar{q}$ annihilation followed by rearrangement (R-process); right: annihilation of two $q\bar{q}$ pairs and a pair creation (A-process) [3].

model include the interactions between the initial and the final state of the annihilation [53, 54]. The main drawback of these models is that they only describe final states with two mesons and are not able to reproduce all annihilation effects. However, when an additional phenomenological optical potential, independent of the states and the energy is added, the correct annihilation cross sections and a good description of nucleon-antinucleon scattering can be obtained [55].

The quark models, on the other hand, deal with constituent quark degrees of freedom. Their advantage over baryon exchange models is that they naturally contain the spatial extension of the hadrons, which results in a small number of parameters because no additional form factors or coupling constants are needed.

The mutual annihilation of $N\bar{N}$, according to the quark model, does not necessarily translate into actual annihilation of all the incoming quarks and antiquarks, but undergoes different quark rearrangements into quark-antiquark ($q\bar{q}$) pairs and follows different annihilation mechanisms. Hence, some of the incoming quarks and antiquarks might annihilate, and new quark–antiquark pairs might be created.

In the quark rearrangement model [56, 57], the constituents of the nucleon and the antinucleon (quarks and anti-quarks) re-couple to reach a final state that consists of three mesons which are combinations of π, ρ, ω and η mesons. Hence, the total number of quarks does not change. The reaction is the following:

$$(qqq) + (\bar{q}\bar{q}\bar{q}) = (q\bar{q}) + (q\bar{q}) + (q\bar{q}), \tag{2.1}$$

A scheme of one possible mode of the quark rearrangement and their re-coupling into three pions is given in fig. 2.2. Although this model has successfully explained the existing experimental data for pion multiplicity, it does not explain the annihilation into two mesons and to mesons other than the aforementioned ones. The two-meson channels are estimated to represent $\sim 10\%$ of the total annihilation events.

The original model of quark rearrangement was further developed with a focus on the three-meson decay models for $N\bar{N}$ annihilation at rest, by taking into account the existing experimental data. Part of the experimental data were used for suitable adjustment of seven parameters to obtain a quantitative fit to the data. The comparison of the results with data that were not used in the fitting procedure tested the model and

showed good agreement in the decay rates for different channels between data and the model [58]. The conclusion was that the quark rearrangement model with the spatial overlap function can provide a good description for $\sim 90\%$ of the branching ratios for the $N\bar{N}$ annihilation at low energies [59].

In the case of low energy proton-antiproton, the annihilation into two mesons has been described with a non-relativistic quark model, where at least one quark-antiquark pair annihilates to form two mesons in the final state [3]. Two basic diagrams are considered: the partial rearrangement (R-process, where one quark-antiquark pair is annihilated and the remaining two pairs are rearranged into two mesons, and the annihilation (A-process), in which case two quark-antiquark pairs are annihilated, but another pair is created from the annihilation energy and forms two mesons with the remaining pair from the incoming nucleon and antinucleon. These schemes are presented in fig. 2.3. Depending on the mechanism and the number of mesons in the final states, different schemes are possible. Abbreviations A2, A3, R2, R3 are used to refer to the annihilation schemes where two or three mesons or meson resonances are produced, either by annihilation of the quarks or rearrangement. The contribution from the different processes depends on the energy of the incoming antiproton. The A-process dominates at higher energies because of the increased momentum difference between the initial and the final state. For the $p\bar{p}$ annihilation at rest into three mesons, both rearrangement and annihilation models explain with similar reliability the branching ratios of the decay products. In the case of the decay into a two-meson final state, the annihilation model provides a better description and gives a better agreement with the experiment [60].

Other approaches describe the $N\bar{N}$ annihilation phenomenologically, in terms of geometry and statistics. This is possible because the data show that, empirically, some of the basic features of the annihilation are of statistical nature, such as the pion multiplicities that are described by a statistical (Gaussian) distribution (see fig. 2.1), or the momentum distribution of charged pions from $p\bar{p} \to \pi^{\pm}X$, which can be well approximated by a Maxwell-Boltzmann distribution. One of the most significant and most successful statistical model is the two meson doorway model [61], which assumes that the $N\bar{N}$ annihilation occurs through the formation of a two-meson intermediate state which subsequently decays into the final state that consists of pions and/or kaons. This assumption is supported by the fact that a large, but quantitatively still unknown fraction of all annihilation channels actually proceed via two-meson intermediate states. This shows that the resulting energy density of the annihilation process is preferably stored in a minimal number of massive meson resonances, rather than being transformed instantly into kinetic energy of pions and kaons. The two-meson doorway model provides a better description for the $N\bar{N}$ annihilation in flight and it can successfully reproduce many of its features for a wide range of antiproton momenta [1]. As for the annihilation at rest, the model is able to predict the rates for the decay channels obtained experimentally in the correct order of magnitude.

In general, a complete theoretical framework for the $N\bar{N}$ annihilation at quark level is very hard to build due to the complexity of the annihilation process, which is likely driven by both the quark dynamics and by the well established hadronic interactions. A precise determination of the rates for all annihilation channels is almost impossible to achieve, as there is a certain possibility of interferences between the primarily formed mesons (from the $q\bar{q}$ pairs) and the mesons built from final-state interactions.

2.2.2 Antiproton annihilation with atomic nuclei

In order to understand the annihilation signature of antiprotons in silicon, and therefore the expected signal coming from the silicon position detector in AEgIS, a brief description of the interactions of low energy antiprotons with nuclei are presented in this section. A brief overview of the theoretical models as well as a summary of the existing data for different nuclei is also given. The lack of experimental data for antiproton annihilations in silicon in literature was one of the motivations for the work done in this thesis.

In general, antiprotons can interact with the nucleus in flight or at rest. When the interaction occurs in flight, the processes that can take part are: elastic scattering, inelastic reactions (nucleus excitation, pick-up and break-up reactions, etc.), charge exchange reaction, annihilation like on free nucleons and interaction between the annihilation products in the final state and the residual nucleons (e.g. mesons may be absorbed and the residual nucleus may suffer fragmentation). Exploring the annihilation of low-energy antiprotons in silicon makes the annihilations at rest the primary process of interest.

For energies in the order of MeV and down to $\sim$ 10 keV, when antiprotons pass through the material, they loose their energy according to the Bethe-Bloch formula (see sec. 3.1), until they are finally stopped. When antiprotons are brought to rest, they are captured into bound atomic orbits with high principal quantum number n: a highly excited $\bar{p}$-atom is formed and cascades downward, first by emission of Auger electrons and subsequently by X-ray emission, reaching orbits that are close to the nuclear surface. At this point, the antiproton-nucleus interactions are mediated not only via long-range Coulomb interactions, but also through short range, strong nuclear forces, where the absorption is dominant. As a result, the antiproton interacts only with the nuclear surface, at a maximum depth where the density is 10% of the central nuclear density [62]. The annihilation with a nucleon at the nuclear surface takes place when the antiproton reaches the levels between $n = 9$ (for lead) and $n = 4$ (for oxygen), depending on the charge of the nucleus. As explained in section 2.2.1, the antiproton-nucleon annihilation at rest releases an energy of 1880 MeV and produces on average five pions. They are emitted isotropically, so different scenarios for the final state of the annihilation process are possible. Some of the pions escape without interacting with the nucleus. In some cases even all the pions can leave the nucleus through quasi-free scattering or pion-nucleon charge exchange, which results into weakly excited compound nucleus which de-excites by emission of one or two nucleons or only γ rays.

Nevertheless, depending on the size of the nucleus, different probabilities hold for the number of the primarily produced pions that will penetrate inside the nucleus. The energy of these pions ($\sim$ 230 MeV) is in the region of Δ resonances and they have short range, thus transferring a large fraction of this energy to the nucleus, but only small amounts of linear and angular momenta. The interaction between the pions and the nucleus leads to an intranuclear cascade, during which the nucleus can be heated to very high temperatures (up to several hundred MeV [62]) and exotic states such as fireballs, special quark-gluon plasma, hot nuclear gas and hyperons may be produced [63]. The antiproton-nucleus interaction is successfully described by the intranuclear cascade model (INC) [64], which reproduces correctly the momentum distribution of pions emerging from $\bar{p}$-nucleus annihilation [65].

The process can result in production of additional pions and fragmentation of the

nucleus with emission of protons, neutrons, deuterons (d), tritions (t) or alpha particles. In some cases the annihilation is accompanied by the emission of K^+K^- pairs or even a Λ hyperon, which can be produced in a secondary reaction between K^- and the residual nucleus [66].

The residual nucleus after the annihilation has nucleon deficiency and is in most cases radioactive. The decay mechanism of the residual nucleus is determined by the excitation energy deposited in it: if this energy is ≤ 2 MeV/nucleon, the decay will most probably occur by successive nucleon evaporation and fission that can, depending on the mass number, A, result in wide spectrum of residual nuclei; if the excitation energy is close to the binding energy per nucleon (≥ 5 MeV), a phase transition of the nuclear matter into liquid-gas type can occur, resulting in an explosive decay of the residual nucleus (multifragmentation) [67]. The outcome of such a process is a multiple production of nuclear fragments [68].

Both the evaporation and the multifragmentation processes are described with statistical models. For the evaporation of moderately excited nuclei, the Weisskopf model is used to reproduce the emission of $n, p, d, t, {}^3He, {}^4He$ [69]. In the statistical model of the multifragmentation of hot nuclei, the excitation energy of the fragments is calculated based on the liquid-drop model description of the properties of hot fragments to finite temperatures. The lightest fragments ($d, t, {}^3He, {}^4He$) are assumed to be formed in their ground states [70–72].

The annihilation of antiprotons on heavy nuclei can produce the emission of a large number of nucleons from the parent nucleus. The energy spectra and the multiplicities of the emitted particles give an insight of the intranuclear cascade process. Experimental results show that up to 11 protons and 30 neutrons can be produced in the annihilation with ^{95}Mo and about 50 nucleons in total from annihilation of antiproton with an ^{165}Ho [73].

Non-conventional processes, such as annihilation involving more than one nucleons can occur in the antiproton-nucleus reaction. The final states of these two body annihilation channels, the so-called Pontecorvo reactions [74], are not attainable from annihilations with free nucleons. While in the ordinary annihilation of an antiproton with a nucleon at least two mesons are created, when the annihilation takes place in a nucleus, it is possible to create only one meson or possibly none at all. This kind of events have been observed with a very small rate ($\sim 10^{-5}$) [75, 76]. The theoretical modelling of these processes is not straightforward, as the calculated probability of Pontecorvo reactions is found to be strongly dependant on the choice of the wave functions. The rates predicted by the two-step model are two to three order of magnitudes smaller compared to the experimental data [77].

An experiment at LEAR [78, 79] provided data on the multiplicity and the spectra of the charged particle emitted from antiproton annihilation at rest in different nuclei, with ^{12}C and ^{40}Ca being the closest to the element of interest in this study, silicon. An extensive study of the charged particle emission due to antiproton-nucleus annihilations for different materials was performed. The spectra and the yields of H and He ions emerging from annihilations of stopped antiprotons in targets made of ^{12}C, ^{40}Ca, ^{63}Cu, ^{92}Mo, ^{98}Mo and ^{238}U were measured for different ranges up to 200 MeV with a silicon and a germanium telescope. The measurements were carried out with antiprotons with momentum of 202 ± 1 MeV/c that were slowed down by means of polyethylene wedges adjusted in a way that the antiprotons would stop in the target. Apart from protons,

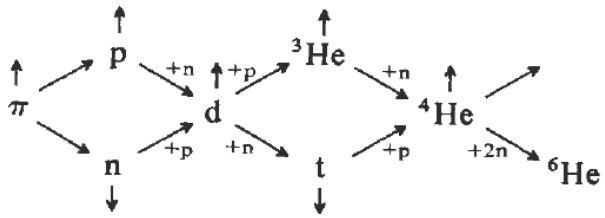

Figure 2.4: A graphical scheme of the pickup model. Vertical arrows mean that the particle escapes. Other arrows denote strikes by a pion or pickup of a proton or neutron [2].

deuterons, tritons, ^{3}He and ^{4}He, whose energy spectra were measured, ^{6}He, ^{8}He and Li ions have also been observed and their total yield per 100 antiproton annihilations was determined. The results led to the conclusion that protons are produced by direct emission and evaporation, whereas tritons are mostly emitted directly. It was proven that the shape of the spectra is independent of the target mass number A, which is in accordance with results from fast proton and fast pion-nucleus reactions.

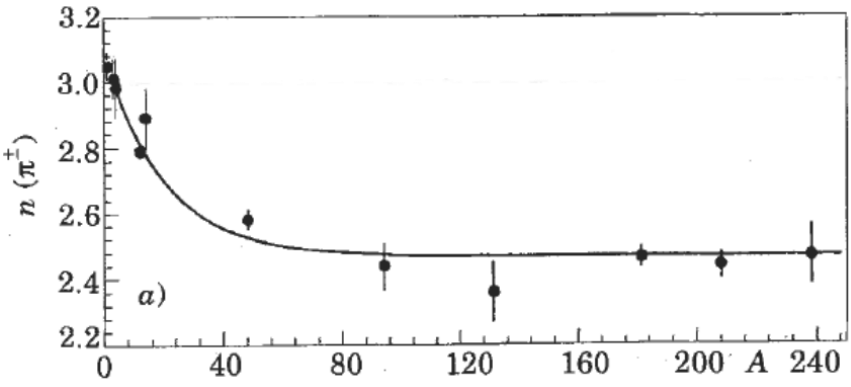

Figure 2.5: Mean multiplicity distribution of $\pi^{\pm}$ emitted from antiproton annihilation on nuclei with different mass number A. The solid line is the result of a best-fit calculation [4].

The experimental results for the yields showed that ^{3}He yields increase by a factor of about 1.5 from ^{12}C to ^{238}U and the ^{4}He yields about a factor of 5 [78]. This effect can be understood with a simple pickup model [2], according to which the formation of heavier emitted particles is a consecutive process. The method is graphically presented in fig. 2.4. Fast pions produced from the antiproton annihilation hit nucleons that can either be knocked out of the nucleus or go through multiple scattering, picking up on the way other protons and neutrons and forming heavier particles such as d, t, ^{3}He and ^{4}He. The model allows calculation of the yield ratios using only the number of protons Z, the number of neutrons N, and one free parameter r, which represents the average pickup probability per average distance in the nucleus. It is assumed that protons and neutrons have similar pickup rates. A good agreement between experimental data and

this model has been reported for ^{4}He/^{3}He ratio for annihilation of antiprotons with nuclei with different *Z*. The only exception is the ^{238}U, where the calculated value was too large. It is assumed that the reason for this discrepancy might be found in the omission of the Coulomb barrier in the calculations. Due to this barrier, the tritions would rather escape than pick up a proton, hence the smaller number of ^{4}He particles in the measurement and the larger ratio in the model calculations [78].

The production yield of pions has to our knowledge never been measured for antiproton annihilations in silicon, but an extrapolation was made based on the existing experimental data for other nuclei [4]. Measurements from different experiments with different antiproton momenta (0-900 MeV/c) were summarized and the obtained results are shown in fig. 2.5. Starting from $A = 2$, the number of emitted charged pions per annihilation decreases quickly as A increases, for $A < 80$. Above this value $n(\pi^{\pm})$ is almost constant. According to this plot, the expected number of charged pions produced from an antiproton annihilation in silicon is in the range of 2.5 to 2.8. In the present work, the available experimental results for the two elements closest to silicon, ^{12}C and ^{40}Ca, were compared with the two GEANT4 models in use for simulations of antiproton annihilations in silicon. The spectra of the emerging charged particles from the annihilations in silicon were simulated with the SRIM package [80].

Chapter 3

Silicon detectors and detection of antimatter

Solid state materials have been used for building particle detectors since the 1970s, when the ionization-drift principle was adopted from gaseous detectors. The novel concept consisted of detecting charged particles in solid state detectors by exciting the electrons of the atoms and generating free carriers in the volume of a solid material, instead of ionizing a gas. Due to their high material density, these detectors produce a large number of charge carriers, which, combined with the possibility of fine segmentation allow for good position resolution. The fast readout, great robustness, simple handling and easy-manageable infrastructure are some of the advantages that make solid state detectors preferable over gaseous ones. Silicon, germanium and diamond are the most commonly exploited materials for the production of solid state detectors, but also compound materials like GaAs are used.

Silicon is the most commonly employed material in trackers in high energy and nuclear physics experiments (for example it is employed in the LHC experiments). Silicon was as well chosen for the construction of the AEgIS position sensitive detector: challenging requirements like the high position resolution ($10-13$ μm) and the cryogenic operation (77 K or lower) encouraged a development from a well established baseline technology [31]. This thesis work explores, for the first time, the use of silicon segmented sensors for direct detection of quasi-static antihydrogen [80, 81]. In this chapter, an overview on the general characteristics of silicon sensors, based on [5], [82], [83] and [84] is presented. Section 3.4 addresses the issues specific to antimatter detection, giving an introduction to the studies presented in the following part of this thesis.

3.1 Interaction of charged particles with matter

The *signal* induced in a particle detector is generally produced by the energy loss by the particle inside the sensitive volume of the detector. For this reason, when building a particle detector, the latter has to be designed taking into account the type and the energy of the particles which should be detected. As mentioned in Chapter 2, the detection of antiprotons is based on the detection of the annihilation products. This section will explain the mechanism of energy loss by a generic charged particle. The energy loss (dE/dx) for some of the annihilation products that are most relevant to the annihilation detection in silicon material is shown in fig. 3 of [80], which can be found in Chapter 7 of this thesis.

Symbol	Definition	Value (or units only)
$\frac{dE}{dx}$	energy loss per unit distance	MeV $g^{-1}cm^2$
r_e	classical electron radius	2.817 x 10^{-13} cm
m_e	electron mass	9.11 x 10^{-31} kg
N_a	Avogadro's number	6.022 x $10^{23}mol^{-1}$
I	mean excitation potential	eV (137 eV for Si)
Z	atomic number of absorbing material	14 for Si
A	atomic weight of absorbing material	28 for Si
ρ	density of absorbing material	2.329 $g \cdot cm^{-3}$ (at 0°C, 101.325 kPa)
z	charge of the incident particle	e
β	v/c of the incident particle	
γ	$1/\sqrt{1-\beta^2}$	
δ	density correction	eV
C	shell correction	eV
W_{max}	maximum energy transfer in a single collision	eV

Table 3.1: Parameters of the Bethe-Bloch formula.

In general, when charged particles cross matter, they interact with the atoms of the material and there are mainly two processes distinguished: inelastic collisions with the atomic electrons (referred to as *electronic*) and elastic scattering from the nuclei (referred to as *nuclear*). Other processes like nuclear reactions or bremsstrahlung can also occur, but their rate is much smaller and their contribution to the overall energy loss of the crossing particle can here be neglected. The energy transfer from the incident particle to the target material is dominated by the collisions with the atomic electrons; this is due to the small energy of the crossing particle compared to the mass of the nuclei of most materials. The maximum kinetic energy that a particle of mass M can transfer to an electron is

$$W_{max} = \frac{2m_e c^2 \beta^2 \gamma^2}{1 + 2\gamma m_e/M + \left(m_e/M\right)^2}. \tag{3.1}$$

Depending on their mass, particles can be considered as *heavy* if their mass is large compared to the rest mass of the electron (alpha particles, nuclear fragments etc.) and *light*, when their mass is comparable to the electron's mass (e.g positrons). For $M \gg m_e$, the maximum kinetic energy in eq. 3.1 becomes $W_{max} \approx 2m_e c^2 \beta^2 \gamma^2$. The rate of ionization loss for a charged particle in matter is given with the Bethe-Bloch formula, as shown below [82]:

$$-\frac{dE}{dx} = 2\pi N_a r_e^2 m_e c^2 \rho \frac{Z}{A}\frac{z^2}{\beta^2}\left[\ln\left(\frac{2m_e\gamma^2 v^2 W_{max}}{I^2}\right) - 2\beta^2 - \delta - 2\frac{C}{Z}\right]. \tag{3.2}$$

The parameters used in this formula are given in table 3.1.

C, the *shell* correction term becomes important at low energies. It corrects the assumption associated with the Bethe-Bloch formula that the velocity of the incident

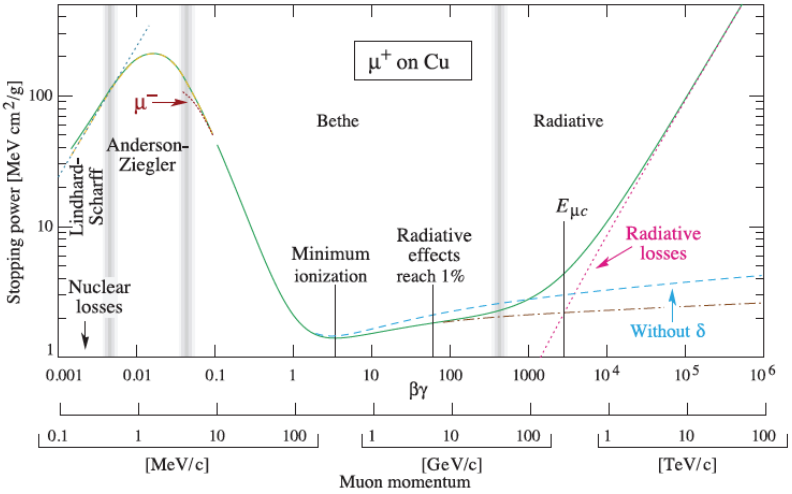

Figure 3.1: Stopping power for positive muons in copper as a function of $\beta\gamma = p/Mc$ over nine orders of magnitude in momentum (12 orders of magnitude in kinetic energy). The solid curve indicates the total stopping power. The short dotted lines labelled μ^- indicate the so-called Barkas effect - the dependence of stopping power on the charge of the crossing particle at very low energies. Red dotted line illustrates the energy loss due to radiative processes for muons. The vertical bands indicate the different regions discussed in the text; only in the Bethe region, the mean energy loss is a function of β alone [5].

particle is much larger than the orbital velocity of the bound electrons in the medium. In the case where the particle's velocity is comparable or smaller than the target electron velocity, the hypothesis that the electrons are stationary breaks down and the Bethe-Bloch formula can not give accurate description of dE/dx (if this correction is not taken into account). At such small energies the electron capture process is also possible. The shell correction is usually small and it is calculated by evaluating the particle's interaction with each electronic orbit. It also decreases very rapidly with increasing energy.

The contribution of the *density* correction term, δ, is connected to the polarization effect, as the electric field of the incoming particle can polarize the atoms along its path. Unlike the shell correction, it becomes significant at high energies (high γ, large velocity of the particle) because the transversal electric field, and subsequently, the interaction cross section, increases. As a result, the electrons that are far from the particle's track will also feel the electrical field, but will be shielded from its full intensity. Due to this shielding, collisions with the electrons far from the path will give less contribution to the energy loss than expected and will effectively cut off the long range contribution. The density correction depends on the density of the material because the induced polarization is greater in condensed materials than, e.g. in gasses.

The Bethe–Bloch formula is valid in the region $0.1 \lesssim \beta\gamma \lesssim 1000$ for materials with intermediate Z with an accuracy of few percent. A graphical representation of the stopping power for positive muons in copper as a function of the muon momentum is

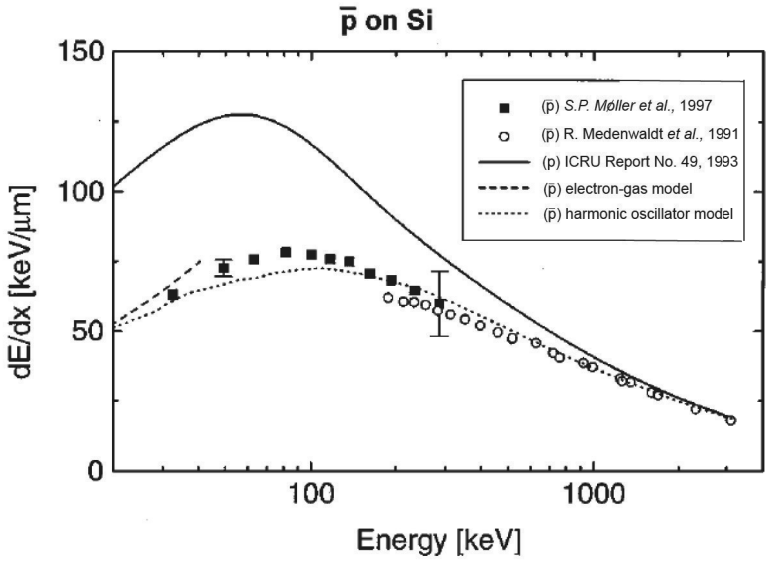

Figure 3.2: Measured stopping power for antiprotons in silicon compared to proton data and to theoretical models. The symbols denote the experimental data from [6] and [7]. The solid curve shows proton data taken from [8]. The dashed curve represents the antiproton stopping power in silicon predicted by the electron-gas model [9], whereas the dotted curve depicts the antiproton stopping power predicted by the harmonic oscillator model.

given in fig. 3.1. For very low energies there are higher order corrections that need to be included, such as the Bloch correction (proportional to Z^4). Another important correction in the low energy region is the Barkas correction (proportional to Z^3), which refers to an effect that was first discovered in 1956: a difference in the range between negative and positive pions, with the negative pions having 0.36% longer range [85]. Barkas explained the discrepancy in the range of particles having the same mass and velocity, travelling in the same target and differing only by the sign of their charge: the effect arises because of the different behaviour of the atomic electrons in the target material with respect to the charge of the incoming particle. When the velocity of the particle is very low, these electrons have enough time to move. Positively charged particles pull the electrons towards their path, while the negative particles repel them. This may be interpreted as an increased local electron density for the positive particles, and a decreased local electron density for the negative ones. At higher energies, the Barkas correction becomes negligible because a fast moving particle is not able to induce movement of the target electrons.

This effect is of great importance for understanding and describing the stopping power of the negatively charged particles, such as antiprotons. For example, experimental data for antiprotons in silicon showed that the stopping power for 0.188 MeV antiprotons is 32% lower than for the protons with same velocity [6]. Another study of antiprotons with energies from 50 to 700 keV found that their stopping power near the electronic stopping power maximum, in both light and heavy targets, is 30-40% lower

than the corresponding stopping power for protons [7]. A combined plot from existing experimental data for antiprotons, protons and two theoretical models is given in fig. 3.2. The data from both measurements are consistent in the overlapping region, with a discrepancy within the experimental errors. The antiprotons experience a maximum stopping power at an energy ($\sim$ 100 keV) which is slightly higher than the one for the proton's maximum. As for theoretical models, the harmonic oscillator model described in [7] provides a good agreement with the data, especially at higher energies. On the other hand, the electron-gas model gives a very good description in the low-energy region, where the stopping power seems to be proportional to the velocity of the particles. The stopping power was calculated for energies below the stopping maximum by describing the target electrons as a degenerate, homogeneous Fermi gas. The calculations showed that the energy loss rate for antiprotons in silicon and germanium is less than half of the rate for protons [9]. The necessity of using models arises from the deficiencies of the Bethe-Bloch formula even when corrections are included. In these models, the atoms in the target material are treated as an electronic gas or as harmonic oscillators and such calculations are used to better understand the slowing down process and the interactions between the projectile particle and the target atoms.

When the corrections at low energies are taken into account, the Bethe-Bloch formula is accurate to $\sim 1\%$ down to $\beta \approx 0.05$, or, translated into energy, about 1 MeV for protons [5]. In the very low energy region ($\beta\gamma < 0.1$), when the orbital electrons of the absorption medium can not be considered *free* compared to the incoming particle, the energy loss reaches a maximum and drops rapidly toward lower energies, as seen in fig. 3.1. For $0.01 < \beta\gamma < 0.05$, there is still no theory that provides a satisfactory description [5]. At such low energies the best description for protons is provided by the phenomenological fitting formulae developed by Andersen and Ziegler [86]. Lindhard has described the electronic stopping power for particles of even lower velocities, $\beta < 0.01$, which is approximately equal to the velocity of the outer atomic electrons. In this case, the electronic stopping power is proportional to β [87]. For extremely low energies, e.g. protons of energy less than several 100 eV, the total energy loss is mostly due to non-ionizing nuclear recoil [87].

As the energy rises, the $1/\beta^2$ term increases rapidly and dominates the dE/dx, which, in turn, decreases, and for $\beta \approx 0.96$ ($\beta\gamma \approx 3$) the function reaches its minimum. When a particle's energy loss is in the minimum of the Bethe–Bloch formula (or $\beta\gamma = 3-4$), the particle is known as a *minimum ionizing particle* (m.i.p. or MIP). A relativistic rise of dE/dx occurs for $4 < \beta\gamma < 200$: this is due to the relativistic extension of the transversal electric field because of the Lorentz transformation ($E_y \rightarrow \gamma E_y$). The energy loss in this region increases as $\sim \ln(\beta\gamma)^2$. For large values of $\beta\gamma$ (> 200), dE/dx becomes saturated and the energy deposit reaches a so-called *Fermi plateau*. As explained before, polarization effects arise that limit the field extension and density corrections become important. At extremely high energies radiative effects become more important than ionization losses. The radiative losses are important for muons and pions in general, because they do not only lose energy by ionization but also by radiative processes, such as bremsstrahlung, direct production of e^-e^+ pairs, and photonuclear interactions. The energy loss which is due to these processes is shown by the dotted red line in fig. 3.1.

3.2 Semiconductor detectors

3.2.1 General properties of semiconductors

Solid state materials can be divided into three main groups: conductors, insulators and semiconductors, a classification that is based on the conductivity of the material, which is determined from the distribution of their atomic electrons into the *energy bands*. The energy bands are ranges of energy levels which are very close to each other. The electronic band structure is a result of the overlapping electron orbitals of neighbouring atoms in the lattice. According to the Pauli principle, two identical fermions can not be in the same quantum state. Hence, when two atoms are brought very close to each other, these states experience a small shift, thus generating new energy levels which differ very little. When this process is applied to the many atoms in the large periodic lattice, the result are shifting energy levels that form energy bands. The occupancy level of those bands determines the conductivity of the material. A band will contribute to conduction only if it is partially filled with electrons or empty, since a completely filled band would not be able to provide free carriers to move and to generate current. In conductors, there is an overlap between empty and filled bands, which allows for excited electrons to move freely through the empty band when a voltage difference is applied. On the other hand, in insulators there is a large (> 9 eV) energy gap (forbidden energy levels) between the conduction band (which is empty) and the valence band (completely filled), which prevents electrons from being excited to the corresponding energy levels in the conductive band. However, in semiconductors this band-gap is small enough so that free carriers can be easily produced by energy deposited from a particle crossing the solid material. A material is conventionally classified as a semiconductor if the energy gap is at most ~ 4 eV [88].

At $T = 0$ K all the electrons are tightly bound to the atom and occupy the lowest possible energy level, so in absence of movable charge carriers the semiconductor behaves like an insulator. At $T \neq 0$ K the electrons experience thermal excitation, which, for the electrons in the outer shell can be enough to be able to move to the energy level in the conduction band. The energy distribution of the electrons at temperature T is given by the Fermi distribution:

$$f(E) = \frac{1}{1 + e^{\frac{E - E_F}{kT}}}, \tag{3.3}$$

where k is the Boltzmann constant and E_F is the *Fermi Energy*. At 0 K, all available levels with $E < E_F$ are filled, and all levels for $E > E_F$ are empty. When an electron jumps to a higher energy level it leaves a vacancy in the lower band (valence band). The absence of an electron (called a *hole*) behaves like a positively charged virtual particle, which moves in opposite direction with respect to the electrons, when an electric field is applied. In a pure semiconductor, the concentration of electrons and holes is the same (generation of carriers is due to thermal excitation only) and it is known as *intrinsic* semiconductor. The intrinsic carrier concentration at temperature T is

$$n_i = C \cdot T^{3/2} e^{\frac{-E_g}{2kT}}, \tag{3.4}$$

and can be increased by introducing impurities (small amount of another element) into the lattice of the semiconductor. This process is called doping, while the added element is known as *dopant*.

In the lattice of group IV semiconductors (e.g. silicon, germanium etc.), each atom is bonded to four other neighbouring atoms by sharing four electrons from its outer shell, creating four covalent bonds (one with each neighbouring atom). When an atom from another element from group V (e.g. phosphorus), which has five electrons in the outer shell, is introduced in the lattice of such a semiconductor, it bonds to four neighbouring atoms creating four covalent bonds, leaving behind an electron that is a potential carrier. This type of dopant is called donor. When a sufficient number of donor atoms is added, an excess of electrons is produced. The resulting semiconductor is known as $n-type$. In the same way, an excess of holes can be obtained by adding a group III dopant (with three electrons in the outer shell, e.g. boron), known as acceptor. The resulting semiconductor is of $p-type$, with holes as majority carriers.

3.2.2 p-n junction

The operation principle of a semiconductor detector is based of the p-n junction as their most fundamental structure. It is created by bringing two semiconductors of different types into atomic contact. When this occurs, a diffusion process is triggered in both directions: the electrons from the n-type semiconductor move to the p-type bulk, and the holes from the p-type semiconductor go in the opposite direction. In this way, a certain region around the physical junction is depleted from charge carriers of both types. While both, the p-type and the n-type bulks are neutral, the depletion region contains a space charge that creates an electric field which prevents further diffusion. The corresponding potential difference is known as *built-in potential*. A schematic overview of the p-n junction in thermodynamic equilibrium together with the plots for the charge density, the electric field and the induced potential difference is given in fig. 3.3

The width of the depletion layer can be changed by applying an external electric potential. If the p-n junction is connected to forward bias (n-type to the negative terminal, p-type to the positive one), the space charge region gets smaller. On the contrary, if we apply a bias which has the same polarity as the built-in potential (reverse bias, where n-type is connected to the positive terminal, p-type to the negative one), the depletion region extends. By increasing the reverse bias it is possible to deplete the whole semiconductor volume, all the way to its edges. This is called *full depletion*. Further increase of the bias will eventually result in a breakdown. But even when the junction is fully depleted, there is still a small current flowing through. This is due to two effects: the motion of the minority carriers that move towards the depletion region from each side of the bulk and the generation of minority carriers that occurs in the existing electron-hole (e-h) pairs generation centres within the depleted region. The generation of minority carriers is possible due to the energy levels located close to the middle of the band gap, which appear because of the crystalline defects of the bulk. Here, the e-h pairs are created only by thermal excitation. The component of the leakage current evoked by this effect is dominant over the component coupled to the motion of minority carriers, so the total leakage current is strongly dependent on the temperature and becomes negligible (order of nA) at cryogenic temperatures.

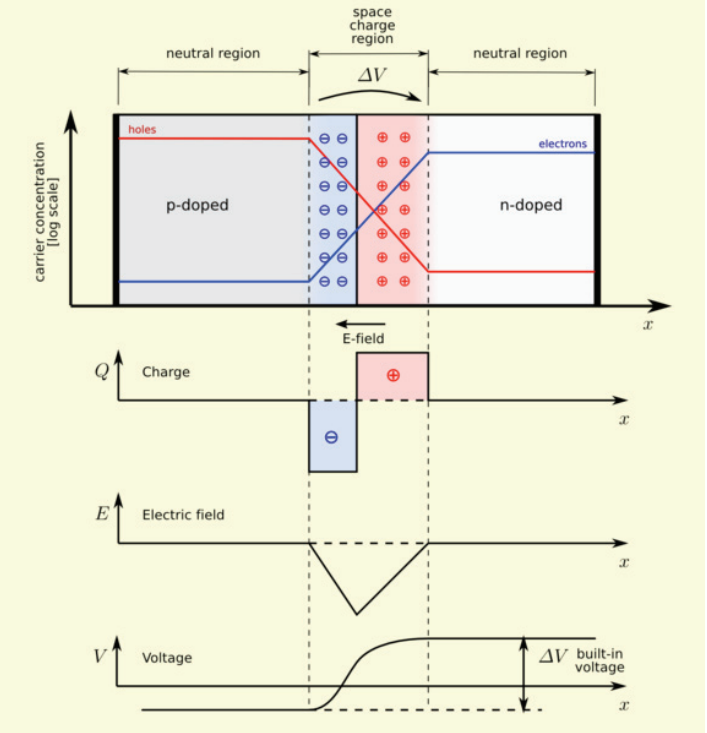

Figure 3.3: A schematic overview of a p-n junction together with the plots for the charge density, the electric field and the potential [10].

3.2.3 Silicon as detector for charged particles

The detection of charged particles in silicon is possible due to the electron-hole pairs that are created when a crossing particle deposits part of its energy in the bulk and excites some carriers from the valence to the conduction band. In order to establish a signal from the collected charge that is only due to the energy deposited from the incoming particle, and not from thermally created e-h pairs, the free carriers must be removed from the detector. The most convenient way to separate the signal is to use the depletion volume of a reversed bias p-n junction as an active volume of the silicon detector. Under the effect of an external electric field, the depletion zone, free of charge, can extend to the physical edge of the bulk. When the charge carriers that are generated by the incident particle drift under the effect of the applied electric field, they induce a signal on the electrodes. If an information on the spatial position of the particle is required, at least one of the electrodes needs to be segmented. A schematic overview of the principle of particle detection in silicon sensors is given in fig. 3.4.

Silicon is a material with a low ionization energy, i.e. its band-gap is only 1.12 eV. Nevertheless, the average energy required to produce one electron-hole pair in silicon is 3.6 eV, where the remaining energy dissipates into phonon excitations. This is the minimum energy that a crossing particle needs to release in order to be detected. For

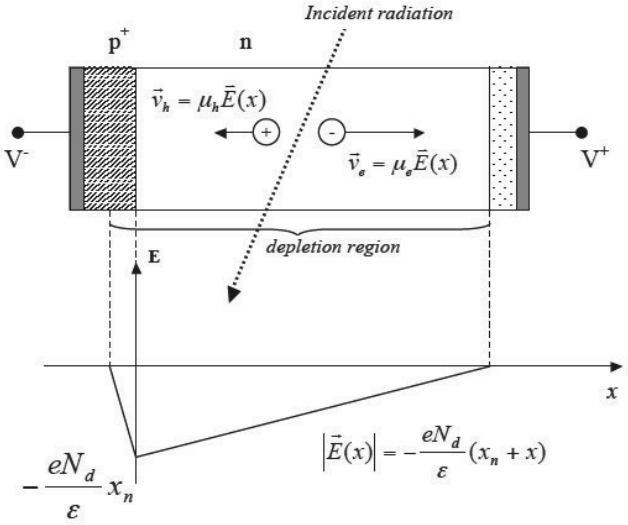

Figure 3.4: A schematic overview of a particle detection in a silicon sensor. The label p^+ designates a heavily doped region, allowing extension of the active volume in only one type of bulk. The thinner p^+ region allows to place the readout electrode closer to the point where the junction starts (where the field is higher) for more efficient charge collection.

comparison, in gaseous detectors the minimum required energy to ionize a gas atom is $\sim$ 30 eV. Silicon has a low Z ($Z = 14$) which results in limited multiple scattering. On average, a minimum ionizing particle will produce 80 electron-hole pairs per µm of silicon [88]. Frequently silicon detectors are used for the detection of highly ionising particles, with energy depositions exceeding this figure by several orders of magnitude. Such particles are for example typical products of hadron annihilations as will be shown further on in the work presented here. As soon as the carriers start to move through the detector, they induce a time-varying charge on the electrodes, creating a current (charge is not "collected" when the carriers reach the electrodes). The induced current intensity depends on the coupling between the charge and the electrodes and it is described by the Ramo's theorem [89]. The instantaneous current induced on a given electrode is:

$$i(t) = -q\mathbf{v}(\mathbf{t}) \cdot \mathbf{E_W}, \tag{3.5}$$

where q is the charge moving under the electric field with velocity $\mathbf{v}(\mathbf{t})$ and $\mathbf{E_W}$ is the weighting field, a vector dimensionless quantity which is calculated from the resulting electric field when a unitary bias is applied on the concerned electrode and all the other electrodes in the sensor are grounded.

3.3 Silicon detector technology

Although several sensor geometries are achievable by properly segmenting the readout electrodes, this work will address two main configurations: strip and pixel sensors. Pixel detectors can be divided based on the geometry of the electrodes into planar and 3D detectors. The most classical configuration implements the readout of the sensor in a silicon die independent from the active detecting volume (*hybrid* detectors). Detectors integrating in the same silicon die the sensing volume and the readout electronics are known as *monolithic*. In the following sections, technologies of particular relevance for this thesis will be presented.

3.3.1 Silicon strip detectors

Silicon detectors are usually fabricated by growing or implanting one type of doped silicon on top of another. By segmenting the implant in many parallel strips, reconstruction of the position of the traversing particle in one dimension can be achieved. These strips can be metallized (DC coupled) and act as charge collecting electrodes. The signal is read out by connecting each strip to a charge sensitive amplifier: the signal can then be shaped and digitized. The position of the crossing particle is reconstructed from the signals induced on a single or a few of the individual strips. A typical n-type silicon strip detector is built out of a p^+-n junction, with a thickness of 300 μm and a n^+ layer on the backplane to improve the *ohmic* contact with the aluminium metallization. The operating voltage is typically < 200 V. All the strips are connected to the so-called bias ring, which provides the bias necessary to deplete the detector. A long poly-silicon resistor in the order of $\sim$ MΩ is coupled between each strip and the bias ring to prevent the signal generated on the strip from flowing into the ring. To block the DC leakage current from flowing into the readout electronics, an AC coupling of the electrodes can be implemented by depositing a $100-200$ nm thick layer of SiO_2 between the p^+ implant strip and the metallic strip contact. In this way, a capacitor with a capacitance of ~ 100 pF is formed by the SiO_2-metal configuration, where the charge signal on the p^+ implant induces a charge on the electrode which is read out. The sensor is wire bonded to the readout electronics. A schematic overview of the structure of a silicon strip detector is given in fig. 3.5, and a top view of such a detector is given in fig. 3.6.

Two dimensional position resolution can be achieved by adding strips also on the wafer backside (double sided silicon strip technology). If the angle between the strip orientations is 90°, this will result in uniform resolution in both direction. The main disadvantage of this kind of detectors is the ambiguity (so-called ghost-hits) in the reconstruction of the two-dimensional positions when two or more particles cross the sensor at the same time. This issue can be solved by using crossing angles $<90°$, which, on the other hand, will give reduced position resolution in one of the two dimensions. Also, more layers of strip detectors with a different strip orientation can be built, thus adding more material in the detector, but reducing the computational time to eliminate the ghost-hits.

Silicon strip sensor technology allows to integrate the readout on the sides of the sensors, at the end of the strips, thus allowing to have a sensing region with an extremely low material budget and with a low thermal dissipation (in the order of nW/cm^2). Both

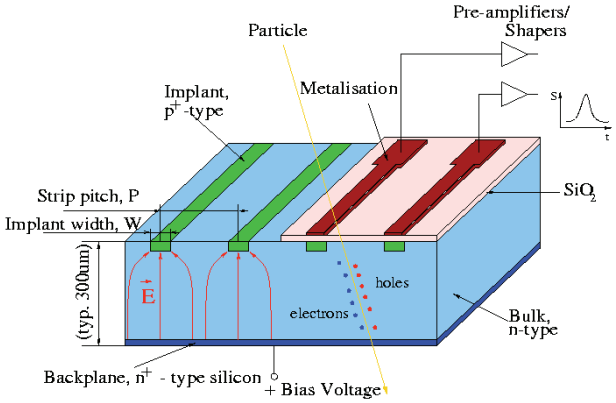

Figure 3.5: Drawing of a cross-sectional view of a silicon strip detector showing the principle of detection of a charged particle [11].

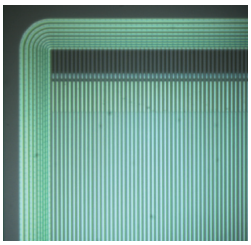

Figure 3.6: Top view of a strip silicon detector. Strips and guard rings are visible, as well as the pads for connecting the readout electronics to the detector.

characteristics will be exploited in the AEgIS silicon position sensor, as will be shown in the next chapters, with the first data on direct detection of antiproton annihilation in a strip sensor.

3.3.2 Silicon pixel detectors

The problem of ghost-hits in high occupancy scenarios can be more effectively eliminated by introducing pixels instead of strips. By dividing the electrodes in small equal square cells, an excellent two dimensional position resolution (down to few µm) can be achieved. The readout in the hybrid pixel detectors is performed by connecting the pixel sensor with the matrix of the front−end readout chip. Both the sensor and the electronics matrix are segmented in exactly the same way, so they can match perfectly when joined into one detector. A cross section of a hybrid pixel detector is given in fig. 3.7. The contact between the sensor and the chip is made with a special technique called bump-bonding. An example for this bond, with a typical pitch is 50 µm, is shown in fig. 3.8.

One of the advantages of pixel detectors is the very low capacitance (in the order of fF), which is mostly influenced by a neighbouring pixel rather than the backside plane. As the capacitance is one of the main contributors to the electronic noise, this results in high signal-to-noise ratio (exceeding 100 [84] for a fully depleted 300 µm thick sensors).

The good position resolution in these detectors is achieved with the centre-of-mass charge weighting which is provided by the charge sharing between different pixels. Some of the main disadvantages of this technology are the large number of channels, the high power consumption and the relatively low yield of the bump-bonding technique, as well as the relatively high fabrication costs related to the separate production of the sensor and the readout chip. For this reason, research and development efforts are directed toward monolithic detectors, where the readout electronics and the active volume are realized in two different layers within the same wafer, thus removing the

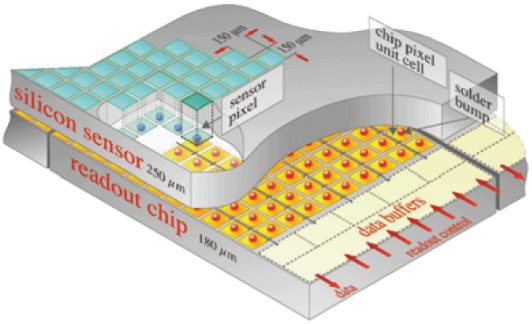

Figure 3.7: Schematic drawing of parts of a hybrid planar pixel detector showing the two different parts: front-end readout chip and the sensor [12].

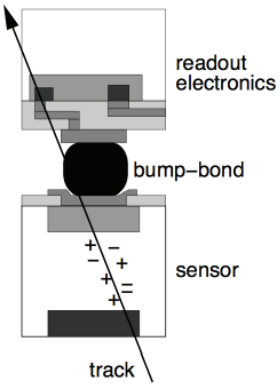

Figure 3.8: Schematic layout of the bump-bond between a single cell (pixel) of the sensor and the readout chip. When particle passes through the sensor and ionizes it, the generated signal is passed to the chip through the bump bond [13].

need for bump-bonding.

3.3.2.1 3D silicon pixel detectors

The 3D technology for silicon pixel detectors is relatively new, originally proposed in 1997 [90]. The main difference with respect to planar pixel detectors is the geometry of the electrodes: while the electrodes in planar sensors are implanted on the surface of the device and the applied bias is used to deplete the full thickness of the bulk (usually $\sim$300 μm), the electrodes of a 3D sensor are implanted inside the sensitive volume, in form of columns perpendicular to the surface (see fig. 3.9).

This kind of detector architecture offers several advantages over other pixel sensor technologies. Unlike the planar sensors, where the electric field created from the reverse bias grows perpendicularly to the surface, in 3D devices this field develops in lateral direction. Hence, the full depletion voltage does not depend on the overall thickness of detector, but only on the distance between two electrodes, which can be as small as 50 μm. This feature provides a higher electric field at lower depletion voltage ($\sim$ 10 V, compared to 30-100 V for planar sensors) [91]. The generated carriers travel on a shorter collection path on the way to the electrodes, which increases the signal strength due to the decrease of the recombination of carriers. Furthermore, the charge collection time is much shorter ($\sim$ ns, compared to the planar detectors (tens of ns) [91]. This results in a higher signal-to-noise ratio, despite the increasing noise (because of the short distance, capacitance values are higher than for planar sensors). Hence, one of the main advantages of 3D detectors is the large pulse with a fast rise-

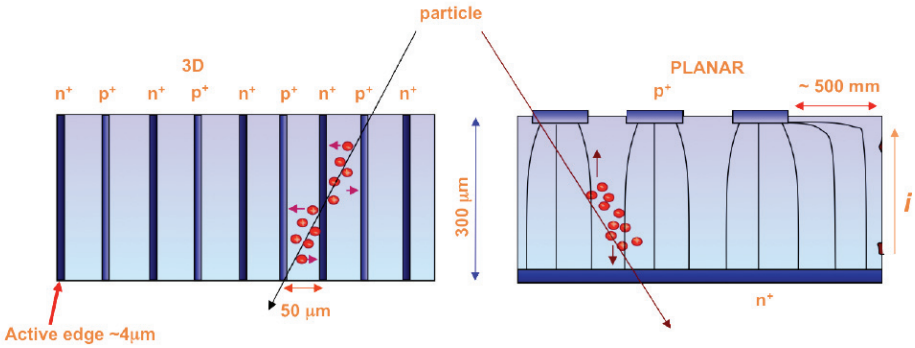

Figure 3.9: Difference between the geometry of a 3D sensor (left) and a planar one (right). In 3D detectors charge carriers drift in lateral direction, whereas in planar detectors they move across the whole volume of the bulk, thus passing a greater distance [14].

time. Another benefit of the 3D electrode architecture is that the sensor edge can be an electrode, which can reduce the dead area down to few microns [92, 93]. This is due to the absence of guard rings, otherwise needed to smoothly lower the voltage, which results in a large inactive region at the edge of the detector.

The edge electrodes are fabricated in the same way as the others, by etching a trench into the silicon wafer which is then doped. Another feature that favours the 3D detectors over planar detectors is the lower charge sharing which is due to the specific electrode's configuration that creates a large shielding effect [94]. Nevertheless, the electrodes themselves are inactive and do not produce charge, so the detector is inefficient in these areas. If a particle happens to cross exactly through the electrode column, it won't be detected. However, the efficiency is fully recovered at 15° with respect to the direction of the electrode. The 3D detector technology is still not produced on large scale because of the non standard manufacturing (Deep Reactive Ion Etching -DRIE- technique [95]) and there is an ongoing effort for its industrialization. The first application of this detector technology is the installation of 3D detectors in the Insertable B-Layer of the ATLAS detector at CERN in spring 2014 [91].

3.3.2.2 Monolithic active pixels (MAPS) detectors

The idea and the first successful development of a monolithic detector, where the active sensor volume and the electronics are integrated in the same silicon wafer was made in the beginning of the 1990s [96]. The early developed monolithic pixel detectors consisted of a PIN diode, with a junction created between the fully depleted p-type bulk and n-type diffusion layer. The readout electrodes were of p^+-type and were placed in a region of minimal electric field, as the diode junction was formed on the back side.

The readout circuit consisted of PMOS (P-type metal-oxide-semiconductor) transistors connected to each of the pixel cell. The n-well field, created by the n-type diffusion layer, extending into $\sim$ 90 % of the sensor area allowed for holes created by ionizing radiation in the depletion layer to be collected by the collection electrodes [97]. The operating principle of the first MAPS detectors is shown in fig. 3.10. Even though the

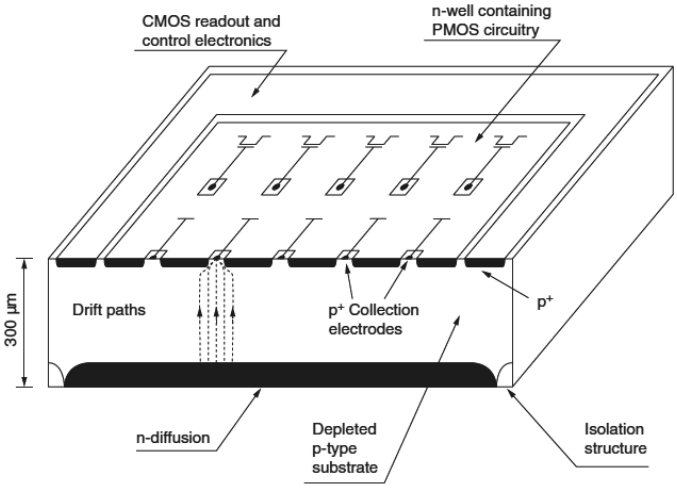

Figure 3.10: Cross-section of the first generation of monolithic pixel detectors [15].

performance of this type of detectors was impressive at the early stage of pixel developments, the use of non-standard technologies for their production was the main issue that prevented a large-scale fabrication. However, one of their successors, the CMOS (Complementary Metal-Oxide Semiconductor) detectors, achieved greater success both with the implementation as well as the mass production.

The CMOS detectors are MAPS detectors consisting of an epitaxial layer which serves as a solid state ionization volume with standard NMOS (N-type metal-oxide-semiconductor logic) electronics on top. The main difference with respect to the first monolithic detectors and to other solid state detectors where the active volume is fully depleted, is that these sensors operate without any depletion voltage, so no external electric field is applied to the active volume. Hence, only a shallow depletion layer created by the p-n junction built-in potential is present. The charges created in the epitaxial layer (usually 15-20 µm thick) remain in it because of the reflection from potential barriers at the boundaries due to the difference in the doping levels of the p-epitaxial layer and of the p^{++} wells and substrate. The free charge carriers move in thermal diffusion and when reaching the boundaries, they are collected in the n-well/p-epi diode. The full collection of the charge is obtained through the n-well collection diode because the MAPS is depleted only directly under this diode, so the charge collection is incomplete in all other parts of the epitaxial layer. An illustration of the process is given in fig. 3.11. Given the number of e-h pairs (80) produced per µm by a MIP and the typical thickness of these detectors, the produced signal charge is very small (the total collected charge is about $\sim 1000\ e^-$) and the time needed for the signal formation is quite long ($\sim$ 100 ns) compared to hybrid pixel detectors [97]. Despite the small signal, the values of the signal-to-noise ratio for CMOS detectors can be as high as ~ 30, due to the low capacitance and hence the low noise [83]. The readout rate of CMOS detectors can be very large and frequencies up to $\sim$ 40 MHz can be achieved for devices with several million pixels.

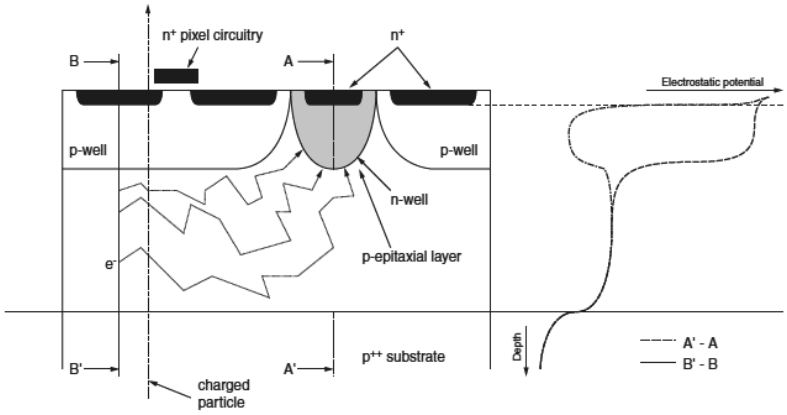

Figure 3.11: Cross-sectional view of one pixel of CMOS detector with n-well/p-epi collecting diode. On the right, the electrostatic potential is depicted [16].

CMOS pixels are widely used for detection of visible light. However, they are more and more used also as ionizing particle detectors. These detectors are competitive because of the standard processing technologies used for their fabrication which result in low cost production. Another advantage is that signal processing circuits are integrated on the sensor substrate (*system-on-chip*) so that the interconnecting procedures used for the hybrid detectors are omitted. Depending on the pixel pitch that is implemented (20-30 μm), a position resolution of few μm can be achieved. Because of the small charge created in the thin active volume, monolithic sensors are quite resilient to saturation effect and can thus be exploited in high luminosity beam monitoring applications [98]. Long collection times negatively affect the performance of MAPS detector in high-radiation applications, where the carrier lifetime is compromised by the radiation-induced bulk damage [99].

3.4 A brief review of the detection of antimatter in silicon

Detection of charged antimatter particles with silicon detectors have been performed in various experiments over the past years. In almost all of these measurements, silicon detectors were used to detect the charged end products of the annihilation of the antiparticles, which occurred in another target material. This is a so-called *indirect* detection. In this way also neutral antimatter atoms, such as antihydrogen have been detected. The final annihilation products are detected in a series of segmented silicon detectors (a telescope) and the position of the annihilation point is then reconstructed with fitting algorithms applied on the tracks measured in these detectors. A new approach (*direct detection*) is being implemented for the AE$\bar{g}$IS silicon position detector, where the antihydrogen annihilation will be detected directly in the sensor. A brief review of the detection of antimatter with silicon detectors is presented in this section.

3.4.1 Silicon detectors for detection of end products of an annihilation

The principle of indirect detection of antihydrogen annihilations was adopted in the ATHENA experiment [100]. The so-called annihilation detector consisted of two layers of 16 double-sided silicon microstrip modules, arranged in a cylindrical shape around the trap where the antihydrogen production took place. The silicon modules were surrounded by a layer of CsI crystals to detect the γ rays from the positron annihilation. The detector covered $\sim 80\%$ of the solid angle and the antihydrogen was detected by measuring the charged hadron tracks coming from the annihilation of the antiproton that coincide in time and space with the two 511 keV photons emitted from the e^-e^+ annihilation. A sketch of the antihydrogen detector is given in fig. 3.12. The inner and the outer diameter measured 75 mm and 140 mm respectively, while the overall length was 250 mm. The detector was able to operate at 80 K, in a relatively high magnetic field (4 T) and in vacuum (10^{-7} mbar). The silicon microstrip modules were composed of two double-sided sensors, 81.6×19 mm^2 each, with a thickness of 380 μm. The sensors were glued on a 400 μm silicon support [17]. The p-side of the sensor was segmented into 384 strips with 46.5 μm pitch and 32 μm implant width. Of these, only 128 strips were read out, as every third strip was bonded to the VLSI (Very-Large-Scale Integration) VA2 TA ASIC (produced by IDE AS, Norway [101]), while the two intermediate were floating. A scheme of the silicon microstrip module is given in fig. 3.13.

The readout system was divided into three independent subgroups: 16 ceramic hybrids for each of the inner and outer layer of the silicon strips and 16 PCBs (Printed Circuit Board) of the crystals were connected in parallel with kapton cables with 33 lines to three printed circuit boards. Up to this point, the described electronics was kept in the vacuum. On the other side of the flange, outside the vacuum vessel, three repeater digital cards that contained the electronics for controlling the three sub-detectors were placed. These cards were connected by two digital buses to VME modules. The readout and the ADC sampling were controlled with a sequencer (CAEN V551B).

First cold antihydrogen atoms were successfully detected with this detector. The detection of the charged products from the antihydrogen annihilation in the two layers of the silicon microstrip detectors allowed three-dimensional reconstruction of the antiproton annihilation vertex with a spatial resolution of 4 mm. Even though the position resolution that was achieved with the silicon strip modules was 28 μm, the overall vertex resolution was much worse because of the unknown curvature of the charged particle tracks in the 3T magnetic field. In fact, the tracks were extrapolated as straight lines from the two measured points (one in each layer of the silicon microstrip modules), as the lack of information on the charge of the pion prevented the determination the track curvature.

A similar annihilation vertex detector, composed of three concentric cylindrical layers of 60 silicon microstrip modules was used for detection of antihydrogen in the ALPHA experiment [19]. This detector operated in dry air atmospheric pressure and was surrounded by a solenoidal magnet that provided a magnetic field of 1 T. The main difference in the construction with respect to the ATHENA detector, previously described, was the absence of CsI crystals and the number of tiers (three, instead of ATHENA's two). The silicon modules had an active area of 6×23 cm with a thickness of 300 μm. Each of them consisted of 256 DC coupled readout strips on the p-side, with a pitch of 227 μm in the $R-\phi$ direction and another 256 AC coupled readout strips on the n-side

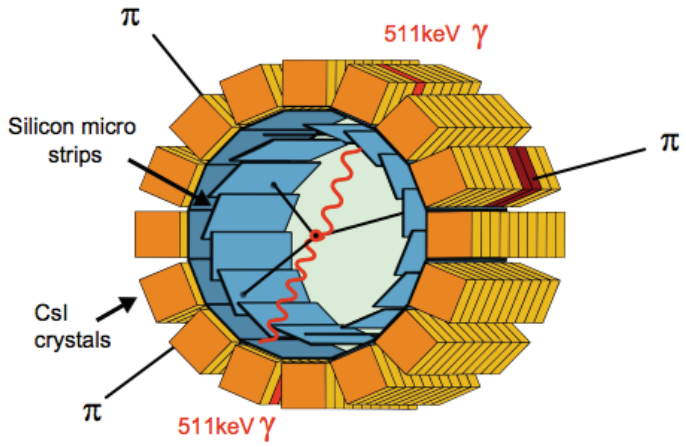

Figure 3.12: Scheme of the ATHENA antihydrogen detector. After the antihydrogen annihilation on the walls of the trap, the charged pions from the antiproton annihilation were detected in the two layers of the silicon strip modules, while the 511 keV γ rays were detected by the CsI crystals [17].

with a pitch of 875 μm in the z direction, R, ϕ and z being the cylindrical coordinates. In accordance with the strip pitch, the achieved position resolution was $227\sqrt{12} = 65$ μm in the $R-\phi$ direction and $875\sqrt{12} = 253$ μm in the z direction. The inner and outer radii of the detector were 75 mm and 114 mm respectively, while its length was 460 mm. This geometry provided a coverage of $\sim 90\%$ of the solid angle. A drawing of the cross section of the detector is given in fig. 3.14.

The readout was performed with VA1 TA ASICs produced by IDE AS, Norway. Each ASIC had 128 input channels and was self triggered, producing a fast 75 ns trigger pulse and slow analogue signal, with a typical shaping time of 1 ms [18]. These analogue signals were then digitized by five 48-channel VME-based VF48 ADC modules. The trigger mechanism was set to read out the entire detector when two or more strips in the $R-\phi$ plane from the inner layer of the detector are hit.

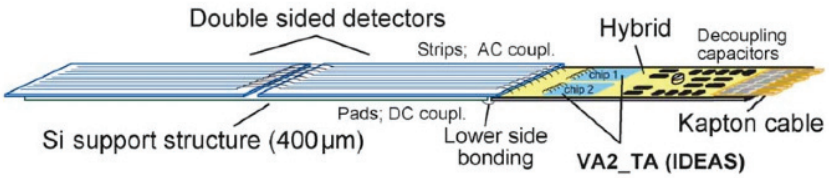

Figure 3.13: Schematic view of the ATHENA modules for the silicon microstrip detector [17].

The reconstruction of each of the annihilation event was made with 9-15 hits that the annihilation prongs produce when travelling through the detector. A *hit* is considered

to be the point where the particle passes through the silicon module and produces a signal in the readout strips on both p and n side of the wafer, which are orthogonal. Given the three layers of silicon strip modules, a track was extrapolated from three simultaneous hits. Due to the large amount of material present between the wall of the trap, where the antihydrogen annihilation took place, and the silicon detector, most of the tracks originated from charged pions. The magnetic field of the Penning-Malmberg trap defined the helical geometry of the trajectories. The shape was confirmed both in simulations and data from measurements. The reconstruction of vertices was performed with at least two intercepting tracks. The overall spatial resolution on the vertex was characterized with the axial, radial and the azimuthal resolutions. The achieved values were 0.56 cm, 0.87 cm and 0.83 cm respectively [19]. A scheme of the ALPHA silicon detector with a reconstructed vertex is given in fig. 3.15.

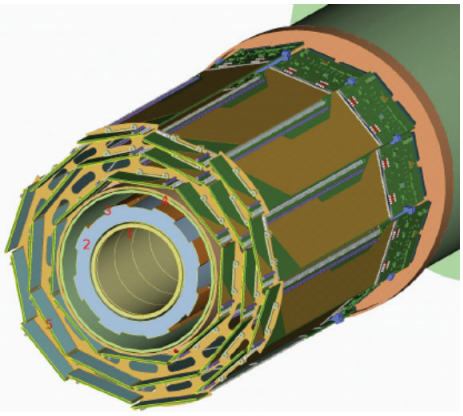

Figure 3.14: Scheme of the cross section of the ALPHA silicon detector. The modules arranged in three cylindrical concentric layers. 1) denotes the trap electrodes, 2) is the supporting structures, Octupole magnet is marked with 3), the beam pipe is 4) and 5) are the hybrids [18].

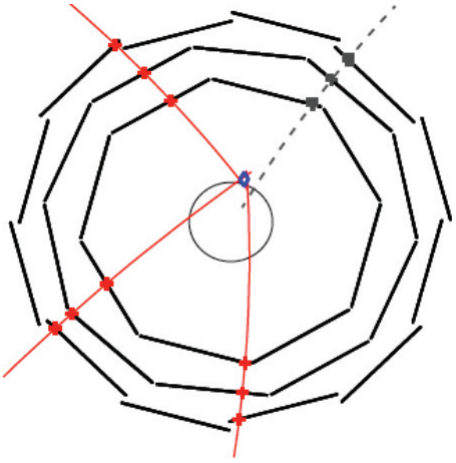

Figure 3.15: Reconstructed annihilation event in the ALPHA silicon detector. Hits in the silicon sensors are marked with crosses, while reconstructed tracks are given with solid lines. The dashed line is a track that was reconstructed but rejected in the process of the vertex reconstruction. The annihilation point (vertex) is marked with blue diamond [19].

3.4.2 Silicon detectors for beam monitoring

Silicon detectors have been used for monitoring beams applications where an information on the beam parameters, like the beam intensity, beam profile and beam position is needed. In such cases, a huge number of antimatter particles passes through the detector (or in some cases is annihilated in it, depending on its thickness) and individual particles are not of interest, but rather the total energy deposited inside the active volume. The characteristics of the beam, such as the number of particles per bunch, can

be obtained from the measured energy. Silicon detectors are suitable for these purposes also because they can easily be operated in the conditions needed for manipulation of antiparticle beams - vacuum and/or cryogenic temperatures. The thickness chosen for the silicon bulk depends on the energy of the incoming particles and the desired method of beam profiling: destructive (when all the particles annihilate in the detector) or non-destructive (when the antimatter particles can pass through the detector and are further used in the experiment).

An example for a silicon monitoring detector is the thin sensor (67 μm) that was placed in the ATHENA apparatus for beam diagnostics [102]. This so-called beam counter was a circular PIN diode (15 mm diameter) where the p^+ implant is segmented in five pads in order to determine precisely the position and the intensity of the incoming antiproton beam (5.3 MeV). The signal was fast enough to provide a trigger for the catching trap of the ATHENA experiment. It operated in a magnetic field of 3 T and 10 K temperature. A photograph of the device is shown in fig. 3.16. The energy loss of 5.3 MeV antiprotons in silicon was estimated to be of 11.4 keV/μm, which, for $\sim 10^7$ incoming antiprotons gives $\sim 3.2 \times 10^{10}$ electron-hole pairs per μm silicon [102]. This huge number of generated carriers provided a signal large enough to be read out directly, without any amplifier. In this way, the output signal was taken directly to the 50 Ω input of the oscilloscope and the total charge was obtained by integration of the data from the oscilloscope. A similar beam counter with different thickness (55 μm) was installed in the AEḡIS experiment in 2012. The author of this work was the responsible person for the commissioning and the operation of the AEḡIS beam counter.

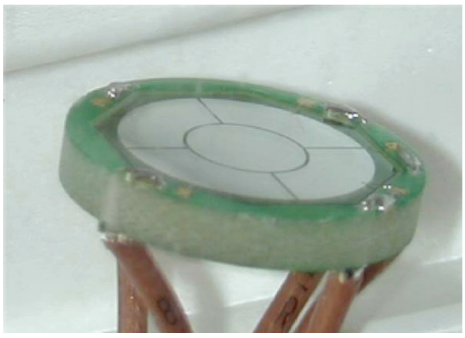

Figure 3.16: A photo of the ATHENA beam counter. The silicon detector was segmented in five pads and mounted on a circular PCB frame. The readout was made with an oscilloscope [17].

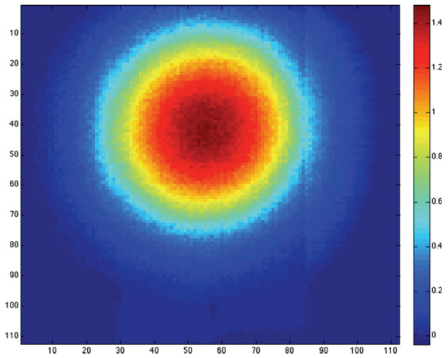

Figure 3.17: Beam profile of a single shot containing $\sim 3 \times 10^7$ antiprotons delivered in 500 ns, captured in a single frame of the MIMOTERA detector [20].

Another application of an antiparticle beam profilometer which is based on a thin silicon detector has been exploited in the ACE (Antiproton Cell Experiment) experiment at CERN. A monolithic active pixel detector (MAPS) was used to obtain the exact characteristics of the antiproton beam before it irradiates the cells [20]. The measurement of the beam parameters in this experiment was of high importance because it was used as an input for calculating the dose delivered to the sample. The detector had

to cope with the large number of antiprotons (3×10^7) delivered within 500 ns, and an extremely high dynamic range was required to avoid possible saturation. The detector had to provide a fast output from spill to spill so that the beam can be monitored and the parameters can be adjusted accordingly in real time. The measured beam profile of one spill is given in fig. 3.17. The same detector was used as part of the experimental work in this thesis for studying individual antiproton annihilations in segmented silicon for the first time. The MAPS detector, due to the high dynamic range, was suitable for analysis of the total energy deposited in the detector due to an annihilation event.

3.4.3 Silicon detectors for direct annihilation detection

To our knowledge only one experiment has been performed which measured directly the annihilation of antiprotons with a silicon detector. However, this was a non-segmented silicon detector and was looking at antiproton energies higher than what was studied for this thesis. In this measurement the goal was to measure the depth of the nucelar density radius at which the antiproton annihilations usually occur. The incoming antiprotons of 608 MeV/c annihilated in the silicon detector that was used to measure the energy released from an annihilation event, whereas a magnetic spectrometer system (called CALLIOPE [103]) that included $x-y$ position sensitive gas counters, plastic scintillators and Cherenkov counter was used for tracking and identification of the annihilation prongs. The signal observed in the silicon detector due to an annihilation event is caused by the energy deposited in its bulk from the energy losses of various successive processes:

- The penetration of the incoming antiproton in the detector bulk up to the point of the annihilation.
- The primary charged particles produced during the direct intranuclear cascade (p, $\pi^{\pm}$ and $K^{\pm}$) until they exit the silicon detector.
- The charged particles produced during the subsequent de-excitation cascade and evaporation, including p, d, t, ^{3}He, α and the recoiling residual nucleus.

The deposited energy was afterwards used, through Monte Carlo modelling, to determine the radius (depth) of the silicon nucleus where the incoming antiproton annihilated [104].

Chapter 4

The AEgIS experiment

This section gives a detailed description of the AEgIS experiment and explains every step towards the formation of the antihydrogen beam and the gravity measurement. Different parts of the AEgIS apparatus and their operation are presented in sec. 4.3, based mainly on [31] and [105]. The design constraints and requirements for the silicon detector that emerge from the concept of the gravity measurement and the integration of the detector within the overall AEgIS apparatus are given in sec. 4.3.4.1.

4.1 Antimatter and gravity

One of the questions that arise from the nature's apparent preference for matter over antimatter is the gravitational interaction between the two. The lack of direct observation, independent from theoretical models, resulted in the development of different theories, some even claiming that antigravity is possible, or at least allowing that antimatter might fall differently from normal matter in the Earth's gravitational field [106, 107]. According to the classical, Newtonian theory of gravitation, the acceleration, g, of a body in the Earth's gravitational field is given by

$$m_I g = G\frac{m_G M_E}{r^2}, \tag{4.1}$$

where m_I and m_G are the inertial and the gravitational mass of the body, M_E is the Earth's mass, r is the distance between the two masses and G is Newton's constant. Measurements have shown that bodies fall with the same acceleration in a given gravitational field, regardless of their composition and structure, which implies the equality between the inertial and gravitational mass. Einstein used this as a postulate in the Theory of General Relativity (GR), and formulated the *Einstein Equivalence Principle* (EEP), which states that a laboratory in a free fall can be considered as being at rest and free of the gravitational field for any local non-gravitational experiment. The *Weak Equivalence Principle* (WEP) is just another version of the EEP which states that the trajectory of a point mass in a gravitational field depends only on its initial position and velocity, and is independent of its composition and structure.

It is thus clear that GR and its equivalence principles imply that a particle and its antiparticle should have the same acceleration in a certain gravitational field. Nevertheless, GR is a classical theory that does not imply the existence of antimatter. Attempts

to unify gravity with other fundamental forces resulted in quantum theories of gravity [108] that predict additional gravitational forces mediated by spin 1 (gravivector) and spin 0 (graviscalar) partners of the well known graviton with spin 2. Depending on the spin of the exchanged bosons, these forces could be attractive or repulsive. For example, the vector component (mediated by the spin 1 gravivector) is repulsive between same charges (matter-matter) and attractive between opposite charges (matter-antimatter) [109, 110].

In matter-matter interactions the effects from the virtual exchange of the vector and the scalar bosons would cancel each other, thus becoming invisible. Phenomenologically speaking, the observable classical effect from the quantum gravity theories can be written as an additional potential of Yukawa type, with approximately gravitational strength, between the two point masses m_1 and m_2, (with the gravivector and the graviscalar taken into account) [111]:

$$V = -\frac{Gm_1m_2}{r}(1 \mp ae^{-r/v} + be^{-r/s}), \tag{4.2}$$

where a and b are the products of the vector and scalar charges, and v and s are the inverse masses of the graviphoton and graviscalar, respectively. The sign in front of a changes accordingly for matter-matter (-) and matter-antimatter (+) interactions. Depending on the values for a and b, different conclusions can be drawn for the gravitational behaviour of antimatter. Assuming that the values of these parameters are $a \sim b \sim 1$, an antimatter body would experience attractive graviscalar and gravivector interactions in the gravitational field of Earth, which would lead to antimatter falling with an acceleration greater than g and thus a violation of the WEP. Nevertheless, there are no constraints to the range of values for a and b within the quantum gravity theories.

Another theoretical approach to the question of gravitational interaction between matter and antimatter has been proposed by Villata [106], in which he starts from the CPT theorem, assuming its invariance also in curved space-time, and combining it with GR. He also assumes that inertial and gravitational masses for matter and antimatter are positive definite. When transforming matter into antimatter by the three operators (charge conjugation, parity and time reversal), the result predicts that matter and antimatter are mutually repulsive. By claiming antigravity and consequently, the separation of the equal amounts of matter and antimatter in the Universe, this result can possibly explain the cosmic expansion and its acceleration. The model goes even further, speculating that antimatter could be located in the so-called local voids (large-scale voids observed in the distribution of galaxy clusters and super-clusters). This would imply that "mysterious ingredients" such as Dark Energy and Dark Matter are no longer needed in the cosmological model for explaining the universe [112].

Other, even more "exotic" cosmological models, such as the Dirac-Milne Universe [113], are in favour of antigravity and a matter-antimatter symmetric universe, in which antimatter has a negative active gravitational mass. This model relies on the hypothesis that particles and antiparticles behave similarly to quasi particles, like electrons and holes in a semiconductor, and that the universe is not subject to accelerated expansion, but rather to a linear evolution of its scale factor. As such, it offers reasonable agreement to the expansion of universe and primordial nucleosynthesis and solves, in an elegant way, the problems of the horizon and the age of the universe.

In conclusion, a direct measurement of the gravitational properties of antimatter would clearly test the various theoretical possibilities. Attempts were made in the past to measure the gravitational acceleration for antimatter using antiprotons, but no conclusive results have been obtained due to the order of magnitude difference in the strength between gravity and electromagnetic force as experienced by antiprotons [114]. This is one of the main issue in gravitational experiments with charged particles, as the electric field has a great influence on the particles, making it very difficult to reduce the effect of electric stray fields to a level below the effect of gravity (e.g. an electric field of only $6 \cdot 10^{-11}$ V/m accelerates a positron equal to gravity). Witteborn and Fairbanks set out to study gravity on electrons [115] (they also made a proposal for positrons but it was never performed [116]) and found the effective force to be zero g - explained by the fact that all stray electric fields were shielded out and the only remaining force aside from gravity was the electric field produced by the sagging of the free electrons in the shield tube to the point where an electric field equal and opposite to the gravitational field was generated inside the tube. Nevertheless, the missing proof is an experiment on positrons where they then expected to measure $2g$.

The most recent experimental result related to this question came from the ALPHA collaboration, which managed to set very broad limits on the ratio of the gravitational and inertial mass of antihydrogen [117], excluding the possibility that the gravitational mass of antihydrogen is more than 110 times its inertial mass, or that it falls upwards with a gravitational mass more than 65 times its inertial mass.

Measuring the local gravitational acceleration of antimatter, $\bar{g}$, in the gravitational field of the Earth is what AE$\bar{g}$IS [31] aims for. The AE$\bar{g}$IS collaboration will attempt to carry out the first direct measurement of the Earth's gravitational acceleration for antimatter with 1% relative precision, using the simplest form of electrically neutral antimatter: antihydrogen.

4.2 The Antiproton Decelerator (AD)

The two main ingredients needed to create antihydrogen atoms are antiprotons and positrons. At CERN, all the antimatter experiments make use of the low energy (5.3 MeV) antiproton beam extracted from the AD. This unique facility with a circle-like shape and a circumference of $\sim$ 188 m is the only one in the world able to produce such a beam. The production includes several stages and starts with the acceleration of protons up to 50 MeV in the Linear Acelerator 2 (LINAC2). The protons are then transferred into the Proton Synchrotron (PS) Booster, where they are accelerated to an energy of 1.4 GeV, and injected into the Proton Synchrotron which increases their energy up to 26 GeV. At this point, about $\sim 1.5 \times 10^{13}$ protons hit a metal target (copper or iridium) and different matter-antimatter particle pairs are created. The proton-antiproton pair production occurs according to the following reaction:

$$\mathrm{p}(beam) + \mathrm{p}(target) = \mathrm{p} + \mathrm{p} + \mathrm{p} + \bar{\mathrm{p}}. \tag{4.3}$$

The efficiency for proton-antiproton pair production is very small, only 10^{-4} $\bar{\mathrm{p}}$/p, which, combined with the collection efficiency for antiprotons produced in the target

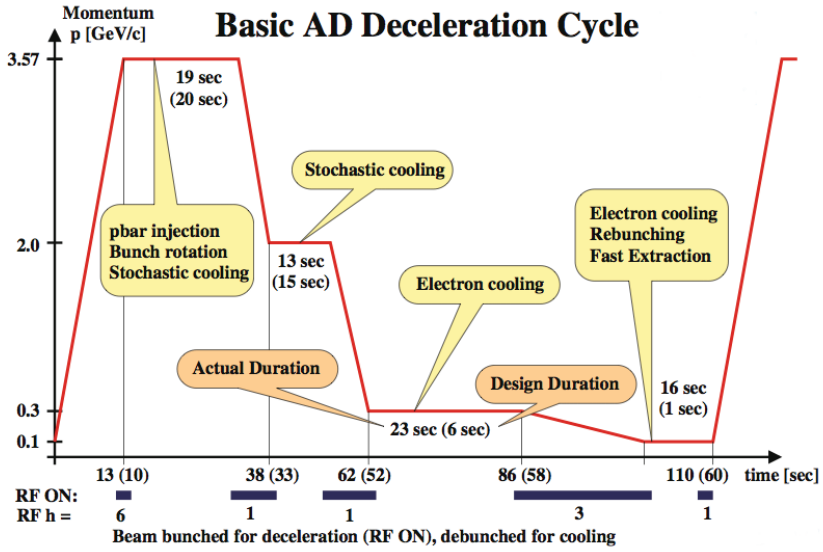

Figure 4.1: A schematic overview of a typical AD cycle showing the decrease of the momentum of the antiprotons as function of the time necessary to perform each step. The beam is bunched for deceleration (RF ON) and debunched for cooling [21].

(10^{-2}), gives $\sim 5 \times 10^7$ antiprotons extracted from one production cycle. The energy of the outcoming antiprotons is $\sim$3.6 GeV and must be reduced by eight orders of magnitude before they can be of use for antihydrogen production in the experiments [22]. Therefore, antiprotons are directed towards the AD to be decelerated using RF cavities and cooled in different stages. The antiproton beam is injected into the AD with an emittance of 190 πmm.mrad, while the spread of the momentum is $\pm 3\%$. This quite large dispersion of the beam is reduced down to $\pm 0.75\%$ by bunch rotation, which is the first step of the AD cycle, followed by two subsequent stages of stochastic cooling, separated by RF deceleration from 3.5 GeV/c to 2 GeV/c. Antiprotons are then further decelerated down to an intermediate momentum of 300 MeV/c) and cooled down by means of electron cooling, which is more suitable for lower energy beams. They are finally slowed down to a momentum of 100 MeV/c and electron-cooled to obtain a final emittance of 0.3 πmm.mrad and momentum spread of 0.01% [22]. In this way, at the end of the 100 s cycle, a 5.3 MeV antiproton pulsed (100$-$200 ns long) beam in bunches of $\sim 3 \times 10^7$ $\bar{\text{p}}$ is ejected from the AD and delivered to the experiments. A scheme of the AD cycle is given in fig. 4.1 and a schematic overview of the AD machine and the position of the beam lines of the experiments is shown in fig. 4.2.

The energy of the antiprotons provided by the AD is still too large for them to be directly trapped in the experimental apparatuses. For this reason, different degrader foils are used to further slow down the antiprotons to energies suitable for trapping, which are in the order of few keV. As a consequence, a great amount ($\sim$ 50%) of the incoming particles is lost, as they annihilate in these degraders. These losses will be significantly reduced with the upgrade of the AD, ELENA (Extra Low ENergy An-

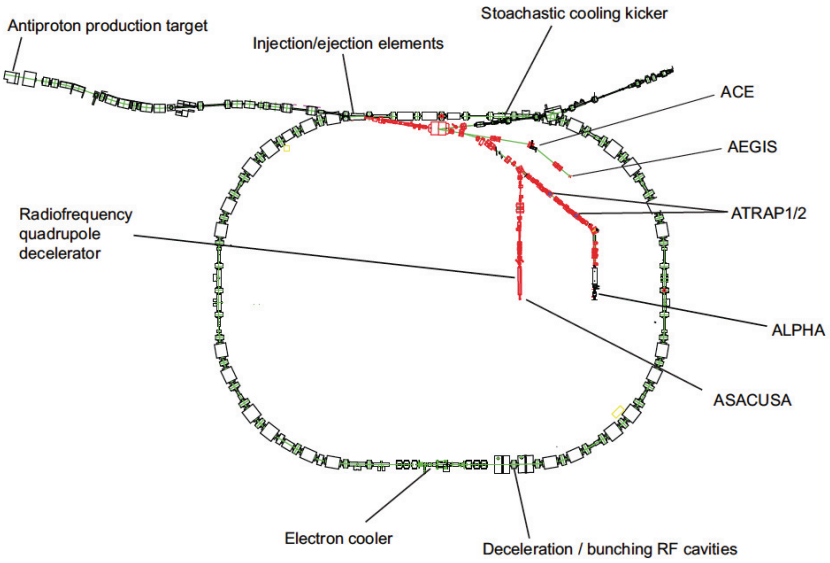

Figure 4.2: A schematic overview of the AD at CERN including the position of the beam lines for the different antimatter experiments in 2012 [22].

tiprotons) [21, 118], which is currently under construction. According to the design specifications, this small ring inside the AD (with a circumference of 30.4 m) will be able to provide a pulsed (300 ns) beam in bunches of $\sim 6 \times 10^6$ antiprotons with a kinetic energy of ~ 100 keV.

4.3 The AEḡIS experiment

The AEḡIS experiment at CERN is designed and built to measure the local gravitational acceleration for the simplest antimatter atom in Earth's field with 1% relative precision. This goal will be reached by measuring the vertical shift of an antihydrogen beam after traversing ~ 1 m path in horizontal direction. The cold (~ 100 mK) antihydrogen atoms will be produced by a charge exchange reaction between laser excited (Rydberg state) positronium (Ps) atoms and cold antiprotons. The beam will be formed by applying an inhomogeneous electric field (Stark effect) to accelerate the hydrogen Rydberg atoms to few hundred m/s (see fig. 4.3). After the acceleration, the beam will propagate through the two gratings of a moiré deflectometer [119], where a selection of certain paths will occur. Atoms should decay towards their ground state during the time they need to reach the detector. In the end, the pattern produced by the moiré deflectometer will be detected and observed with a position sensitive detector. Over a horizontal path of ~ 1 m, the shift due to gravity is expected to be in the order of ~ 20 µm.

A schematic overview of the AEḡIS apparatus with its different parts is given in fig. 4.4. The two largest components are the 5 T and 1 T superconducting magnets which are enclosed in liquid helium vessels and connected through the central re-

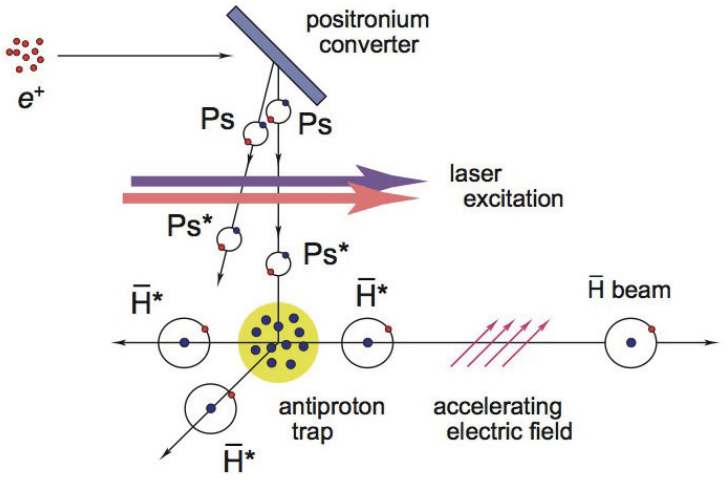

Figure 4.3: Schematic overview of the antihydrogen production in AEgIS. The positronium is excited in two subsequent steps to Rydberg states and combined with the cold antiprotons to create antigydrogen. The atoms are then accelerated by an inhomogeneous electric field to produce a beam.

gion. In addition, thermal shielding is provided by the liquid nitrogen containers that surround the liquid helium vessels. The 5 T magnet houses the ultra high vacuum ($\sim 10^{-12}$ mbar) region where the antiproton catching and cooling trap and the positron storage trap are placed. The second magnet, with 1 T magnitude, encloses the antihydrogen formation region. The detection of antihydrogen and the gravity measurement will take place in the gravity module, a tube housing the moiré deflectometer and the position detector, attached at the end of the 1 T magnet.

4.3.1 Positronium formation and excitation

As mentioned already, the antihydrogen production in AEgIS will occur through the following charge exchange reaction between the highly excited positronium and cold antiprotons:

$$\mathrm{Ps}^* + \bar{\mathrm{p}} \rightarrow \bar{\mathrm{H}}^* + \mathrm{e}^- . \tag{4.4}$$

Positronium is a neutral bound system consisting of an electron and a positron that can coexist together for a very short time (up to $\sim$ 100 ns) before they annihilate. The positronium production in AEgIS begins with $\sim 10^8$ positrons, supplied from a ^{22}Na β^+ source and stored in a Surko-type accumulator [120] for $\sim$ 300 s. The stored positrons are cooled down through collisions with a nitrogen buffer gas and then transferred through their own transfer line to the e^+ dedicated catching trap in the 5 T magnet. The transfer line between the accumulator and the 5 T magnet includes solenoids

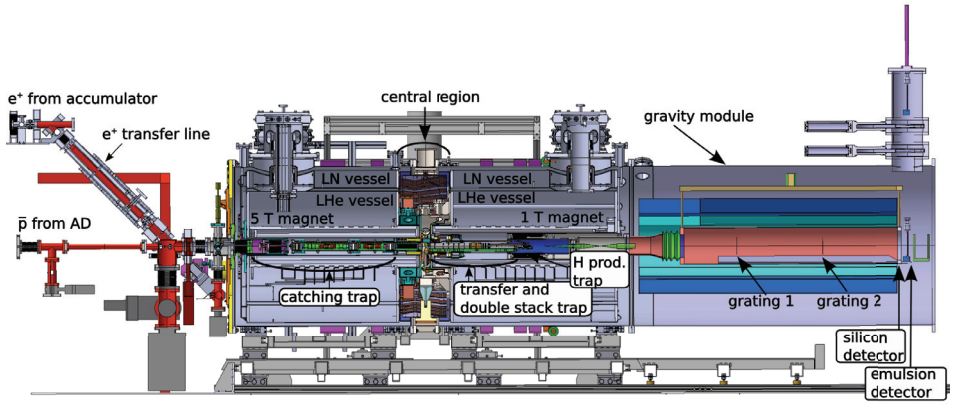

Figure 4.4: A schematic cross-sectional view of the AEgIS apparatus at CERN, showing its different parts. Positrons from the accumulator (not shown) are transferred to the 5 T magnet with their own transfer line. 5 T and 1 T magnet are connected through the central region and house the catching traps, the transfer traps and the antihydrogen production ultra cold trap. The gravity module is attached downstream the 1 T magnet and encloses the moiré deflectometer and the hybrid position detector.

that create magnetic field lines along which the slow positrons move and arrive into the traps inside the magnet. A large number of positrons confined in a Malmberg-Penning trap can form a plasma (see sec. 4.3.2.1), which then can be compressed applying a rotating wall technique [121]. This technique allows the reduction of the radial extension of the positron cloud (i.e. compression) by using an appropriate electric field that exerts a torque on the cloud, thus changing its shape. The time varying electric field is applied to the plasma through a segmented electrode, split azimuthally into four sectors. The benefit of the radial compression of the positron plasma is an increase of the storage time and the number of accumulated positrons. The mechanism is explained in detail in sec. 4.3.2.2.

In the 1 T magnet, the traps for the antiprotons and the positrons become separated by a double stack configuration (see fig. 4.5), necessary for the next steps: antiproton compression and transfer in the on-axis trap and positrons acceleration towards a positronium conversion target in the off-axis trap. The Ps converter [122] is a target of nano-porous material located at the end of the off-axis trap. Once injected into the converter, the positrons bounce from the walls of the nano channels in the target and some of them form positronium by binding with an electron. As the pores are connected to the surface of the material, the positronium can escape towards the vacuum through the pore channels by colliding with the pore walls. Fig. 4.6 shows a drawing of the mechanism of positronium conversion and cooling in porous materials [23]. The emerging positronium can be produced with 1/4 probability into *para*−Ps with spin 0 (singlet) and with 3/4 probability into *ortho*−Ps with spin 1 (triplet), which are the two possible ground states. The mean lifetime of *para*−Ps is too short (only 125 ps) and it is not possible to laser excite it before it decays into two γ of 511 keV each. On the other

hand, the mean lifetime of *ortho*−Ps is 142 ns, which is long enough to be laser excited before it self-annihilates into three γ of 2×511 keV total energy. Nevertheless, the presence of 1 T magnetic field, where the antihydrogen formation takes place, reduces the lifetime of *ortho*−Ps, as one of the triplet states (with spin component $S_z = 0$) mixes with the singlet state and its lifetime decreases to 15 ns. However, the lifetimes of the two other components do not change, so a total reduction of 1/3 is expected.

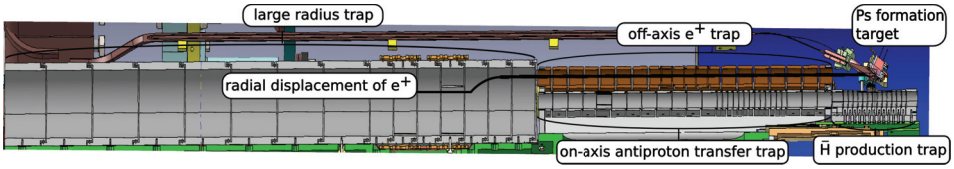

Figure 4.5: Schematic layout of the AEgIS trap system placed in the 1 T magnet. Antiprotons and positrons arrive separated in time from the 5 T region, which is on the left (not visible on the picture). After the rotating wall compression in the large radius common trap, positrons are moved off-axis by diocotron mode excitation and injected in the upper trap of the double-stack. They are then accelerated towards the positronium production target. Antiprotons continue through the on-axis trap, which is devoted to their transport to the antihydrogen production trap.

In AEgIS, the target for the positronium formation is made of a nano-channelled (5-100 nm diameter) Si p-type (crystal orientation 100) material. The energy of the emerging positronium depends strongly on the energy of the incoming positrons. At 1 keV positron implantation energy, the *ortho*−Ps emission into vacuum is estimated to be about 42% [123]. Taking into consideration that the cross section of the charge exchange reaction increases significantly as the Ps velocity decreases [31], the energy of the emerging *ortho*−Ps must be as low as possible. Cryogenic tests performed by members of the AEgIS collaboration showed that when 7 keV positorns are implanted in a target which is kept at 150 K, about 27% of the positrons form positronium that escapes into the vacuum and around 9% of the escaped positronium is cooled by collision with the walls of the nano-channels [124]. The target, which will be mounted in a cryogenic (100 mK) environment, very close to the antiproton trapping region inside the 1 T superconducting magnet, must be able to provide long enough contact for Ps atoms to be cooled down to a temperature of a few tens of K. The produced *ortho*−Ps is expected to emerge with a velocity of $\sim 10^4$ m/s, which corresponds to an energy of ~ 10 meV [31].

The Ps excitation in AEgIS will be performed in two subsequent stages. The large transition energy (> 6 eV) between $n_{Ps} = 1$ and the Rydberg states, does not allow for the transition to be stimulated with a commercially available laser. Therefore, two superimposed laser pulses will be applied to excite the Ps from ground state ($n_{Ps} = 1$) to Rydberg states ($n_{Ps} = 16 - 30$). An UV pulse with λ=205 nm will stimulate the transition from $n_{Ps} = 1$ to $n_{Ps} = 3$, whereas a tunable IR laser that generates radiation pulses in the optical band $\lambda = 1650 - 1700$ nm will be used for the $n_{Ps} = 3 \rightarrow n_{Ps} = 16 - 30$ transition. Excitation to higher levels will increase the ionization probability and will thus be avoided in order to minimize losses due to ionization processes. The level $n_{Ps} = 3$ was chosen as intermediate instead of $n_{Ps} = 2$ mainly because of two reasons:

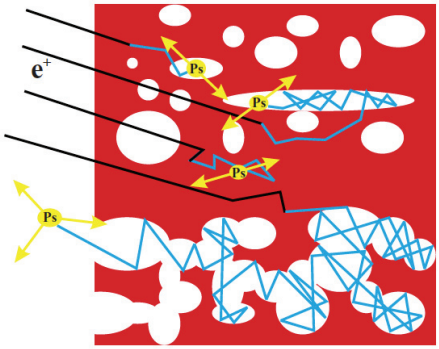

Figure 4.6: Drawing of the mechanism of positronium formation in porous materials [23]. Some of the injected positrons bounce on the walls of the nano channels and capture an electron to form a positronium.

three times longer lifetime (10.5 ns compared to 3 ns) and lower power necessary to reach saturation. Even though the power needed for the 1→2 and 1→3 transitions is similar, the power required for the 2→16-30 transition (up to saturation) is one order of magnitude higher than the power for 3→16-30 [31]. The efficiency of the two-step laser system is expected to be $\sim$ 30% [125].

The Rydberg states of the positronium are essential for manipulating the antihydrogen by using the Stark effect because the principal quantum number of the antihydrogen, $n_{\bar{\mathrm{H}}}$, is determined by the principal quantum number of the positronium involved in its formation, $n_{\bar{\mathrm{H}}} = \sqrt{2} n_{\mathrm{Ps}}$. Rydberg states are as well crucial for the cross section of the charge exchange reaction (eq. 4.4), which scales as $\sigma \propto n_{\mathrm{Ps}}^4$ [126]. Finally, the excitation of positronium is also important for increasing the lifetime of the *ortho*−Ps.

4.3.2 Antiprotons trapping and cooling

Antiprotons coming from the AD ($\sim 3 \times 10^7$ $\bar{\mathrm{p}}$ every $\sim$ 100 s) enter the 5 T magnet through different degrader foils: one fixed (18±2.7 μm) and one movable (0.8±0.2, 2±0.5, 3±0.75, 4±1 and 5 ±1.25 μm), then a silicon beam counter (55±5.5 μm) [102] and another fixed aluminium degrader (150 ±15 μm). Passing through the degraders, they continuously loose their energy, reaching an energy $<$ 700 keV before entering the antiproton catching traps. Here, the antiprotons are first trapped and cooled down by electron cooling, then accumulated and compressed. Similar to the positrons, they are afterwards transferred to the 1 T region through a set of transfer electrodes. The trap system in this region consists of the so-called *large radius trap*, that continues in a double stack trap, where the two different types of particles are injected: antiprotons in the axial trap and positrons into the off-axis trap (fig. 4.5.)

4.3.2.1 Catching traps in the 5 T superconducting magnet

The trap system in AEgIS consists of Penning-Malmberg traps that are placed inside the bores of the 1 T and 5 T magnets, in the cryogenic (4.2 K) ultra-high vacuum. Before explaining the implementation of the traps in AEgIS, the theoretical basis of the confinement principle in Penning-Malmberg trap is given below, based on work presented in [24], [127] and [128].

The Penning-Malmberg trap belongs to a class of particle traps called Penning traps, which make use of superimposed static electric potential and a strong homogeneous axial magnetic field. A quadrupole electric field is produced with three hyperbolic electrodes: one central electrode (ring) and two end caps (top and bottom). Penning-Malmberg traps, used for non-neutral plasma confinement, differ from the ordinary Penning traps by their cylindrical symmetry. They consist of a set of aligned hollow cylindrical electrodes. This geometry offers two main advantages over the Penning traps: the volume inside the trap can be easily accessed and instruments for diagnostics of the trapped particles can be placed at the end of the trap; the use of multiple electrodes instead of one allows to vary the axial electric fields to manipulate the trapped particles and to even simultaneously confine particles with different charges. The following explanation on how particles are confined refers to an ideal Penning trap. Even though the electric potentials used in Penning-Malmberg traps are usually more complicated than the harmonic potential and include an-harmonic contributions, the obtained results can be considered as a first-order approximation of the motion associated to a charged particle in a Penning-Malmberg trap.

The magnetic field used for the particle radial confinement is given by $\mathbf{B} = (0,0,B)$, while the electric field is obtained from the electrostatic potential Φ ($\mathbf{E} = -\bigtriangledown\Phi$), which is given by

$$\Phi(x,y,z) = \frac{V_0}{2d^2}\left(z^2 - \frac{1}{2}x^2 - \frac{1}{2}y^2\right), \tag{4.5}$$

where V_0 is the applied potential and d is the characteristic length of the potential well. The axial confining force for a particle with charge q is the z-component of $\mathbf{F} = q\mathbf{E} + \mathbf{V} \times \mathbf{B}$, and since the velocity $\mathbf{v}$ of the axial motion of the particle is parallel to the magnetic field $\mathbf{B}$, the z component is given by

$$F_z = -q \bigtriangledown \Phi = \frac{qV_0}{d^2} z. \tag{4.6}$$

According to this, the motion of the particle in z direction is harmonic and is given by the equation

$$\begin{aligned} F_z = m\frac{d^2z}{dt^2} &= -m\frac{qV_0}{d^2}z, \\ \frac{d^2z}{dt^2} + {\omega_z}^2 &= 0 \end{aligned} \tag{4.7}$$

where $\omega_z = \sqrt{\frac{qV_0}{md^2}}$ is the axial frequency of the particle. The motion of the particle in the x and y directions is more complicated because the motion components are coupled

to the magnetic field via the Lorentz force (the term $\mathbf{v} \times \mathbf{B}$ is no longer zero). Since $\mathbf{B} = B\hat{z}$, the force is given by

$$m\frac{d^2r}{dt^2} = q\left(-\bigtriangledown\Phi + B\frac{d\mathbf{r}}{dt} \times \hat{z}\right), \tag{4.8}$$

and the motion equations for x and y become

$$\begin{aligned} \frac{d^2x}{dt^2} - \omega_c\frac{dy}{dt} - \frac{1}{2}{\omega_z}^2 x = 0 \\ \frac{d^2y}{dt^2} + \omega_c\frac{dx}{dt} - \frac{1}{2}{\omega_z}^2 y = 0, \end{aligned} \tag{4.9}$$

where $\omega_c = \frac{qB}{m}$ is the cyclotron frequency. The motion in the $x-y$ plane can be solved by introducing a complex substitution $u = x + iy$, allowing the equations 4.9 to be written as one:

$$\frac{d^2u}{dt^2} + i\omega_c\frac{du}{dt} - \frac{1}{2}{\omega_z}^2 u = 0. \tag{4.10}$$

The solution of this complex differential equation can be written in the form $u = e^{-i\omega t}$, thus reducing it to a quadratic equation

$$\omega^2 - \omega_c\omega + \frac{1}{2}{\omega_z}^2 = 0, \tag{4.11}$$

which solutions are

$$\omega_\pm = \frac{1}{2}\left(\omega_c \pm \sqrt{\omega_c^2 - 2{\omega_z}^2}\right). \tag{4.12}$$

For real roots of this equation to exist, i.e. the condition for confinement in $x-y$ plane to be fulfilled, it is required that $\omega_c^2 > 2{\omega_z}^2$. ω_+ is the so-called modified cyclotron frequency, and for $\omega_c \gg \omega_z$, the positive root is identified as the standard cyclotron motion, $\omega_+ \simeq \omega_c$. The negative root, ω_- is called magnetron frequency $\omega_- = \omega_m$ and is, in fact, the $\mathbf{E} \times \mathbf{B}$ drift motion, i.e. the slow rotation of the particles around the z axis. In conclusion, the motion of the trapped particles in a Penning-Malmberg trap is a superposition of three oscillatory modes, axial, cyclotron and magnetron, as shown in fig. 4.7, and with the corresponding frequencies listed below (eq. 4.13-4.15):

$$\omega_z = \sqrt{\frac{qV_0}{md^2}} \qquad (axial\ motion) \tag{4.13}$$

$$\omega_c = \frac{qB}{m} \qquad (cyclotron\ motion) \tag{4.14}$$

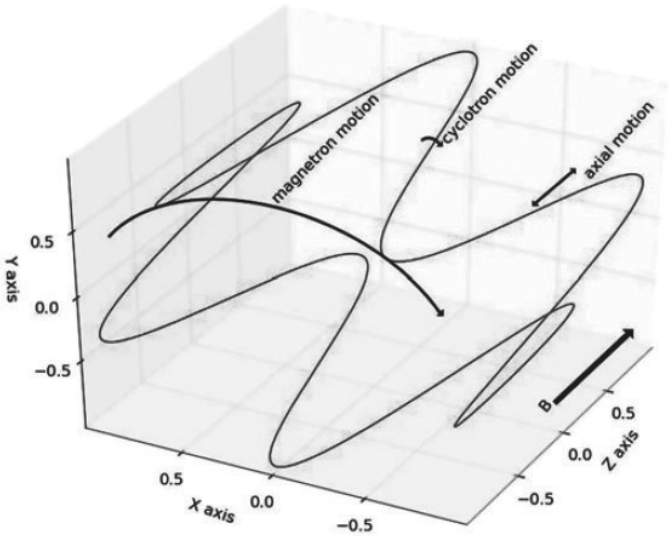

Figure 4.7: Illustration of the motion of a single particle in a Penning-Malmberg trap: a superposition of three oscillatory modes: the slow magnetron oscillation around z axis, the axial vibration along z and the fast cyclotron orbit [24].

$$\omega_m = \frac{{\omega_z}^2}{2\omega_c} \qquad (magnetron\ motion). \tag{4.15}$$

The behaviour of a collection of charged particles that is large in all of its dimensions compared to the Debye length (so-called non-neutral plasma) differs from the motion of a single trapped particle mainly due to space charge effects (the Debye length is defined as $\lambda_D = \sqrt{\frac{\varepsilon_0 k_B T}{q^2 n_0}}$, where ε_0 is the vacuum permittivity, k_B is the Boltzmann constant and n_0 is the density of the charged particles). Without going into the details of the dynamics of the plasma in Penning-Malmberg traps, which is beyond the scope of this thesis, an insight of the electrostatic potential, Φ will be given. In a Penning-Malmberg trap, Φ is a sum of the trap potential Φ_T, the space charge potential Φ_s that arises from the Coulomb interactions among the charged particles and the image charge potential Φ_i, which occurs due to the induced image charges in the trap electrodes and is negligible when the plasma is far from the electrodes:

$$\Phi(x,y,z) = \Phi_T + \Phi_s + \Phi_i. \tag{4.16}$$

To achieve an almost square-like trap potential, the central long electrode (or set of electrodes) in a Penning-Malmberg trap is grounded ($V_C = 0$) and the axial confinement of the charged particles is achieved by applying a potential V_T to the two outer (end cap) electrodes, such that the product qV_T is positive. In this way, the potential well is flat

along the trap, except in the region near the end caps, so the particles bounce back and forth inside the trap. The distance from the center of the central electrode to the end-cap is usually much larger than the inner radius of the electrode. The trap potential Φ_T inside the Penning-Malmberg trap is zero. If a plasma with radius r_p and uniform density n_0 is confined inside the trap, the radial self-electric field can be determined by integrating the following Poisson equation (applying Gauss's law):

$$\frac{1}{r}\frac{\partial}{\partial r}[rE_r(r)] = -\frac{qn_0(r)}{\varepsilon_0} \tag{4.17}$$

where $r = \sqrt{x^2+y^2}$ is the radial distance from the axis of symmetry and

$$n_0(r) = \begin{cases} n_0 = const, & r \le r_p \\ 0, & r > r_p \end{cases} \tag{4.18}$$

is the density profile of the plasma. Hence

$$E(r) = \begin{cases} \frac{qn_0}{2\varepsilon_0} r, & r \le r_p \\ \frac{qn_0 {r_p}^2}{2\varepsilon_0}\frac{1}{r}, & r > r_p \end{cases} \tag{4.19}$$

is the obtained radial electric field. Consequently, the space charge potential Φ_s will be of the form:

$$\Phi_s(r) = \begin{cases} -\frac{qn_0}{4\varepsilon_0} r^2 + C, & r \le r_p \\ -\frac{qn_0 {r_p}^2}{4\varepsilon_0}\left(1 + 2\ln\frac{r}{r_p}\right) + C, & r > r_p. \end{cases} \tag{4.20}$$

The integration constant C can be obtained from the boundary condition of the inner surface of the grounded electrode, i.e. $\Phi_s(r_0) = V_C = 0$, which results into

$$C = \frac{qn_0 {r_p}^2}{4\varepsilon_0}\left(1 + 2\ln\frac{r_0}{r_p}\right). \tag{4.21}$$

In order to axially trap N particles in a Penning-Malmberg trap, the trap voltage V_T must be larger than the space charge voltage V_s induced by a plasma with length L and radius r_p in a trap with inner radius r_0, which is

$$V_s = \frac{qN}{4\pi\varepsilon_0 L}\left(1 + 2\ln\frac{r_0}{r_p}\right). \tag{4.22}$$

Radial confinement of the plasma is provided by a uniform axial magnetic field. The radial electric field arising from the non-neutrality of the plasma (due to its space-charge), which is perpendicular to the magnetic field, causes the plasma to rotate azimuthally ($\mathbf{E}\times\mathbf{B}$ motion) with drift velocity $v_{E\times B} = \frac{\mathbf{E}\times\mathbf{B}}{B^2}$ and frequency $f_{E\times B} = \frac{ne}{4\pi\varepsilon_0 B}$, where n is the density of the plasma. On the other hand, charged particles moving in a magnetic field experience the Lorentz force, which forces them to move spirally around the magnetic fields line (cyclotron oscillation). Hence, the azimuthal rotation of the plasma gives rise to the opposing Lorentz force ($q\mathbf{v}\times\mathbf{B}$), which is radial and directed inwards, thus balancing the space charge radial field.

The Penning-Malmberg trap in the 5 T region of the AEḡIS experiment (the axial magnetic field providing the radial confinement) is composed of 1 m long stack of

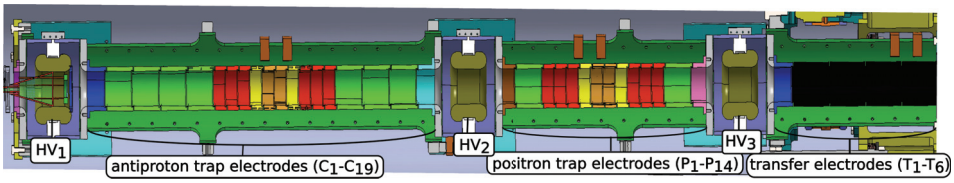

Figure 4.8: Schematic view of the trap system placed in the 5 T magnet to manipulate the antiproton and the electron plasma, as well as to transfer them to 1 T magnet.

cylindrical electrodes with inner radius of 15 mm, schematically shown in fig. 4.8. To meet the requirements for manipulating the antiproton (and the positron) plasma, three different types of electrodes are included in the design: standard gold-plated aluminum low voltage ($\pm$200 V) electrodes, split electrodes (gold-plated aluminium) for rotating wall compression (spilt azimuthally into 4 equal sectors) and high voltage (max 20 kV) electro-polished titanium electrodes.
After being slowed down to a kinetic energy of few hundred keV with the degraders, the antiprotons arrive at the trap entrance and at this moment HV_1 is grounded to allow them to enter into the trap, while HV_2 is at high voltage (currently, the maximum value of the applied potential is 9 kV). Antiprotons with kinetic energies $\leq eV_{HV_2}$ are reflected from HV_2 and bounce back within 500-700 ns, the time needed for antiprotons to pass twice the distance (46 cm) between HV_1 and HV_2 [105]. During this short period, the HV_1 electrode is polarized by applying the same voltage as HV_2 and the antiprotons are trapped longitudinally. The geometry that AEḡIS adopted for the traps, the so-called *Multi-Ring Electrode* (MRE), allows for an axially long harmonic potential region whose length and position along the axis can be controlled by changing the voltages applied to the electrodes. The trapping region for the antiprotons, according to the design, can be extended to HV_3, thus increasing the length from 46 cm to 76 cm [105].

The next phase involves electron cooling of the antiprotons with previously loaded electrons in the trap, coming from a source (barium oxide disc cathode) mounted outside the cryostat [31]. The same charge sign of antiprotons and electrons allows their confinement in the same volume inside the traps, using the same voltage polarity. A narrow, low voltage potential well ($V_{lp} = \pm 200$ V) [31] inside the large one (where all the antiprotons are trapped) is created for storing the preloaded electrons. The antiprotons are cooled down through Coulomb collisions with the electrons. Although electrons are heated during this procedure, they immediately cool themselves by emission of cyclotron radiation. Their cooling time constant in a 5 T magnetic field is 0.1 s. In an ideal case, antiprotons and electrons will both have the same temperature as the environment after reaching thermal equilibrium. As achieved already at LEAR [129] and proved also in ATHENA, electron cooling of $\sim 10^4$ antiprotons from initial energies of few keV down to few eV can be achieved with electron cloud density of $\sim 10^7 - 10^8$ cm^{-3} [17].

The diagnostics of the the electron cooling efficiency is performed by lowering the potential on HV_1 electrode to ground in order to release and detect the antiprotons that have not been cooled down, the so-called "hot dump". The antiprotons with energy

lower than qV_{lp} together with the electrons will remain in the low potential well. The same procedure is afterwards applied to detect the "cold dump". The measurements during the first commissioning of the AEḡIS apparatus showed a cooling efficiency of 90% [105]. Successful trapping and cooling of antiprotons at this stage is important to obtain a sufficient number of antiprotons, which will increase the efficiency of antihydrogen production, thus decreasing the overall time necessary for the statistics for the 1% precision measurement. The positron cycle, as previously described, lasts $\sim$ 300 s, while one AD cycle is as short as $\sim$ 100 s. This timing mismatch allows the accumulation (stacking) of antiprotons from several AD shots, which is foreseen for the final configuration of the AEḡIS experiment. During accumulation, the method for trapping and cooling down of antiprotons for every next bunch is the same as for the first one: while the cold antiprotons, mixed with the electrons are confined in the small potential well, the potential on the HV_1 electrode is gradually lowered to ground to allow access for the new bunch. As the size of the antiproton plasma increases with the stacking, a possible radial compression of the antiproton cloud [130], using the rotating wall technique is considered [31]. This may affect the cooling of the antiprotons, since they are heated up during compression. Unlike electrons, their mass is too large for effective cyclotron cooling in the 5 T magnetic field. Therefore, other techinques like sideband cooling are taken into account and preliminary studies have been carried out [131].

The transfer trap is the termination of the trap system in the 5 T region and its main purpose is the transport of particles (antiprotons together with electrons, and separately positrons) to the 1 T traps. It is composed of six electrodes situated in the central region where the inhomogeneity of the magnetic field is high due to the transition from the 5 T to the 1 T magnet. Particles are transferred by appropriately changing the electrode's voltages during their movement.

4.3.2.2 1 T storing traps and antihydrogen production trap

The new, original, double stack design of the 1 T traps in the AEḡIS experiment provides different regions for manipulating the positrons and the antiprotons (as shown in fig. 4.5). After the transfer of the particles from the trap enclosed in the 5 T magnet, they first enter into the initial part of the 1 T trap system (with a radius of 22 mm), which is common for both antiprotons and positrons. This so-called large radius trap is devoted to the radial compression of the plasmas with rotating wall technique [121], as well as moving the positron plasma off-axis. The decrease of the magnetic field from 5 T to 1 T results in an expansion of the plasma with a radial increase of a factor $\sqrt{5}$. To be able to enter the double stack trap region, with a radius of 5 mm, both plasmas need to be reduced in size. Two of the electrodes in the 1 T region are azimuthally divided into 4 sectors to provide rotating electric field asymmetry to compress both the antiproton and the positron plasma before they are injected into each of the double stack traps. The displacement of the positrons into the off-axis trap will be performed through the autoresonant excitation of the $m = 1$ diocotron mode [132, 133].

The diocotron mode is, in fact, a perturbation in the density of the plasma cylindrical column formed inside the Penning-Malmberg trap. When such a perturbation occurs, the plasma performs two rotational motions: the first one is the rigid rotation of the plasma around its axis due to the $\mathbf{E} \times \mathbf{B}$ drift from the plasma's own electric field; the other one appears when the plasma column is slightly moved off-center and is li-

able to a second drift $\mathbf{E_i} \times \mathbf{B}$, arising from the electric field $\mathbf{E_i}$ of the plasma image in the conducting wall of the electrodes. Since the direction of this drift always points to the center of the trap, the resulting motion is the plasma orbiting around the trap center. Tests with electron plasma as a proof of principle have already been performed [134]. An external drive signal, with a suitable frequency for the specific off-axis displacement which will invoke the auto-resonant diocotron motion, will be applied to the sectored electrode. After its displacement, the positron plasma will be injected into the off-axis trap. The common large radius trap in the 1 T field ends with a flat plate with two openings (with 5 mm radius each) to allow the corresponding particles to continue their way into one of the double stack traps. When the positrons are placed in the off-axis trap, they are re-confined, stored and compressed in the first part of the off-axis trap (with a total length of 28 cm and maximum trapping length of 25 cm). Next, the positron cloud is accelerated towards the positronium conversion target by applying high voltage to the central electrodes (up to 10 kV). The target is kept at ground potential, so that the positrons can be accelerated as they leave the trap. When in contact with the target, some of them are converted into positronium, which can then be laser excited to Rydberg states (as described in sec. 4.3.1).

Cooled antiprotons continue their passage through the on-axis trap together with the previously loaded cooling electrons. The size of this trap is identical to the size off-axis trap and its main purpose is the manipulation and controlled transport of the antiprotons to the antihydrogen production trap, where the charge exchange reaction will take place.

4.3.3 Antihydrogen beam formation

4.3.3.1 Cooling of antiprotons to 100 mK in the antihydrogen production trap

The antihydrogen formation trap is an aligned continuation of the on-axis trap of the double stack, having the same radius (5 mm, fig. 4.5). Here, antiprotons will arrive together with the electrons previously used for their cooling and will be further cooled down to $\sim$ 100 mK before the arrival of positronium and prior to the charge exchange reaction. Cooling of antiprotons through the emission of cyclotron radiation in the provided magnetic field is not possible due to their large mass, so Coulomb interactions with electrons are essential for reducing the temperature of the antiprotons to 100 mK. It is of great importance for the antihydrogen to be produced at sub-kelvin temperatures so that the flux of antihydrogen reaching the position detector is as large as possible (see sec. 4.3.3.2).

Electrons, which are $\sim$ 2000 times lighter than antiprotons, radiate their cyclotron energy and reach thermal equilibrium by absorbing black body photons emitted from the surroundings. This process is effective if the temperature of the environment is higher than few K, because at lower temperatures the thermal equilibrium can not be reached. The reason is the low number of radiated photons from the environment with frequency close to the cyclotron frequency of the electrons (thus able to excite the electrons radial motion). At such low temperatures, quantum effects become important. The energy E_c of the cyclotron motion of an electron with a frequency ω_c in a Penning trap is

$$E_c = \left(n_c + \frac{1}{2}\right)\hbar\omega_c. \tag{4.23}$$

The electron will radiate this energy until reaching the ground state ($n_c = 0$). Hence, the minimum radial energy of an electron in a magnetic field with magnitude B is

$$E_{min} = \frac{\hbar eB}{2m_e} \tag{4.24}$$

which, in the case of 1 T magnetic field, would give a minimum energy of $\sim 0.093 \cdot 10^{-22}$ J, corresponding to a temperature of ~ 0.5 K. This is the minimum temperature to which the electrons can be cooled via cyclotron radiation. Nevertheless, the axial oscillations of electrons confined in a Penning trap are usually in the radio-frequency range and are thus much lower than the cyclotron oscillation frequencies. For example, the axial frequency of electrons for a potential of ~ 1 kV is ~ 20 MHz and the quantum energy limit for their axial motion for a frequency of 10 MHz is 240 μK. This allows for electrons to be cooled to temperatures in the order of few hundred μK by cooling them axially. Nevertheless, the low radiation rate of the axial energy imposes the need of a method for external cooling. In AEḡIS, the axial cooling of electrons in the 1 T region will be carried out by applying the resistive cooling mechanism [135], where the idea is to make use of a cryogenic electronic circuit, tuned to resonate to the axial frequency of the electrons and coupled to their axial motion, so that the electrons dissipate their kinetic energy into this external circuit. Additional techniques for reducing the antiproton temperature even below 100 mK are considered for the future phases of the experiment, such as cooling of antiprotons with negative ions [136], laser ("Doppler") cooling [137] and evaporative cooling [138]. The environment in the small antihydrogen formation region in the 1 T magnet will be kept at 100 mK by means of a dilution refrigerator cryostat [31]. The procedure to separate and remove the electrons is not straightforward and can not be carried out without changing the electric field inside the traps, thus giving the antiprotons an additional potential energy comparable to eV. This value is not negligible, as the expected value of the energy of the antiprotons and electrons right after their transfer is in the eV range. Hence, the electrons will remain in the antihydrogen production trap when the charge-exchange reaction takes place [31].

4.3.3.2 Charge-exchange reaction and production of antihydrogen

After the antiprotons are cooled down to 100 mK, the positronium atoms coming from the conversion target are spread over the antiproton cloud in the production trap (see fig. 4.9). The positronium enters into this trap through small openings with a honeycomb structure, introduced on top of the electrodes. The size of the mesh holes is kept as small as possible so that the electric field is not disturbed. The width of one hexagonal hole is 0.6 mm, and the thickness of the wall between the two hexagonal holes is 50 μm. To ensure a maximum possible transmission for positronium, the transparency of the honeycomb mesh is designed to be $\sim 80\%$. The prototype of the experimental set-up for the charge exchange reaction is given in fig. 4.9.

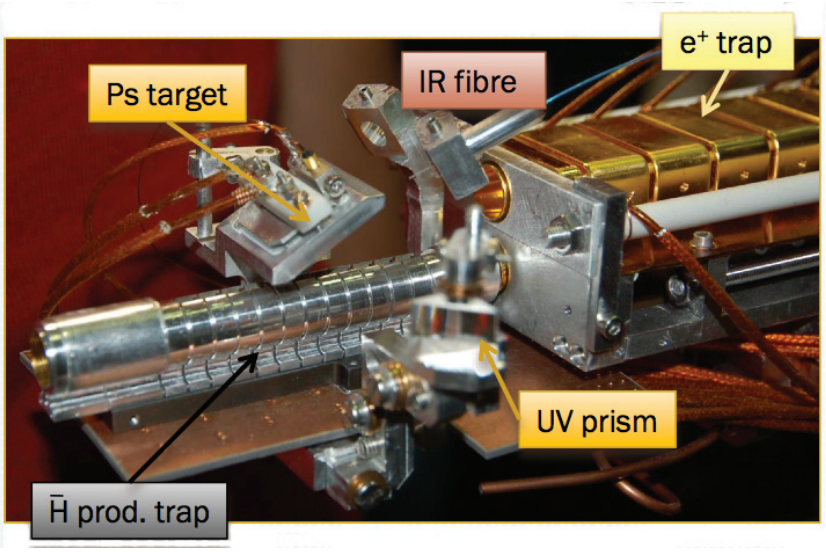

Figure 4.9: Prototype of the ultra cold trap, where the antihydrogen production takes place, together with the positronium target and the laser system for its excitation.

The charge exchange method [139] was exploited for the first time in the ATRAP experiment [140, 141], where antihydrogen production was performed by a double charge exchange reaction with excited Cs atoms. The difference in the AEgIS production scheme is in the formation of a pulsed beam, which is required to have a defined initial time for the antihydrogen beam which, together with the arrival time on the detector is needed to calculate the time during which the antihydrogen atoms drop. This time of flight together with the vertical deflection allows calculating the acceleration for antihydrogen in Earth's gravitational field.

The main advantages of antihydrogen production through the direct charge exchange reaction between cold antiprotons and Rydberg state positronium are:

- The strong dependace of the cross section of the reaction on the positronium principal quantum number, $\sigma \propto {n_{\mathrm{Ps}}}^4$ [126], allows obtaining a high production efficiency using Rydberg state positronium. This dependence arises from the mere fact that the radius of the positronium in Rydberg states with principal quantum number n_{Ps} can be approximated as $a_0 {n_{\mathrm{Ps}}}^2$, where a_0 is the Bohr radius. Therefore, the geometric area of interest for the cross section becomes $\pi {a_0}^2 {n_{\mathrm{Ps}}}^4$.

- The distribution of the principal quantum number of the final states of the formed antihydrogen is predetermined by the quantum state of the positronium engaged in the charge exchange reaction, with a mean value $n_{\bar{\mathrm{H}}} = \sqrt{2} n_{\mathrm{Ps}}$. Even if all the positronium atoms involved in the collision initially are in the same state, the outcoming antihydrogen states will form a n-levels distribution centred around the resonant state. In the collision process almost all l, m sub-levels can be populated with the same probability. This implies that the $\bar{H}(n)$ atom are born with a random

dipole moment. Nevertheless, by tuning the positronium states with lasers, one can establish control over the final states of the produced antihydrogen.

- The charge exchange method allows the production of ultra cold antihydrogen, and this aspect is of great importance for the precision of the $\bar{g}$ measurement. The colder the antihydrogen is, the lower the transverse velocity of the antihydrogen, which will prevent large radial spread of the beam. Given the finite size of the position detector, greater flux of the antiatoms arriving on the detector is obtained. The temperature of the formed antihydrogen is mainly determined by the temperature of the antiprotons and they need to be cooled to sub-K temperatures.

Although the velocity of the formed antihydrogen is given mostly by the velocity of the antiprotons (the mean value at 100 mK is $\sim$ 41 m/s), other parameters should not be neglected, such as the velocity of the positronium ($\sim 10^4$ m/s), contributing with 15-20 m/s to the final antihydrogen velocity. Even if both the antiproton and the positron are at rest when they recombine, the obtained antihydrogen velocity is zero only if $n_{\bar{\mathrm{H}}} = \sqrt{2} n_{\mathrm{Ps}}$. As previously mentioned, this is not always true since the distribution of the principal quantum number of the produced antihydrogen, $\mathrm{n}_{\bar{\mathrm{H}}}$, is never monochromatic. This results in a contribution to the antihydrogen velocity of another 15-20 m/s. In total, the expected velocity of the antihydrogen is 25-80 m/s [31].

Despite the strong dependence of the cross section, σ, on the principal quantum number of the positronium, it is also determined by the relative velocity between the positronium and the antiproton that participate in the charge exchange reaction. This effect is known as velocity matching: if the relative velocity between antiproton and positronium matches the velocity of the Rydberg positronium internal motion, the cross section is large [126, 142]. As the velocity of the positronium ($\sim 10^4$ m/s) is much higher than the one of the antiproton ($\sim$ 41 m/s) prior to their recombination into antihydrogen, their relative velocities are basically given by the velocity of the positronium center of mass, which means that the positronium has to be cold.

When the positronium and the antiprotons are in contact, the production of the antihydrogen will happen in a very short time interval of $\sim$ 1 µs [143]. The resulting antihydrogen will be emitted isotropically and will drift towards and annihilate on the walls of the trap, unless it is trapped or forced to move in a given direction. In AEḡIS, the gravity measurement will be performed in flight, by creating a beam of antihydrogen rather than trapping it. Apart from their impact on the cross section, Rydberg states of the antihydrogen are also essential for the Stark acceleration. This is due to the large dipole moment of the Rydberg states that is required to obtain an acceleration of the antihydrogen atoms when applying the inhomogeneous electric field. A time-varying electric field (kV/µs) will be applied to accelerate the antihydrogen atoms to few hundred m/s. A similar technique has already been demonstrated for deceleration of hydrogen [144], where a beam of atoms with velocity of $\sim$ 700 m/s and principal quantum number n in the range between 15 and 40 has been successfully stopped in $\sim$ 5 µs within a distance of 1.9 mm. The presence of a magnetic field will affect the energy levels with a linear term (Zeeman effect) and a quadratic term (diamagnetic effect) and can lead to energy level crossings or even to a chaotic regime. The magnitude of 1 T was chosen as an intermediate value between the necessary high field to confine the charged particles prior to the antihydrogen production and the low field that would not

invoke mixing of the states and would not prevent the acceleration of the antihydrogen atoms, but has not been optimized yet.

After the beam is formed and accelerated towards the gratings of the moiré deflectometer, the next step is the gravity measurement that will be described in detail in the following section.

4.3.4 Antihydrogen detection and gravity measurement

The production of cold antihydrogen in AEḡIS will be measured with an annihilation detector built around the antihydrogen production trap. The Fast Annihilation Cryogenic Tracking (FACT) detector will operate inside the 1 T magnet bore, in vacuum (10^{-6} mbar) at 4 K temperature [25]. It consists of four layers of multi-clad scintillating fibres coupled to clear fibres of the same diameter and read out with 800 silicon photomultipliers. The scintillating light produced in the scintillating fibres is guided through clear fibres from the cryogenic region to Hamamatsu Multi-Pixel Photon Counters (MPPC) at room temperature. Each MPPC is composed of 100 Geiger mode Avalanche Photo Diodes (APDs) operating in parallel. All these components are placed inside the vacuum. The MPPC signal is read out with a FPGA through an amplifier and a fast discriminator. The amplifiers are mounted on PCBs placed outside the vacuum, at room temperature. The detection of antihydrogen is based on the detection of charged pions from the annihilation and reconstruction of the annihilation vertex by extrapolation of their tracks back to the interception point. According to GEANT4 simulations, an annihilation vertex resolution along the axis, σ_z, of 2.1 mm is expected. A schematic overview of the FACT detector is given in fig. 4.10.

As mentioned in sec. 4.3, in the first phase of the AEḡIS experiment a gravity measurement with 1% precision, based on the vertical deflection of an antihydrogen beam passing through a moiré deflectometer will be attempted. The magnitude of the deflection depends on the velocity distribution of the accelerated antihydrogen atoms. The AEḡIS apparatus is designed to allow the production of a beam with horizontal velocity of few hundred m/s and a transverse velocity of few tens m/s. As an example, if the velocity of the beam is 500 m/s and it passes through 1 m of horizontal path before hitting the detector, the vertical deflection in case $\bar{g} = g$ would be ~ 20 μm. In principle, knowing the initial position (production point) of each antihydrogen atom and its horizontal velocity, and measuring the vertical displacement of the atoms after a certain length of flight would be sufficient to obtain the value of $\bar{g}$. However, the production of a perfectly collimated antihydrogen beam, a precise determination of the beam center and sustainability of its absolute position within few μm requires a mechanical stability of the whole apparatus that is very difficult, if not infeasible to achieve in practice. For these reasons, AEḡIS will make use of a moiré deflectometer consisting of two gratings coupled to a position sensitive detector. The gravity measurement will take place in the so-called gravity module: an independent set-up mounted in a cylindrical tube that will be attached at the end of the 1 T magnet, outside of the magnetic field. The magnetic field gradient in the intermediate region between the end of the antihydrogen production trap and the beginning of the gravity module is unavoidable and at the same time particularly undesirable, as the gravity force must be the only force acting on the antihydrogen atoms during their flight. Given the force $F_z = \mu_z \frac{dB_z}{dz}$ experienced by the

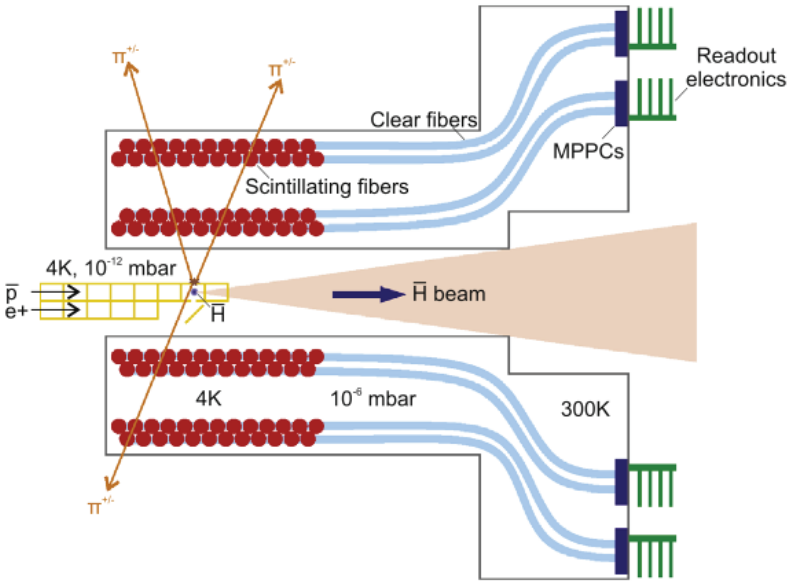

Figure 4.10: Schematic overview of the Fast Annihilation Cryogenic Tracking (FACT) antihydrogen detector. The scintillating fibres are shown with red circles. The radial distances of the layers are 70 mm and 98 mm from the beam axis. The clear fibres used to transport the scintillating light from the cryogenic region to the room temperature readout electronics are shown with blue lines. An annihilation event inside the antihydrogen production trap is shown. The vertex is reconstructed by extrapolating the tracks of the charged pions (shown with orange lines) [25].

antihydrogen due to an inhomogeneous magnetic field, to obtain a precision of 1%, the magnetic field gradient must be reduced to

$$\frac{dB_z}{dz} < 0.177 \frac{1}{m_l + 2m_s} Gauss/m \quad [31], \tag{4.25}$$

where m_l and m_s are the magnetic and secondary spin quantum number of the antihydrogen atom. Hence, a proper magnetic shielding is of great importance to suppress a possible systematic error on the gravity measurement.

When produced, at 100 mK, the antihydrogen atoms will have radial velocity that will follow a Maxwell distribution. Once accelerated, the beam will diverge over ~ 1 m of horizontal distance, passing through the gratings before reaching the detector, as shown in fig. 4.11. Two identical gratings will act as a collimator of the beam, thus eliminating the necessity of having a collimated beam. The moiré deflectometer operates in a classical regime: the de Broglie wavelength of the antihydrogen is orders of magnitude smaller than the grating period and diffraction effects are negligible. When the diverging beam passes through the gratings, some propagation directions will be selected. $\bar{H}$ atoms that pass through the deflectometer will produce a fringe (shadow)

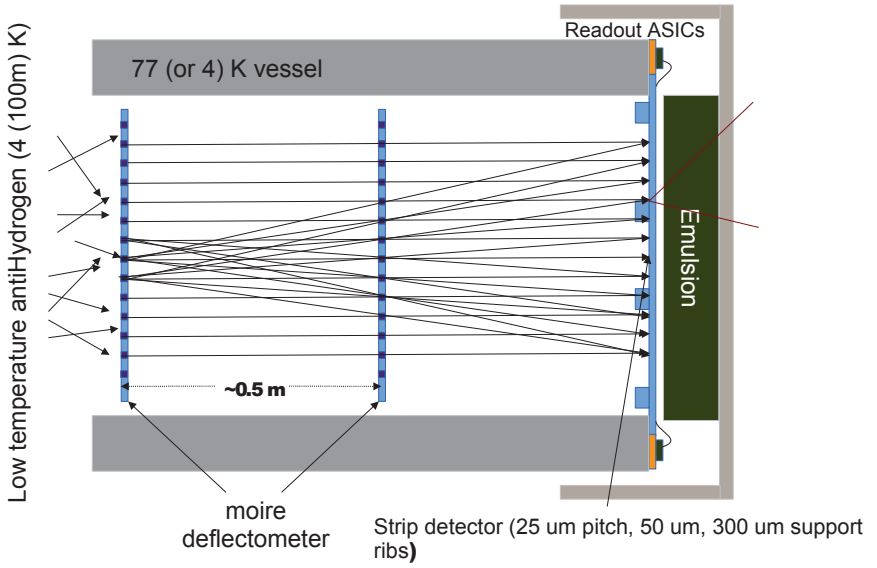

Figure 4.11: Schematic overview of the propagation of the antihydrogen beam throuhg the two-grating Moiré deflectometer before being detected by the position sensitive detector.

pattern on the detector, with the same period as the gratings (see fig. 4.12). The effect of gravity will be visible through the vertical shift of this pattern as a function of transit time. The gravitational acceleration for antihydrogen will be determined by measuring, for every $\bar{H}$ atom reaching and annihilating on the detector's surface, the vertical "fall" in Earth's gravitational field(Δ_x) expressed in units of the grating period (information that is revealed from the shift of the pattern) and the time of flight between the two gratings and the detector $T = L/v_z$:

$$\frac{\Delta_x}{d} = -\frac{g}{d}T^2 = -\frac{g}{d}\frac{L^2}{v_z{}^2}. \tag{4.26}$$

T will be reconstructed from t_0, the time when the accelerating electric field is switched off, and the arrival time t_{det} of the antihydrogen on the position sensitive detector. Knowing the distance L, the axial velocity can then be easily calculated. The vertical displacement of the pattern will depend on the velocity of the antihydrogen atoms: the slower the atoms are, the greater the deflection in the Earth's gravitational field. The simulated signal of the detector, obtained from the annihilations of antihydrogen atoms with two different velocities is shown in fig. 4.12. The vertical shift is given in grating period units (d) and it is clearly visible that when the velocity is larger (600 m/s in this case) the vertical shift of the fringe pattern is smaller.

The procedure for calculating $\bar{g}$ can be explained by starting with the assumption that $\bar{g} = 0$ m/s^2, in which case the pattern will not be shifted with respect to the position of the gratings. If we assume that $\bar{g} = 9.81$ m/s^2, the fringe pattern will shift accordingly with the beam velocity. If antiatoms having different axial velocities are grouped together, then each group will contribute to the signal with its own phase shift.

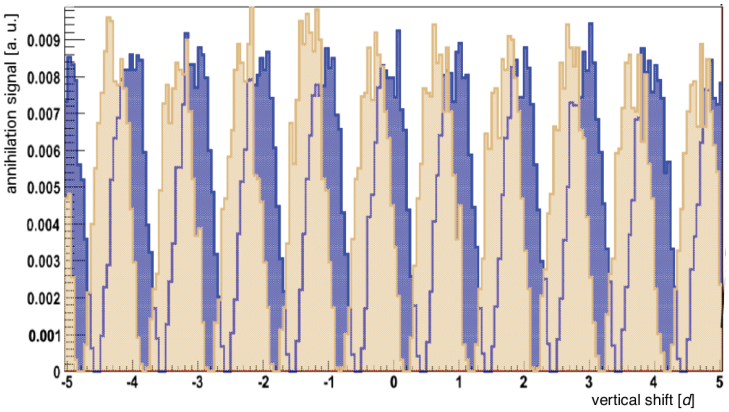

Figure 4.12: Simulation of the detector signal (annihilation signal in arbitrary units) vs vertical position on the detector (in grating period d units) showing the moiré pattern produced from the antihydrogen atoms passing through the two gratings. In blue: signal from antihydrogen atoms with axial velocity $v_z = 600$ m/s; in grey: distribution signal from antihydrogen atoms with axial velocity $v_z = 250$ m/s a distance between the gratings of $L = 40$ cm and a period $d = 80$ µm have been considered in this simulation.

It was verified with simulations that when the number of antihydrogen atoms annihilating at the detector ($N(\Delta_x)$), and having a distribution of T^2 symmetric around its mean value $\langle T^2 \rangle$ (where x is the direction of the gravity force) are grouped together, the phase shift due to gravity is independent of the shape of the distribution of T^2. The phase, or fringe shift is related to the classical deflection Δ_x:

$$\Delta\Phi_g = \frac{2\pi\Delta_x}{d} = \frac{2\pi}{d} g T^2 \tag{4.27}$$

This means that by grouping the data for the time-of-flight (T) in symmetrical intervals (T_1, T_2), despite the different σ_{T^2} for each distribution, the phase shift would remain unchanged within its error. When the annihilated antihydrogen atoms are grouped in symmetric T^2 distributions according to their time-of-flight, the signal from the position detector, obtained by selecting all the atoms within one distribution, gives the mean value of the vertical displacement Δ_x and subsequently, the phase shift $\Delta\Phi_g$ for the corresponding distribution. Finally, the value for $\bar{g}$ is obtained by plotting the phase shift as a function of the mean value $\sqrt{\langle T^2 \rangle}$, and by fitting these points with a quadratic fit.

The most significant source of errors related to the gravity module that could influence the precision of the gravity measurement is the vertical alignment of the gratings themselves and the position detector. The alignment precision of the relative position of the gratings has to be in the order of a fraction of the grating period, i.e $\sim$ µm. Moreover, the stability has to be maintained over a long period of time during the data taking. The alignment control of the gravity module will be performed by continuous monitoring with laser light that will produce a signal on the detector. The effect of different systematic errors can be tested by comparison of the results obtained when the gratings are rotated by 90° around the z axis, in which case the effect of gravity is "turned off".

4.3.4.1 Silicon detector requirements

The position detector in AEḡIS is a hybrid detector that will consist of a silicon strip detector where the antihydrogen annihilation will take place, and an emulsion detector [145] for detection of annihilation prongs and reconstruction of the annihilation point with more precision. A scintillation fibre tracking telescope to provide the time-of-flight information for the emulsion part is also foreseen.

The silicon position detector will give an on-line measurement of the annihilation events by providing spatial information of the antihydrogen annihilation position together with the arrival time for each antihydrogen atom. This detector will also act as a separation membrane between the ultra-high vacuum ($\sim 10^{-12}$ mbar), where the antihydrogen formation and propagation through the moiré deflectometer will occur, and the secondary vacuum ($\sim 10^{-6}$ mbar) where the emulsion detector will be installed. The vicinity of the silicon detector with respect to the antihydrogen production trap ($\sim$ 1 m distance) imposes a constraint on its operating temperature: the detector will be kept at 77 K or lower, in order to avoid black body radiation to increase the antiproton plasma temperature, which would increase the thermal velocity of the antihydrogen and reduce its flux.

The precision of the gravity measurement depends, most of all, on the number of reconstructed annihilation vertices, N. Simulations showed that, in case of infinite position resolution of the detector ($\sigma_{\Phi_g} = 0$), the precision in the determination of the phase shift due to gravity is given by [31]

$$\sigma_{\Phi_g} = \frac{0.4}{\sqrt{N}} rad, \tag{4.28}$$

where N is the number of detected antiatoms, which is determined by the number of antihydrogen atoms arriving at the detector and its efficiency. The fraction of antihydrogen atoms arriving at a detector surface of radius w, from a production point at a distance l from the detector is

$$f_N = \frac{w^2}{l^2} \frac{{v_h}^2}{{v_t}^2}, \tag{4.29}$$

where v_h and v_t are the horizontal (axial) and the transversal (radial) velocity of the antihydrogen respectively. Thus, for $l = 1$ m, $v_h = 500$ m/s and $v_t = 50$ m/s, we obtain that the minimum size of the detector and consecutively the size of the gratings allowing to detect all the antihydrogen atoms is in the order of $\sim$ 10 cm. Part of these atoms will annihilate on the gratings, depending on their opening fraction. According to the current design, the gratings and the detector will be produced from standard 6 inch (15.24 cm) silicon wafers and will have a radius that is large enough so that the antihydrogen losses are mainly due to the grating transparency. It was already verified that best resolution for small fringe shifts can be achieved with an open fraction of $\sim$ 30% [119]. Simulations with a detector size of 20 cm, distance between the gratings of $L = 40$ cm, a period $d = 80$ μm and an opening fraction of 0.3 showed that the fraction of transmitted atoms is 9% [31].

When the position resolution of the detector is included in eq. 4.28, an appropriate increase of σ_{Φ_g} is obtained, e.g. from factor 2 for a position resolution $\sigma_{det} = 10$ μm

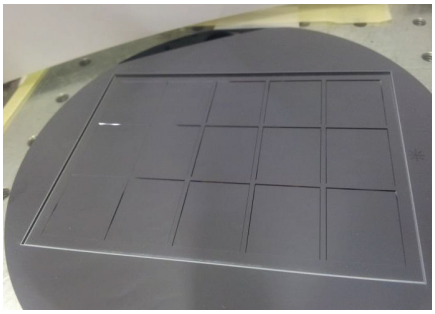

Figure 4.13: Picture of the 6 inch silicon wafer with the prototype sensor before cutting out. The thin areas are 50 μm thick and 5×3 cm^2 large. The support ribs are 300 μm thick. The border around the sensor is 4 mm.

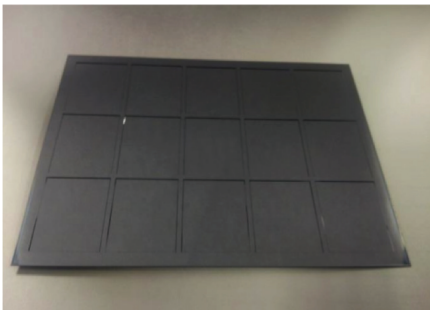

Figure 4.14: The prototype sensor after laser cutting of the wafer.

to factor 4 for $\sigma_{det} = 17.5$ μm. For larger values of σ_{det} the impact of the systematic errors on the phase value becomes important, which results in a requirement for a position resolution not worse than 10-13 μm for the silicon detector. The number of reconstructed annihilation events needed to achieve a precision of 1% on $\frac{\Delta g}{g}$ for this position resolution is 10^4-10^5 [31].

According to the current design, the silicon detector will consist of a single-sided silicon strip sensor with a strip pitch of 25 μm, bonded to an application specific integrated circuit (ASIC) to read out the signal. The sensor will be mounted on a silicon mechanical support wafer, 300 μm thick, together with the readout electronics will be mounted. A silicon mechanical support will ensure a perfect match of the thermal expansion coefficient with the sensor, which is important due to the cryogenic operation environment (77 or 4 K). A thickness constraint of 50 μm is imposed to allow for annihilation prongs such as pions and protons to reach the emulsion detector, experiencing minimal scattering. Due to its relatively large surface (diameter of ~ 10 cm), thick support ribs (300 μm thick) placed around the thin active areas (50 μm thick) are necessary to provide mechanical stability and integrity of the wafer. The sensor will be produced by SINTEF, Norway [146], and different configurations of the thinned area are being investigated to provide a maximum efficiency of the detector, along with appropriate mechanical stability. A sample of a thinned sensor with thin areas of 5×3 cm^2 before and after cutting out from the wafer is given in fig. 4.13 and fig. 4.14.

The AEḡIS position sensitive detector will implement a daisy-chained readout made of ASICs manufactured by IDE AS (Norway) [101] in CMOS 0.35 μm technology. The chip interface is to be derived from the VATAGP7.1 readout chip [147] which allows for sparse readout i.e. only the strips with a hit are read, thus reducing the dead time of the detector. Moreover, as the antihydrogen arrival time is one of the quantities to be measured, the ASIC will have self-triggering readout capabilities. The required time resolution is obtained by the time-of-flight of the antihydrogen, which, given the expected velocity spread of the beam over few hundred m/s and the distance (1 m), is in the order of ms. Hence, a timing resolution in the order of μs would be satisfactory. Other characteristics specific to the chip design will include:

- Extended dynamic range (up to 1 pC of charge per channel).
- Cryogenic operation, which reliability will be ensured by the possibility to force specific bias voltages to critical elements of the chip (pre-ampiflier, shaper, etc).
- Low power dissipation (in the order of 1mW per readout channel).

The chips will be provided with a bonding pad pattern compatible with the one on the sensor, with a 25 μm channel pitch. All the readout lines will then be directed through a vacuum feedthrough to the DAQ, designed around a Xilinx Spartan FPGA. Connection to the readout servers will be provided by USB 2.0 interface.

4.3.5 AEgIS physics program

As noted in the name of the experiment, the long-term goals of AEgIS include not only a gravity measurement, but also research in interferometry and spectroscopy. The design of the AEgIS apparatus allows modifications to perform higher precision gravity and/or accurate spectroscopic measurements in the second phase, such as Rydberg spectroscopy. When the formation of the antihydrogen beam is well established, a gravity measurement with ultra-cold antihydrogen based on atom interferometry is the main long term scientific goal of AEgIS. The main challenge towards these aims is to trap and cool antihydrogen to mK and sub mK temperatures. Temperatures close to 1 mK are foreseen to be achieved by trapping of antihydrogen atoms in a magnetic trap and cooling them with a quasi-CW Lyman α laser. Such temperatures will be low enough to carry out spectroscopic measurement of the 1S-2S transition with trapped antihydrogen [31].

For the gravitational atom interferometric measurements, where sub mK temperatures are required, the AEgIS collaboration proposes a set-up for trapping antihydrogen that consists of a Penning-Malmberg trap superimposed with a quadrupolar Ioffe-Pritchard [148] (or higher order multipole) trap, so that the antihydrogen is produced directly inside the superimposed traps. R&D activities to reach these ambitious goals are being performed by the AEgIS collaboration.

Chapter 5

Conclusion and further work

This thesis reports the first successful use of silicon sensors as low-energy antiproton annihilation detectors. The aims of the present study can be summarized in two main points: identification of a typical antiproton annihilation signature in a silicon sensor, as a function of the detector's characteristics and study of the impact of detector's parameters on the specific application. These goals was addressed through a systematic study performed on three different silicon detector geometries. As no detector to date was specifically designed for the detection of antiprotons, the three geometries were chosen to address specific question related to the annihilation signature:

- A monolithic sensor was chosen primarily in function of its remarkable dynamic range. Preliminary simulations [31] suggested that annihilations could deposit significant amounts of energies inside the silicon bulk.
- A 3D pixel sensor was employed to assess the contribution to the annihilation signals from the components the monolithic sensor was blind to (i.e. highly energetic pions).
- A strip detector was chosen to verify the response to annihilation events of a 1D detector, as the one to be installed in AEgIS.

These tests allowed to define the specifications for the final AEgIS silicon position detector that is currently being produced. The chosen geometry will allow to reach resolutions of 10 μm (or better, on selected events) by means of adequate reconstruction algorithms.

While the work in this thesis allowed for the definition of the detector parameters in terms of what state-of-the-art technology can provide nowadays, further work has the potential of improving the efficiency and resolution of the AEgIS silicon annihilation detector by means of new reconstruction algorithms. While, ideally, simulation tools would be the benchmark for such algorithms, this thesis work has pointed out some limits of simulation models, where more work is required. These limits arise mainly from the lack of a solid and consistent datasets on antiproton annihilation cross sections in different materials. One can foresee in this sense a sensible progress in the future, when the constantly growing number of experiments in the AD and the construction of new facilities like ELENA will provide more opportunities for ad-hoc studies. AEgIS collaboration is currently commissioning a secondary beam line apparatus dedicated to

a systematic study of low energy antiproton annihilations in different materials, where the author takes part.

Bibliography

[1] Eberhard Klempt, Chris Batty, and Jean-Marc Richard. The antinucleon-nucleon interaction at low energy; annihilation dynamics. *Physics Reports*, 413(4–5):197 – 317, 2005. (document), 2, 2.1, 2.1, 2.2.1, 2.2.1.1, 2.2.1.1

[2] T. von Egidy. Interaction and annihilation of antiprotons and nuclei. *Nature*, 328(6133):773–778, 08 1987. (document), 2.2, 2.4, 2.2.2

[3] M. Kohno and W. Weise. Quark model description of low energy proton—antiproton annihilation into two mesons. *Physics Letters B*, 152(5–6):303 – 307, 1985. (document), 2.3, 2.2.1.1

[4] G. Bendiscioli and D. Kharzeev. Antinucleon-nucleon and antinucleon-nucleus interaction. a review of experimental data. *La Rivista Del Nuovo Cimento Series 3*, 17(6):1–142, 1994. (document), 2, 2.2.1, 2.2.1, 2.5, 2.2.2

[5] J. Beringer et al. Review of particle physics. *Phys. Rev. D*, 86:010001, Jul 2012. (document), 3, 3.1, 3.1

[6] S. P. Møller, E. Uggerhøj, H. Bluhme, H. Knudsen, U. Mikkelsen, K. Paludan, and E. Morenzoni. Direct measurements of the stopping power for antiprotons of light and heavy targets. *Phys. Rev. A*, 56:2930–2939, Oct 1997. (document), 3.2, 3.1

[7] R. Medenwaldt, S.P. Møller, E. Uggerhøj, T. Worm, P. Hvelplund, H. Knudsen, K. Elsener, and E. Morenzoni. Measurement of the stopping power of silicon for antiprotons between 0.2 and 3 MeV. *Nuclear Instruments and Methods in Physics Research Section B: Beam Interactions with Materials and Atoms*, 58(1):1 – 5, 1991. (document), 3.2, 3.1

[8] ICRU. Icru report. Technical Report 49, ISBN 0-913394-47-5, 1993. unpublished. (document), 3.2

[9] Allan H. Sørensen. Barkas effect at low velocities. *Nuclear Instruments and Methods in Physics Research Section B: Beam Interactions with Materials and Atoms*, 48(1–4):10 – 13, 1990. (document), 3.2, 3.1

[10] Wikipedia. LaTeX — Wikipedia, the free encyclopedia, 2014. [Online; accessed 7-May-2014]. (document), 3.3

[11] http://hep.fi.infn.it/cms/sensors/silicon_detector.gif. (document), 3.5

[12] http://cms.web.cern.ch/news/silicon-pixels. (document), 3.7

[13] Leonardo Rossi. Pixel detectors hybridisation. *Nuclear Instruments and Methods in Physics Research Section A: Accelerators, Spectrometers, Detectors and Associated Equipment*, 501(1):239 – 244, 2003. Proceedings of the 10th International Workshop on Vertex Detectors. (document), 3.8

[14] 3D active edge silicon sensors test results, 2006. [Online; accessed 15-May-2014]. (document), 3.9

[15] Christopher J. Kenney, Sherwood I. Parker, Vincent Z. Peterson, Walter J. Snoeys, James D. Plummer, and Chye Huat Aw. A prototype monolithic pixel detector. *Nuclear Instruments and Methods in Physics Research Section A: Accelerators, Spectrometers, Detectors and Associated Equipment*, 342(1):59 – 77, 1994. (document), 3.10

[16] G Claus, C Colledani, G Deptuch, W Dulinski, Y Gornushkin, Y Hu, D Husson, G Orazi, R Turchetta, J.L Riester, and M Winter. Monolithic active pixel sensors for a linear collider. *Nuclear Instruments and Methods in Physics Research Section A: Accelerators, Spectrometers, Detectors and Associated Equipment*, 473(1–2):83 – 85, 2001. Proceedings of the 9th International Workshop on Vertex Detectors. (document), 3.11

[17] M. Amoretti et al. The ATHENA antihydrogen apparatus. *Nuclear Instruments and Methods in Physics Research Section A: Accelerators, Spectrometers, Detectors and Associated Equipment*, 518(3):679 – 711, 2004. (document), 3.4.1, 3.12, 3.13, 3.16, 4.3.2.1

[18] G. B. Andresen et al. The ALPHA – detector: Module production and assembly. *Journal of Instrumentation*, 7(01):C01051, 2012. (document), 3.4.1, 3.14

[19] G.B. Andresen et al. Antihydrogen annihilation reconstruction with the ALPHA silicon detector. *Nuclear Instruments and Methods in Physics Research Section A: Accelerators, Spectrometers, Detectors and Associated Equipment*, 684(0):73 – 81, 2012. (document), 3.4.1, 3.4.1, 3.15

[20] Stefan Sellner, Rebecca Boll, Massimo Caccia, Loretta Negrini, Tina Straße, Sara Tegami, and MichaelH. Holzscheiter. The antiproton cell experiment—do antiprotons offer advantages over other particle beam modalities? *Hyperfine Interactions*, 213(1-3):159–174, 2012. (document), 3.17, 3.4.2

[21] Walter Oelert, Tommy Eriksson, Pavel Belochitskii, and Gerard Tranquille. AD performance and its extension towards ELENA. *Hyperfine Interactions*, 213(1-3):227–236, 2012. (document), 4.1, 4.2

[22] M. Hori and J. Walz. Physics at CERN's Antiproton Decelerator. *Progress in Particle and Nuclear Physics*, 72(0):206 – 253, 2013. (document), 4.2, 4.2

[23] David W. Gidley, Hua-Gen Peng, and Richard S. Vallery. Positron annihilation as a method to characterize porous materials. *Annual Review of Materials Research*, 36(1):49–79, 2006. (document), 4.3.1, 4.6

[24] R. Hydomako. *Detection of Trapped Antihydrogen*. Springer Theses. Springer, 2012. (document), 4.3.2.1, 4.7

[25] J. Storey et al. Particle tracking at 4K: The fast annihilation cryogenic tracking (FACT) detector for the AEgIS antimatter gravity experiment. *Nuclear Instruments and Methods in Physics Research Section A: Accelerators, Spectrometers, Detectors and Associated Equipment*, 732(0):437 – 441, 2013. Vienna Conference on Instrumentation 2013. (document), 4.3.4, 4.10, 6

[26] John Ellis. Particle physics: Antimatter matters. *Nature*, 424(6949):631–634, 08 2003. 1

[27] A. D. Sakharov. Violation of CP invariance, C asymmetry and baryon asymmetry of the Universe. *Journal of Experimental and Theoretical Physics*, 5:24, 1967. 1

[28] J. H. Christenson, J. W. Cronin, V. L. Fitch, and R. Turlay. Evidence for the 2π decay of the $K_2{}^o$ meson. *Phys. Rev. Lett*, 13:138, 1964. 1

[29] Tommy Ohlsson, He Zhang, and Shun Zhou. Radiative corrections to the leptonic Dirac *CP*-violating phase. *Phys. Rev. D*, 87:013012, Jan 2013. 1

[30] M. Fukugita and T. Yanagida. Barygenesis without grand unification. *Physics Letters B*, 174(1):45 – 47, 1986. 1

[31] The AEgIS collaboration. Proposal for the aegis experiment at the cern antiproton decelerator, 2007. 1, 3, 4, 4.1, 4.3.1, 4.3.2.1, 4.3.3.1, 4.3.3.2, 4.25, 4.3.4.1, 4.3.4.1, 4.3.5, 5

[32] C. Amsler and F. Myhrer. Low energy antiproton physics. *Annual Review of Nuclear and Particle Science*, 41(1):219–267, 1991. 2, 2.2.1

[33] W. Weise. Anti-nucleon nucleon annihilation. *Nucl.Phys.*, A558:219C–234C, 1993. 2

[34] P. A. M. Dirac. The quantum theory of the electron. *Proceedings of the Royal Society of London. Series A*, 117(778):610–624, 1928. 2.1

[35] Carl D. Anderson. The positive electron. *Phys. Rev.*, 43:491–494, Mar 1933. 2.1

[36] Owen Chamberlain, Emilio Segrè, Clyde Wiegand, and Thomas Ypsilantis. Observation of antiprotons. *Phys. Rev.*, 100:947–950, Nov 1955. 2.1

[37] Bruce Cork, Glen R. Lambertson, Oreste Piccioni, and William A. Wenzel. Antineutrons produced from antiprotons in charge-exchange collisions. *Phys. Rev.*, 104:1193–1197, Nov 1956. 2.1

[38] R. Klapisch. The LEAR project and physics with low energy antiprotons at CERN (A Summary). *Physica Scripta*, 1983(T5):140, 1983. 2.1

[39] E. Aker et al. The Crystal Barrel spectrometer at LEAR. *Nuclear Instruments and Methods in Physics Research Section A: Accelerators, Spectrometers, Detectors and Associated Equipment*, 321(1–2):69 – 108, 1992. 2.1

[40] A. Adamo et al. First physics results from OBELIX. *Sov.J.Nucl.Phys.*, 55:1732–1742, 1992. 2.1

[41] G. Baur et al. Production of antihydrogen. *Physics Letters B*, 368(3):251 – 258, 1996. 2.1

[42] S. Maury. The Antiproton Decelerator: AD. *Hyperfine Interactions*, 109(1-4):43–52, 1997. 2.1

[43] M. Amoretti et al. Production and detection of cold antihydrogen atoms. *Nature*, 419(6906):456–459, 10 2002. 2.1

[44] G. Gabrielse et al. Background-free observation of cold antihydrogen with field-ionization analysis of its states. *Phys. Rev. Lett.*, 89:213401, Oct 2002. 2.1

[45] G. B. Andresen et al. Trapped antihydrogen. *Nature*, 468(7324):673–676, 12 2010. 2.1

[46] The ALPHA Collaboration. Confinement of antihydrogen for 1,000 seconds. *Nat Phys*, 7(7):558–564, 07 2011. 2.1

[47] Masaki Hori et al. Two-photon laser spectroscopy of antiprotonic helium and the antiproton-to-electron mass ratio. *Nature*, 475(7357):484–488, 07 2011. 2.1

[48] R. Marshall. Electron-positron annihilation at high energies. *Reports on Progress in Physics*, 52(11):1329, 1989. 2.2.1

[49] A.J. Apostolakis, G.A. Briggs, N.A. Khan, and J.V. Major. The annihilation of antiprotons on protons and neutrons. *Il Nuovo Cimento*, 37(4):1364–1375, 1965. 2.2.1

[50] T. Armstrong et al. Measurement of antineutron-proton total and annihilation cross sections from 100 to 500 mev/c. *Phys. Rev. D*, 36:659–673, Aug 1987. 2.2.1

[51] B. Moussallam. $\bar{p}p \to \pi\pi$ in a baryon-exchange-potential model. *Nuclear Physics A*, 429(3):429 – 444, 1984. 2.2.1.1

[52] Johann Haidenbauer, Thomas Hippchen, and Karl Holinde. The bonn $\bar{n}N$ potential and the range of $\bar{n}N$ annihilation. *Nuclear Physics A*, 508(0):329 – 334, 1990. 2.2.1.1

[53] V. Mull, J. Haidenbauer, T. Hippchen, and K. Holinde. Meson-baryon dynamics in the nucleon-antinucleon system. II. Annihilation into two mesons. *Phys. Rev. C*, 44:1337–1353, Oct 1991. 2.2.1.1

[54] T. Hippchen, J. Haidenbauer, K. Holinde, and V. Mull. Meson-baryon dynamics in the nucleon-antinucleon system. I. the nucleon-antinucleon interaction. *Phys. Rev. C*, 44:1323–1336, Oct 1991. 2.2.1.1

[55] V. Mull and K. Holinde. Combined description of anti-N N scattering and annihilation with a hadronic model. *Phys.Rev.*, C51:2360–2371, 1995. 2.2.1.1

[56] H.R. Rubinstein and H. Stern. Nucleon-antinucleon annihilation in the quark model. *Physics Letters*, 21(4):447 – 449, 1966. 2.2.1.1

[57] J. Harte, R.H. Socolow, and J. Vandermeulen. A study of the quark rearrangement model of nucleon-antinucleon annihilation. *Il Nuovo Cimento A*, 49(4):555–576, 1967. 2.2.1.1

[58] M. Maruyama and T. Ueda. $\bar{n}$N annihilation at low energies in a quark rearrangement model and decay widths of $\bar{n}$N bound states. *Nuclear Physics A*, 364(2–3):297 – 321, 1981. 2.2.1.1

[59] M. Maruyama and T. Ueda. A quark rearrangement model with spatial overlap function for low energy $\bar{n}$N annihilation. *Physics Letters B*, 124(1–2):121 – 126, 1983. 2.2.1.1

[60] Sadataka Furui, Amand Faessler, and S.B. Khadkikar. $p\bar{p}$ annihilation at rest into mesons in the quark rearrangement model and the quark annihilation model. *Nuclear Physics A*, 424(3):495 – 524, 1984. 2.2.1.1

[61] J. Vandermeulen. N$\bar{n}$ annihilation creates two mesons. *Zeitschrift für Physik C Particles and Fields*, 37(4):563–567, 1988. 2.2.1.1

[62] A.S. Iljinov, V.I. Nazaruk, and S.E. Chigrinov. Nuclear absorption of stopped antiprotons: Multipion-nucleus interactions. *Nuclear Physics A*, 382(3):378 – 400, 1982. 2.2.2

[63] J. Rafelski. $\bar{p}$ annihilation on heavy nuclei. *Physics Letters B*, 91(2):281 – 284, 1980. 2.2.2

[64] Hugo W. Bertini. Low-energy intranuclear cascade calculation. *Phys. Rev.*, 131:1801–1821, Aug 1963. 2.2.2

[65] J. Cugnon and J. Vandermeulen. Antiproton-nucleus interaction. *Ann. Phys. Fr.*, 14(1):49–87, 1989. 2.2.2

[66] J.P. Bocquet et al. Observation of the delayed fission induced by antiproton annihilation in ^{238}U. *Physics Letters B*, 182(2):146 – 150, 1986. 2.2.2

[67] A.S. Botvina, A.S. Iljinov, I.N. Mishustin, J.P. Bondorf, R. Donangelo, and K. Sneppen. Statistical simulation of the break-up of highly excited nuclei. *Nuclear Physics A*, 475(4):663 – 686, 1987. 2.2.2

[68] Carlo Guaraldo. Low energy antiproton-nucleus annihilation. *Nuclear Physics B - Proceedings Supplements*, 8(0):243 – 254, 1989. 2.2.2

[69] I. Dostrovsky, Z. Fraenkel, and G. Friedlander. Monte Carlo calculations of nuclear evaporation processes. III. Applications to low-energy reactions. *Phys. Rev.*, 116:683–702, Nov 1959. 2.2.2

[70] J.P. Bondorf, R. Donangelo, I.N. Mishustin, C.J. Pethick, H. Schulz, and K. Sneppen. Statistical multifragmentation of nuclei: (I). Formulation of the model. *Nuclear Physics A*, 443(2):321 – 347, 1985. 2.2.2

[71] J. Bondorf, R. Donangelo, I.N. Mishustin, and H. Schulz. Statistical multifragmentation of nuclei: (II). Application of the model to finite nuclei disassembly. *Nuclear Physics A*, 444(3):460 – 476, 1985. 2.2.2

[72] H.W. Barz, J.P. Bondorf, R. Donangelo, I.N. Mishustin, and H. Schulz. Statistical multifragmentation of nuclei: (III). Decay of the fragments. *Nuclear Physics A*, 448(4):753 – 763, 1986. 2.2.2

[73] E.F. Moser, H. Daniel, T. von Egidy, F.J. Hartmann, W. Kanert, G. Schmidt, Ye.S. Golubeva, A.S. Iljinov, M. Nicholas, and J.J. Reidy. Residual nuclei after antiproton annihilation in Mo and Ho. *Zeitschrift für Physik A Atomic Nuclei*, 333(1):89–105, 1989. 2.2.2

[74] B.M. Pontecorvo. One-meson and zero-meson annihilation of antinucleons. *Zh.Eksp.Teor.Fiz.*, 30:947–948, 1956. 2.2.2

[75] J. Riedlberger et al. Antiproton annihilation at rest in nitrogen and deuterium gas. *Phys. Rev. C*, 40:2717–2731, Dec 1989. 2.2.2

[76] C. Amsler et al. First observations of Pontecorvo reactions with a recoiling neutron. *Zeitschrift für Physik A Hadrons and Nuclei*, 351(3):325–331, 1995. 2.2.2

[77] L.A. Kondratyuk and M.G. Sapozhnikov. Pontecorvo reactions of two-body antiproton annihilation in deuterium. *Physics Letters B*, 220(3):333 – 336, 1989. 2.2.2

[78] W. Markiel, H. Daniel, T. Von Egidy, F.J. Hartmann, P. Hofmann, W. Kanert, H.S. Plendl, K. Ziock, R. Marshall, H. Machner, G. Riepe, and J.J. Reidy. Emission of helium ions after antiproton annihilation in nuclei. *Nuclear Physics A*, 485(3–4):445 – 460, 1988. 2.2.2, 2.2.2

[79] P. Hofmann, F.J. Hartmann, H. Daniel, T. Von Egidy, W. Kanert, W. Markiel, H.S. Plendl, H. Machner, G. Riepe, D. Protić, K. Ziock, R. Marshall, and J.J. Reidy. Charged-particle spectra from antiproton annihilation at rest in A = 12–238 nuclei. *Nuclear Physics A*, 512(4):669 – 683, 1990. 2.2.2

[80] S. Aghion et al. Detection of low energy antiproton annihilations in a segmented silicon detector. *Journal of Instrumentation*, 9(06):P06020, 2014. 2.2.2, 3, 3.1

[81] N. Pacifico et al. Investigation of silicon sensors for their use as antiproton annihilation detectors. *Nuclear Instruments and Methods in Physics Research Section A: Accelerators, Spectrometers, Detectors and Associated Equipment*, (0):–, 2014. 3

[82] W.R. Leo. *Techniques for Nuclear and Particle Physics Experiments: A How-To Approach*. U.S. Government Printing Office, 1994. 3, 3.1

[83] F. Hartmann. *Evolution of Silicon Sensor Technology in Particle Physics*. Springer Tracts in Modern Physics. Springer, 2009. 3, 3.3.2.2

[84] P. Rossi, L.and Fischer, T. Rohe, and N. Wermes. *Pixel Detectors: From Fundamentals to Applications*. Springer, 2006. 3, 3.3.2

[85] Walter H. Barkas, Wallace Birnbaum, and Frances M. Smith. Mass-ratio method applied to the measurement of L-meson masses and the energy balance in pion decay. *Phys. Rev.*, 101:778–795, Jan 1956. 3.1

[86] M.M.R. Williams. The stopping and ranges of ions in matter: Volumes 2, 3 and 4. *Annals of Nuclear Energy*, 5(11–12):649, 1978. 3.1

[87] J. Lindhard, M. Scharff, and H. E. Schiøtt. Range concepts and heavy ion ranges. *Kgl. Danske Videnskab. Selskab, Mat.-Fys. Medd.*, 33(14), 1963. 3.1

[88] H. Spieler. *Semiconductor Detector Systems*. Series on Semiconductor Science and Technology. OUP Oxford, 2005. 3.2.1, 3.2.3

[89] S Ramo. Currents induced by electron motion. *Proceedings of the IRE,*, 27(9):584 – 585, 1939. 3.2.3

[90] S.I. Parker, C.J. Kenney, and J. Segal. 3D — a proposed new architecture for solid-state radiation detectors. *Nuclear Instruments and Methods in Physics Research Section A: Accelerators, Spectrometers, Detectors and Associated Equipment*, 395(3):328 – 343, 1997. Proceedings of the Third International Workshop on Semiconductor Pixel Detectors for Particles and X-rays. 3.3.2.1

[91] Cinzia Da Via et al. 3D silicon sensors: Design, large area production and quality assurance for the ATLAS IBL pixel detector upgrade. *Nuclear Instruments and Methods in Physics Research Section A: Accelerators, Spectrometers, Detectors and Associated Equipment*, 694(0):321 – 330, 2012. 3.3.2.1

[92] C.J. Kenney, S. Parker, and E. Walckiers. Results from 3-D silicon sensors with wall electrodes: near-cell-edge sensitivity measurements as a preview of active-edge sensors. *Nuclear Science, IEEE Transactions on*, 48(6):2405–2410, Dec 2001. 3.3.2.1

[93] G.-F.D. Betta, A. Bagolini, M. Boscardin, G. Giacomini, M. Povoli, E. Vianello, and N. Zorzi. Development of active and slim edge terminations for 3D and planar detectors. In *Nuclear Science Symposium and Medical Imaging Conference (NSS/MIC), 2011 IEEE*, pages 1334–1340, Oct 2011. 3.3.2.1

[94] D. Pennicard, C. Fleta, R. Bates, V. O'Shea, C. Parkes, G. Pellegrini, M. Lozano, J. Marchal, and N. Tartoni. Charge sharing in double-sided 3D Medipix2 detectors. *Nuclear Instruments and Methods in Physics Research Section A: Accelerators, Spectrometers, Detectors and Associated Equipment*, 604(1–2):412 – 415, 2009. {PSD8} Proceedings of the 8th International Conference on Position Sensitive Detectors. 3.3.2.1

[95] C. Kenney, S. Parker, J. Segal, and C. Storment. Silicon detectors with 3-D electrode arrays: fabrication and initial test results. *Nuclear Science, IEEE Transactions on*, 46(4):1224–1236, Aug 1999. 3.3.2.1

[96] W. Snoeys, J. Plummer, S. Parker, and C. Kenney. A new integrated pixel detector for high energy physics. *Nuclear Science, IEEE Transactions on*, 39(5):1263–1269, Oct 1992. 3.3.2.2

[97] L. Rossi, P. Fischer, T. Rohe, and N. Wermes. *Pixel Detectors From Fundamentals to Applications*. Springer-Verlag, New York, 2006. 3.3.2.2, 3.3.2.2

[98] R. Boll, M. Caccia, C.P. Welsch, and M.H. Holzscheiter. Using monolithic active pixel sensors for fast monitoring of therapeutic hadron beams. *Radiation Measurements*, 46(12):1971 – 1973, 2011. Proceedings of the 16th Solid State Dosimetry Conference , September 19-24 , Sydney , Australia. 3.3.2.2

[99] A. Holmes-Siedle and L. Adams. *Handbook of Radiation Effects*. Oxford science publications. OUP Oxford, 2002. 3.3.2.2

[100] C. Regenfus. A cryogenic silicon micro-strip and pure-CsI detector for detection of antihydrogen annihilations. *Nuclear Instruments and Methods in Physics Research Section A: Accelerators, Spectrometers, Detectors and Associated Equipment*, 501(1):65 – 71, 2003. Proceedings of the 10th International Workshop on Vertex Detectors. 3.4.1

[101] Integrated Detector Electronics AS (NORWAY). Ideas, MARTIN LINGES VEl 25, SNAR0YA, POB I, N-1330, FORNEBU, NORWAY. 3.4.1, 4.3.4.1

[102] P. Riedler, J. Rochet, A. Rudge, M. Doser, and R. Landua. Performance of ultra-thin silicon detectors in a 5.3 MeV. *Nuclear Instruments and Methods in Physics Research Section A: Accelerators, Spectrometers, Detectors and Associated Equipment*, 478(1–2):316 – 320, 2002. Proceedings of the ninth Int.Conf. on Instrumentation. 3.4.2, 4.3.2

[103] J.W. Sunier, K.D. Bol, M.R. Clover, R.M. DeVries, N.J. DiGiacomo, J.S. Kapustinsky, P.L. McGaughey, and W.E. Sondheim. Calliope — a large acceptance multiparticle magnetic spectrometer for intermediate energy physics. *Nuclear Instruments and Methods in Physics Research Section A: Accelerators, Spectrometers, Detectors and Associated Equipment*, 241(1):139 – 152, 1985. 3.4.3

[104] P.L. McGaughey, N.J. DiGiacomo, W.E. Sondheim, J.W. Sunier, and Y. Yariv. Low energy antiproton-nucleus annihilation radius selection using an active silicon detector/target. *Nuclear Instruments and Methods in Physics Research Section A: Accelerators, Spectrometers, Detectors and Associated Equipment*, 249(2–3):361 – 365, 1986. 3.4.3

[105] D. Krasnický et al. AEgIS experiment commissioning at CERN. *AIP Conference Proceedings*, 1521(1):144–153, 2013. 4, 4.3.2.1, 4.3.2.1, 6

[106] M. Villata. CPT symmetry and antimatter gravity in general relativity. *EPL (Europhysics Letters)*, 94(2):20001, 2011. 4.1, 4.1

[107] C. J. Kevane. On antimatter and cosmology. *Science*, 133(3452):580–581, 1961. 4.1

[108] T. Goldman, Richard J. Hughes, and Michael Martin Nieto. Gravitational acceleration of antiprotons and of positrons. *Phys. Rev. D*, 36:1254–1256, Aug 1987. 4.1

[109] G.W. Ford and D.J. Hegyi. A new limit on scalar and vector contributions to gravity. *Physics Letters B*, 219(2–3):247 – 250, 1989. 4.1

[110] J. Scherk. Antigravity: A crazy idea? *Physics Letters B*, 88(3–4):265 – 267, 1979. 4.1

[111] T. Goldman, Richard J. Hughes, and Michael Martin Nieto. Experimental evidence for quantum gravity? *Physics Letters B*, 171(2–3):217 – 222, 1986. 4.1

[112] M. Villata. "Dark energy" in the Local Void. *Astrophysics and Space Science*, 339(1):7–12, 2012. 4.1

[113] Benoit-Lévy, A. and Chardin, G. Introducing the Dirac-Milne universe. *A&A*, 537:A78, 2012. 4.1

[114] M.H. Holzscheiter et al. Trapping of antiprotons in a large penning trap — progress towards a measurement of the gravitational acceleration of the antiproton. *Nuclear Physics A*, 558(0):709 – 718, 1993. 4.1

[115] F. C. Witteborn and W. M. Fairbank. Experimental comparison of the gravitational force on freely falling electrons and metallic electrons. *Phys. Rev. Lett.*, 19:1049–1052, Oct 1967. 4.1

[116] Fred C. Witteborn and William M. Fairbank. Experiments to determine the force of gravity on single electrons and positrons. *Nature*, 220(5166):436–440, 11 1968. 4.1

[117] The ALPHA Collaboration and A. E. Charman. Description and first application of a new technique to measure the gravitational mass of antihydrogen. *Nature Communications*, 4:1785, 04 2013. 4.1

[118] M-E Angoletta et al. ELENA – An Updated Cost and Feasibility Study. Technical Report CERN-BE-2010-029, CERN, Geneva, Nov 2010. 4.2

[119] Markus K. Oberthaler, Stefan Bernet, Ernst M. Rasel, Jörg Schmiedmayer, and Anton Zeilinger. Inertial sensing with classical atomic beams. *Phys. Rev. A*, 54:3165–3176, Oct 1996. 4.3, 4.3.4.1

[120] R. G. Greaves, M. D. Tinkle, and C. M. Surko. Creation and uses of positron plasmas*. *Physics of Plasmas (1994-present)*, 1(5):1439–1446, 1994. 4.3.1

[121] X.-P. Huang, F. Anderegg, E. M. Hollmann, C. F. Driscoll, and T. M. O'Neil. Steady-state confinement of non-neutral plasmas by rotating electric fields. *Phys. Rev. Lett.*, 78:875–878, Feb 1997. 4.3.1, 4.3.2.2

[122] K. F. Canter, A. P. Mills, and S. Berko. Efficient positronium formation by slow positrons incident on solid targets. *Phys. Rev. Lett.*, 33:7–10, Jul 1974. 4.3.1

[123] S. Mariazzi, P. Bettotti, S. Larcheri, L. Toniutti, and R. S. Brusa. High positronium yield and emission into the vacuum from oxidized tunable nanochannels in silicon. *Phys. Rev. B*, 81:235418, Jun 2010. 4.3.1

[124] Sebastiano Mariazzi, Paolo Bettotti, and Roberto S. Brusa. Positronium cooling and emission in vacuum from nanochannels at cryogenic temperature. *Phys. Rev. Lett.*, 104:243401, Jun 2010. 4.3.1

[125] S. Cialdi, I. Boscolo, F. Castelli, F. Villa, G. Ferrari, and M.G. Giammarchi. Efficient two-step positronium laser excitation to rydberg levels. *Nuclear Instruments and Methods in Physics Research Section B: Beam Interactions with Materials and Atoms*, 269(13):1527 – 1533, 2011. 4.3.1

[126] E. A. Hessels, D. M. Homan, and M. J. Cavagnero. Two-stage Rydberg charge exchange: An efficient method for production of antihydrogen. *Phys. Rev. A*, 57:1668–1671, Mar 1998. 4.3.1, 4.3.3.2

[127] F.G. Major, V.N. Gheorghe, and G. Werth. *Charged Particle Traps: Physics and Techniques of Charged Particle Field Confinement*. Springer Series on Atomic, Optical, and Plasma Physics. Springer, 2006. 4.3.2.1

[128] R.C. Davidson. *Physics of Nonneutral Plasmas*. Imperial College Press, 2001. 4.3.2.1

[129] G. Gabrielse, X. Fei, L. A. Orozco, R. L. Tjoelker, J. Haas, H. Kalinowsky, T. A. Trainor, and W. Kells. Cooling and slowing of trapped antiprotons below 100 mev. *Phys. Rev. Lett.*, 63:1360–1363, Sep 1989. 4.3.2.1

[130] H. Higaki, N. Kuroda, K. Yoshiki Franzen, Z. Wang, M. Hori, A. Mohri, K. Komaki, and Y. Yamazaki. Radial compression of protons and H_3^+ ions in a multiring trap for the production of ultra low energy antiproton beams. *Phys. Rev. E*, 70:026501, Aug 2004. 4.3.2.1

[131] A. Kellerbauer et al. Sideband cooling of ions in a non-neutral buffer gas. *Phys. Rev. A*, 73:062508, Jun 2006. 4.3.2.1

[132] J. R. Danielson, T. R. Weber, and C. M. Surko. Plasma manipulation techniques for positron storage in a multicell trap. *Physics of Plasmas (1994-present)*, 13(12), 2006. 4.3.2.2

[133] J. Fajans, E. Gilson, and L. Friedland. Autoresonant (nonstationary) excitation of a collective nonlinear mode. *Physics of Plasmas (1994-present)*, 6(12):4497–4503, 1999. 4.3.2.2

[134] C. Canali, C. Carraro, D. Krasnicky, V. Lagomarsino, L. Noto, G. Testera, and S. Zavatarelli. Off-axial plasma displacement suitable for antihydrogen production in aegis experiment. *The European Physical Journal D*, 65(3):499–504, 2011. 4.3.2.2

[135] Lowell S. Brown and Gerald Gabrielse. Geonium theory: Physics of a single electron or ion in a penning trap. *Rev. Mod. Phys.*, 58:233–311, Jan 1986. 4.3.3.1

[136] Alban Kellerbauer and Jochen Walz. A novel cooling scheme for antiprotons. *New Journal of Physics*, 8(3):45, 2006. 4.3.3.1

[137] T.W. Hänsch and A.L. Schawlow. Cooling of gases by laser radiation. *Optics Communications*, 13(1):68 – 69, 1975. 4.3.3.1

[138] A Crubellier. Theory of laser evaporative cooling of trapped negative ions. I. Harmonically bound ions and RF traps. *Journal of Physics B: Atomic, Molecular and Optical Physics*, 23(20):3585, 1990. 4.3.3.1

[139] B. Deutch, A. Jensen, A. Miranda, and G. Oades. Antiproton capture in neutral beams. *Proceedings of The First Workshop on Antimatter Physics at Low Energy*, page 371, 1986. 4.3.3.2

[140] C. H. Storry et al. First laser-controlled antihydrogen production. *Phys. Rev. Lett.*, 93:263401, Dec 2004. 4.3.3.2

[141] G. Gabrielse et al. Driven production of cold antihydrogen and the first measured distribution of antihydrogen states. *Phys. Rev. Lett.*, 89:233401, Nov 2002. 4.3.3.2

[142] T. F. Gallagher. Rydberg atoms. *Reports on Progress in Physics*, 51(2):143, 1988. 4.3.3.2

[143] G. Testera et al. Formation of a cold antihydrogen beam in aegis for gravity measurements. *AIP Conference Proceedings*, 1037(1):5–15, 2008. 4.3.3.2

[144] E. Vliegen, S. D. Hogan, H. Schmutz, and F. Merkt. Stark deceleration and trapping of hydrogen rydberg atoms. *Phys. Rev. A*, 76:023405, Aug 2007. 4.3.3.2

[145] S. Aghion et al. Prospects for measuring the gravitational free-fall of antihydrogen with emulsion detectors. *Journal of Instrumentation*, 8(08):P08013, 2013. 4.3.4.1, 6

[146] SINTEF. Foundation of scientific and industrial research at the norwegian institute of technology, electronics and cybernetics, microsystems, Oslo and Trondheim, Norway. 4.3.4.1

[147] V. Stankova et al. DAQ system for the readout of silicon pixel detectors based on VataGP7 front-end ASIC. In *Nuclear Science Symposium and Medical Imaging Conference (NSS/MIC), 2012 IEEE*, pages 1084–1086, Oct 2012. 4.3.4.1

[148] David E. Pritchard. Cooling neutral atoms in a magnetic trap for precision spectroscopy. *Phys. Rev. Lett.*, 51:1336–1339, Oct 1983. 4.3.5

[149] S. Aghion et al. A moirédeflectometer for antimatter. *Nat Commun*, 5, 07 2014. 6

[150] P. Scampoli et al. Development of nuclear emulsions operating in vacuum for the AEgIS experiment. *Journal of Instrumentation*, 9(01):C01061, 2014. 6

[151] C. Nellist (on behalf of ATLAS collaboration), A. Gligorova, T. Huse, N. Pacifico, and H. Sandaker. Beam test results of 3D silicon pixel sensors for future upgrades. *Nuclear Instruments and Methods in Physics Research Section A: Accelerators, Spectrometers, Detectors and Associated Equipment*, 732(0):141 – 145, 2013. Vienna Conference on Instrumentation 2013. 6

[152] M. Kimura et al. Development of nuclear emulsions with spatial resolution for the AEgIS experiment. *Nuclear Instruments and Methods in Physics Research Section A: Accelerators, Spectrometers, Detectors and Associated Equipment*, 732(0):325 – 329, 2013. Vienna Conference on Instrumentation 2013. 6

[153] M. Doser et al. Exploring the WEP with a pulsed cold beam of antihydrogen. *Classical and Quantum Gravity*, 29(18):184009, 2012. 6

[154] A. Kellerbauer et al. The AEGIS experiment at CERN. *Hyperfine Interactions*, 209(1-3):43–49, 2012. 6

Chapter 6

Introduction to the papers

The peer reviewed papers in the following pages present the results obtained from the first applications of segmented silicon detectors for direct detection of antiproton annihilations. The data presented in the paper were collected in AEḡIS antiproton runs in the months of May 2012 and December 2012. In particular, the latter one was the last beam period available before a long shut down of the accelerator complex at CERN, that lasted until August 2014. Silicon detectors with different geometry and based on different technologies were used to detect low energy antiprotons, in particular:

- Monolithic Active Pixel Sensor (MAPS)
- Silicon micro-strip detector
- 3D pixel detector

The three papers include description of the detectors, the installation and data taking procedure as well as analysis of beam test data on the three kinds of silicon detectors. Pixel detectors (MAPS and 3D) are in particular used to understand the annihilation topology (number and typology of annihilation prongs, energy distribution of the annihilation events). The papers also presented comparison of the data obtained with pixel detectors to Monte Carlo simulations, in an effort to test the reliability of the annihilation models available.

In addition to being among the primary contributors of the above stated publications, the author of this thesis actively contributed to the overall experiment operation with data taking sessions and shifts, as well as by being responsible for the silicon beam condition monitor installed in the experiment. The work done as part of the AEḡIS collaboration resulted in the publication of 10 further collaborative works on peer reviewed journals [25, 105, 145, 149–154].